Spring 2015

Timing and Source of Alkali Enrichment at Mt. Etna, Sicily: Constraints from Clinopyroxene Geobarometry and In Situ SR Isotope Data

Kaitlyn Nelson
Central Washington University, nelsonk@geology.cwu.edu

TIMING AND SOURCE OF ALKALI-ENRICHMENT AT MT. ETNA, SICILY: CONSTRAINTS FROM CLINOPYROXENE GEOBAROMETRY AND *IN SITU* SR ISOTOPE DATA

A Thesis

Presented to

The Graduate Faculty

Central Washington University

In Partial Fulfillment

of the Requirements for the Degree

Master of Science

Geology

---

by

Kaitlyn Mary Nelson

May 2015

CENTRAL WASHINGTON UNIVERSITY

Graduate Studies

We hereby approve the thesis of

Kaitlyn Mary Nelson

Candidate for the degree of Master of Science

APPROVED FOR THE GRADUATE FACULTY

_____	_____
	Dr. Wendy Bohrson, Committee Chair
_____	_____
	Dr. Chris Mattinson
_____	_____
	Dr. Jeff Lee
_____	_____
	Dr. Optional Fourth Committee Member
_____	_____
	Dean of Graduate Studies

ABSTRACT

TIMING AND SOURCE OF ALKALI-ENRICHMENT AT MT. ETNA, SICILY:
CONSTRAINS FROM CLINOPYROXENE GEOBAROMETRY
AND *IN SITU* SR ISOTOPE DATA

by

Kaitlyn Mary Nelson

May 2015

Since 1971, Mt. Etna, Europe's largest and most active volcano, has exhibited increased eruption frequency and explosivity. Associated with this increased activity, researchers have documented higher abundances of alkali elements (K, Rb, Cs) as well as elevated $^{87}Sr/^{86}Sr$ in Etnean lavas. The source of this alkali-enrichment has been hotly debated, with end-member hypotheses involving mantle vs. crustal contributions. To further characterize the evolution of the subvolcanic magma storage and transport system, as well as the timing and source of alkali-enrichment, clinopyroxene from ten samples erupted between 1329 and 2004 was targeted for *in situ* textural, major element and Sr isotope analysis. Clinopyroxene disequilibrium textures paired with increased Mg# values imply recharge/mixing at work within a dynamic magmatic system. Calculated pressures also reveal a dominant crystallization zone between ~8.7 and 16.5 km within the volcano's carbonate substratum. A select population of clinopyroxene exhibits increasing weight percent CaO and Mg# with decreasing pressure, providing new evidence for late-stage carbonate assimilation enhanced by magmatic recharge. Alkali-enrichment is thus likely a consequence of both magma recharge and crustal assimilation.

ACKNOWLEDGMENTS

I first would like to sincerely thank my advisor and mentor, Dr. Wendy Bohrson. Her incredible instruction, guidance, patience, compassion, friendship and wisdom throughout this process have instilled in me a deep appreciation for the scientific process and the study of igneous petrology and volcanology. She has provided me an unparalleled experience, which has marked me as a scientist, as well as an individual, for life. I wish to thank her for her great generosity of time and devotion throughout these years, as well as the integrity and kindness she exemplifies as a person.

I would also like to thank the many faculty and staff at Central Washington University. To study igneous processes has been a most challenging and fulfilling endeavor, and I am truly thankful for such an opportunity. To experience geology in the beauty of the Pacific Northwest has contributed much to my understanding and appreciation of this field of science, and I am grateful to all who have been a part of this process. Also, a special thank you to Dr. Frank Ramos of New Mexico State University, for graciously opening his home to me for several weeks, as well as for his incredible teaching and instruction in the art of microchemistry. I would also like to acknowledge and sincerely thank both Dr. Scott Boroughs and Dr. Owen Neill at the Peter Hooper GeoAnalytical Lab at Washington State University for their help and guidance in utilizing the electron microprobe and microdrill for my data collection and analysis.

A hearty appreciation and thanks to Central Washington University, the Geological Society of America, Sigma Xi, and GeoEngineers for providing funding for this project, as well their generous financial and academic support.

Many thanks are due to my fellow graduate and undergraduate students, as well. You are my colleagues, and you are dear friends. I express a special thank you and much love, to my thesis buddy, Brittany Fagin, and my cherished volcano buddy, Sylvana Bendaña. The friendships and camaraderie shared in these years have been imperative in my pursuit of this Master's degree. Thank you all for the support, encouragement and fellowship shared amidst challenges and adversity, revelry and triumph.

My family has been a pillar of strength throughout these years of pursuing a Master's in Geology, and I wish, with utmost gratitude, to thank my parents, Kip and Mary Nelson, for all of their love, affirmation, care, provision and example. Thank you for instilling in me a delight and appreciation for nature and Creation and thank you for encouraging me in this pursuit and dream. Also, to my siblings, Emily and Zach, thank you for all of the fun and memories shared, and for those grand moments sifting through rocks together on the shores of Lake Superior. We'll hunt for more agates in the years to come.

This thesis is dedicated to loved ones who have departed from this earth in these recent years. Each lived lives so worthy of example, and I wish for this endeavor, dream and accomplishment to be completed in their honor and their memory. I would like to mention my grandparents, Kenneth and Florence Nelson, and Arthur and Norma Erickson. In life, they imparted great love, deep faith and infinite precious memories. I also dedicate this work to the memory of a dear friend and neighbor, Mr. Terry Bartness. He gave richly of his time and wisdom, offered deep encouragement and filled our days

with joy and laughter. He possessed an extraordinary way of making everyday moments special, and instilled in me a greater love and passion for learning.

Finally, I must thank my Lord and Savior, Jesus Christ, for the wonder and beauty of His Creation, the many opportunities to pursue and enrich my passion for geology, and for His abundant grace and kindness, in every walk of life.

TABLE OF CONTENTS

TABLE OF CONTENTS (continued)

Chapter Page

LIST OF TABLES

LIST OF FIGURES

LIST OF FIGURES (continued)

LIST OF FIGURES (continued)

LIST OF FIGURES (continued)

CHAPTER I

INTRODUCTION

Understanding the structure, evolution, and magmatic pathways at work within a volcano's magma storage and transport system is essential for the improvement of associated eruptive hazards prediction and mitigation. The documentation of external features, such as eruption frequency, magnitude of ground deformation prior to eruption, and volume of erupted material informs scientists about the temporal and spatial evolution of a magmatic system (Caracausi *et al.*, 2003; Patanè *et al.*, 2006). Furthermore, the collection and analysis of compositional data allow volcanologists to document the thermo-chemical origin and evolution of magmas, providing insight into subvolcanic processes that influence eruption style and volatility (Métrich *et al.*, 2004; Schiano *et al.*, 2001; Tonarini *et al.*, 2001). As such, characterization of the magmatic processes that impact a volcanic system is crucial for the improved assessment of volcanic hazards, and ultimately helps to preserve both property and life.

Mount Etna is a tremendous outdoor laboratory, ranking among the world's most well-documented volcanoes, with written records extending back to the Ancient Greek times (~700 BC) (Branca *et al.*, 2013; Coltelli *et al.*, 2000; Tanguy, 1981). Throughout its dynamic eruptive history, it has shaped and influenced the profile and culture of its surrounding cities and villages. It brings not only destruction and peril, but also opportunity by providing environmental, economic and social potential in the form of breathtaking landscapes, tourism and agriculture (Mercatanti, 2013). In addition, its nearly continuous eruptive activity—among the most frequent, and most-actively studied

in the world—has allowed geoscientists to explore important scientific questions regarding its magma dynamics, differentiation processes, patterns of volcanism, and eruptive mechanisms (Armienti *et al.*, 2004).

Despite broad and extensive research on the Mt. Etna volcano, however, there is much of its nature that remains enigmatic, inviting further, detailed study. The relationships among its complex geodynamic setting, its magmatic source(s) and pathways, and the structure and evolution of its magma storage and transport system, are not fully resolved. Additionally, an intriguing geochemical and isotopic signature, marked by a gradual increase in select alkali elements, such as K, Rb, Cs and elevated $^{87}Sr/^{86}Sr$ ratios has appeared since the 17th century (Condomines *et al.*, 1995; Peccerillo, 2005; Tanguy *et al.*, 1996; Tonarini *et al.*, 2001; Viccaro and Cristofolini, 2008; Viccaro *et al.*, 2010).

Since 1971, this alkali-enrichment signature has increased dramatically. Associated eruptions occur with higher frequency, are more explosive and voluminous, and are accompanied by more seismicity and increased CO_2 emissions (Aiuppa *et al.*, 2002; Caracausi *et al.*, 2003; Ferlito *et al.*, 2009; Kamenetsky *et al.*, 2007; Tanguy *et al.*, 1997; Viccaro *et al.*, 2006). Research identifying the source of this shift in geochemical and eruptive behavior is highly polarized, with evidence for a contribution from the mantle (Doglioni *et al.*, 2001; Gvirtzman and Nur, 1999; Métrich *et al.*, 2004; Peccerillo, 2005; Schiano *et al.*, 2001; Tonarini *et al.*, 2001; Viccaro *et al.*, 2008) vs. magmatic interaction with a crustal contaminant (Armienti *et al.*, 2004; Clocchiatti *et al.*, 1988;

Corsaro and Pompilio, 2000, 2004; Michaud, 1991, 1995; Pitcher, 2011; Viccaro and Cristofolini, 2008; Viccaro *et al.*, 2010).

Collecting *in situ* plagioclase data, in conjunction with whole rock and geochemical analysis, Pitcher (2011) produced strong evidence for alkali-enrichment of a late-stage, upper crustal origin. However, because plagioclase crystallization is limited to depths of <8 km below Earth's surface, information about crystallization pathways below this level is necessary in order to build a crustal-scale understanding of Etna's magma storage system as well as to fully elucidate the source of alkali-enrichment. Clinopyroxene is documented to crystallize at deeper levels than that of plagioclase, extending from the upper crust (<6 km) to below the Moho (~27 km), allowing for a more comprehensive evaluation of the magmatic system and the origin of the alkali-enrichment signature (Armienti *et al.*, 2007).

Due to its early appearance on the liquidus, ubiquity within Etnean lavas, and a relatively high Sr content, clinopyroxene represents an excellent probe of the Etnean subvolcanic plumbing system, magma source dynamics, and constraints on the timing and source of the alkali-enrichment event (Armienti *et al.*, 2007; Ghiorso, 2002). By documenting *in situ* clinopyroxene textural, geochemical, and geobarometric data as well as $^{87}Sr/^{86}Sr$ ratios in six historic (pre-1971) samples: 1329, 1566, 1669 (2 samples), 1886 and 1964, as well as four recent (post-1971) samples: 1974, 1981, 2001, and 2004, this study aims to characterize the spatial and temporal evolution of the Mt. Etna magma and transport system over ~700 years, from 1329 to 2004 AD.

Initial characterization of the sample suite involved petrographic and back-scattered electron (BSE) imaging to characterize the sizes and textures of selected pre- and post-1971 clinopyroxene. Following textural analysis, clinopyroxene, representing a broad range of sizes and textures, was selected for *in situ* geochemical analysis, which documented compositional variations in select major and trace elements. Clinopyroxene pressure calculations were then performed using the Putirka *et al.* (2003) geobarometer, after Armienti *et al.* (2012). Finally, clinopyroxene microsampling was performed on a select suite of clinopyroxene cores and rims from pre- and post-1971 samples, representing a broad range of textures, geochemical variations and calculated pressures; this was followed by $^{87}Sr/^{86}Sr$ isotope analysis via thermal ionization mass spectrometry (TIMS).

Texturally and geochemically, clinopyroxene display heterogeneity in both pre- and post-1971 samples. Clinopyroxene crystallization is documented from below the Moho (27 km) to the upper crust (<6 km), with a dominant range at approximately 8.7-16.5 km depth. A distinct population of clinopyroxene within the 1886 and post-1971 samples displays elevated weight percent CaO values and demonstrates pressures consistent with levels of the carbonate substratum beneath Mt. Etna, providing new evidence for carbonate assimilation processes. Additionally, a group of anomalously radiogenic clinopyroxene cores may suggest the formation of a magmatic skarn beneath the volcano. Furthermore, regarding $^{87}Sr/^{86}Sr$ values, clinopyroxene are generally in disequilibrium with associated whole rock, while core-rim relationships and recorded

pressures bear evidence supporting the crystallization of clinopyroxene from a relatively radiogenic source at a late-stage and in the mid- to upper crust.

These *in situ* clinopyroxene analyses provide a window into the primary magmatic pathways recorded by the clinopyroxenes as they grew and resided within the subvolcanic plumbing system. Each crystal's unique petrogenetic history reflects the magmatic growth environment and conditions that existed at the time of its crystallization and residence within the Etna magmatic system. Such information provides insight into the evolution of the plumbing structure, and context by which to better constrain and evaluate the origin of alkali-enrichment. Integration of these data, in conjunction with whole rock data and scientific literature, provides constraints on primary crystallization and magma storage zones, as well as insight into the interactions of magma recharge and mixing, assimilation, and fractional crystallization processes within a transport system composed of an interconnected plexus of dikes and sills. Additionally, new evidence supporting the interaction of magmas with the Hyblean Plateau, a carbonate succession of limestone, $CaCO_3$ and dolomite, $CaMg(CO_3)_2$ (Heap *et al.*, 2013; Michaud, 1995) lying beneath the Etnean edifice, is presented. This dominant interaction may occur alongside and/or be initiated by magmatic recharge and mixing dynamics. Ultimately, these data evaluations and interpretations allow for a reconstruction of magmatic processes that have impacted Mt. Etna over the last 700 years, from 1329 to 2004 AD. Such documentation may contribute new insights into the volcano's historic and recent eruptive history, thus informing the prediction of volcanic hazards and helping to protect commerce and life.

CHAPTER II

BACKGROUND

Location and Geodynamic Setting

Mt. Etna is a quaternary, basaltic stratovolcano that is located on the northeastern coast of Sicily, Italy (Figure 1) and towers over the adjacent Ionian Sea. Extending over an area of approximately 1,250 km^2 and rising 3,340 meters above sea level at its summit, Europe's largest volcano is host to nearly continuous seismic and magmatic activity (Mercatanti, 2013; Patanè *et al.*, 2011). Dominating the fertile and densely inhabited landscape provided by its nutrient-rich lava flows, Mt. Etna is both a benefactor and a hazard to the nearly 1.3 million people who live near its base, supporting – as well as imperiling – the region's population, tourism, and commerce. Over the past four decades,

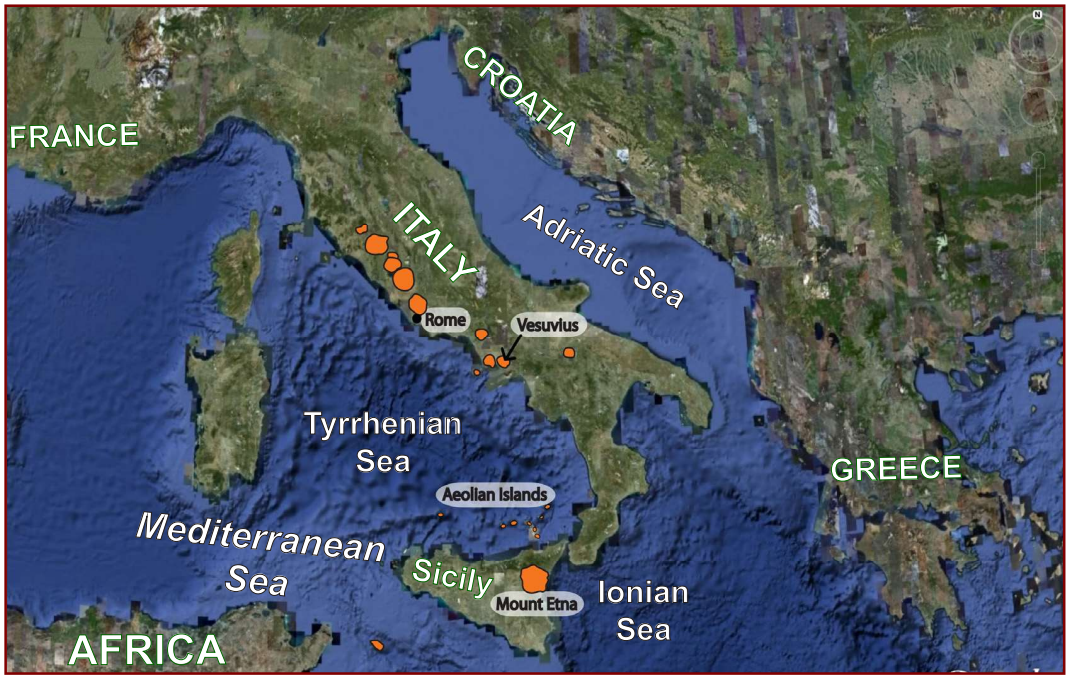

Figure 1. A Google Earth™ image showing the location of Mount Etna, and the other major volcanic centers of Italy (in orange), including the calc-alkaline Aeolian Islands and Mount Vesuvius, from Moses (2010).

chemical changes in Etna's erupted products, including enrichment in K and Rb and increases in $^{87}Sr/^{86}Sr$, have coincided with an increase in eruption frequency and explosivity, underscoring the importance of volcanic hazard prediction and mitigation in response to this enhanced liability and risk.

Plate Tectonic Setting

Mt. Etna is positioned in the center of the Mediterranean Basin, one of the most tectonically and geodynamically complex regions in the world (Şengör, 2009). This area has been shaped largely by the collision between the European and African plates and associated microplates (Barberi *et al.*, 1974; Bonaccorso *et al.*, 1996; Carminati *et al.*, 2006). The volcano resides on the accretionary prism of the Africa-Europe subduction system where three primary structural domains are in contact (Figure 2a): 1) to the north is the collision zone between the African and European plates represented by the Apennine-Maghrebian overthrust belt (Apenninic-Maghrebian Chain, European Plate) 2) to the south, the relatively undeformed northern margin of the African Plate (Hyblean Plateau), which plunges under the Gela-Catania foredeep and the Apenninic-Maghrebian Chain to the north, and 3) to the east, the oceanic lithosphere of the Ionian Sea. (Cristofolini *et al.*, 1985; Paris *et al.*, 1997; Scribano *et al.*, 2008). Mt. Etna's basaltic volcanism developed near the intersection of the Gela-Catania Foredeep, the Apenninic-Maghrebian Chain and the Hyblean Plateau foreland (Figure 2b) (Ben-Avraham and Grasso, 1990; Lentini, 1982). In addition, north of Sicily, the calc-alkaline Aeolian volcanic arc (Figure 1) results from the active subduction of the Ionian oceanic lithosphere beneath Tyrrhenian lithosphere of the European plate.

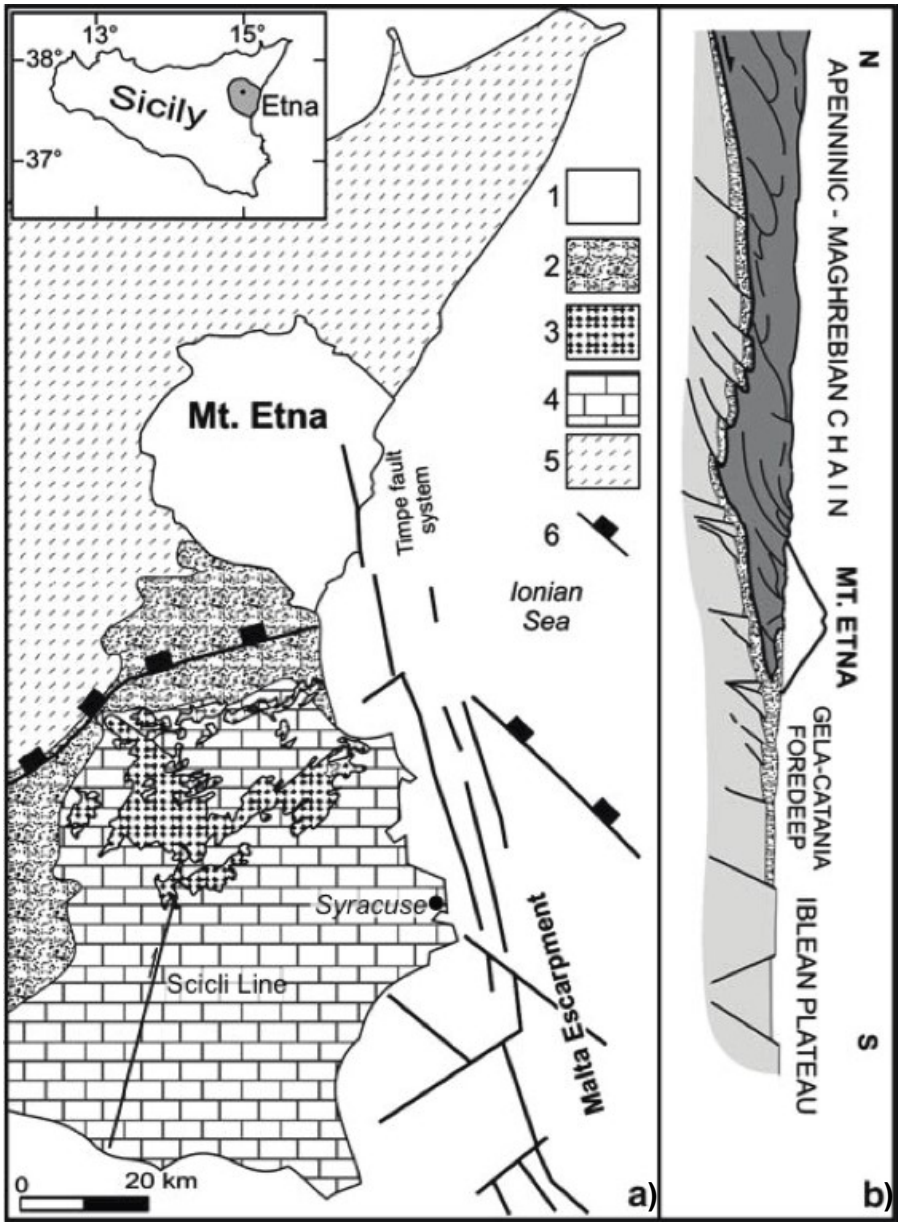

Figure 2. a) Main geological and tectonic features of eastern Sicily. Legend with representative symbols is located in upper right corner: 1) Mt. Etna volcano, 2) Gela-Catania Foredeep, 3) Late Miocene-early Pleistocene Hyblean volcanics, 4) Hyblean (Iblean) Plateau (African Plate), 5) Apenninic-Maghrebian Chain (European Plate), 6) Compressive front of the Apenninic-Maghrebian Chain. The Malta Escarpment and Timpe fault system and N-S Scicli Line dextral strike-slip fault are also shown. b) A schematic cross-section along eastern Sicily, highlighting the location of Mt. Etna and its geological profile, from Branca *et al.* 2008 (redrawn after Lentini *et al.*, 1996).

Geology and Structure

Mt. Etna's geologic profile consists of a basaltic cover approximately 1.5 km thick that rests upon a ~2 km thick sub-volcanic sedimentary and metamorphic basement composed of a mélange of marly clays, marly limestone and quartz-arenitic rocks of the flyschoid series of the Apenninic-Maghrebian Chain (Catalano *et al.*, 2004; Grasso and Lentini, 1982; Heap *et al.*, 2013; Lentini, 1982; Michaud, 1995; Pedley and Grasso, 1992). This sequence unconformably overlies the autochthonous carbonate unit of the Hyblean Plateau, which is inferred to begin at a depth of ~5 km beneath the Mt. Etna edifice and has an average thickness of 10 km, extending to an average depth of 15 km beneath Mt. Etna (Di Stefano and Branca, 2002; Grasso and Lentini, 1982; Heap *et al.*, 2013; Lentini, 1982; Pedley and Grasso, 1992; Romano *et al.*, 1979; Yellin-Dror *et al.*, 1997). The Hyblean Plateau forms a tectonically stable block at the northern margin of the undeformed African Plate (Bonforte and Sturiale, 2008; Branca *et al.*, 2004; Michaud, 1995; Romano *et al.*, 1979) and represents an autochthonous carbonate sequence of Triassic to mid-Pleistocene age defined by a succession of limestone and dolomite, with intercalated submarine and sub-aerial lava flows of tholeiitic and alkaline affinity (Grasso and Lentini, 1982; Grasso *et al.*, 1983; Lentini, 1982; Musumeci *et al.*, 2014; Pedley and Grasso, 1992).

Several fault systems propagate through the central Mediterranean, the most prominent of which is the NNW-SSE trending Malta Escarpment (Figure 2) (Argnani and Bonazzi, 2005; Bousquet and Lanzafame, 2004; Lanzafame and Bousquet, 1997). The Malta Escarpment represents the interface of the Sicilian continental crust and the

Mesozoic oceanic crust of the Ionian Basin and is interpreted as an active right-lateral transtensional fault system (Argnani and Bonazzi, 2005; Bousquet and Lanzafame, 2004; Doglioni *et al.*, 2001; Paris *et al.*, 1997). Extending northward from Malta (not pictured) along the southeastern coast of Sicily to the eastern base of Mt. Etna, the tectonic system progresses across northeastern Sicily, before continuing into the Tyrrhenian Sea (Bousquet and Lanzafame, 2004). As the Malta Escarpment impinges on the lower eastern flank of Mt. Etna, it forms a dominant, highly seismogenic surface feature called the Timpe normal fault system (Bousquet and Lanzafame, 2004; Branca *et al.*, 2004; Doglioni *et al.*, 2001; Patanè *et al.*, 2011).

Volcanism of Eastern Sicily

Hyblean Volcanism

Eastern Sicily possesses two primary domains that represent the evolution of volcanism within the region: the Hyblean Plateau, and the area surrounding the modern Mt. Etna edifice. Beginning in the Late Triassic, two primary extensional tectonic phases induced volcanism on the African continental margin (Carbone *et al.*, 1982; Finetti *et al.*, 1996). Volcanism ceased from the Upper Cretaceous to early Miocene (about 70-15 Ma) due to a stage of continental collision and reinitiated on the north side of the Hyblean Plateau in the late Miocene (Ben-Avraham and Grasso, 1990; Branca *et al.*, 2004). Gradual northward migration in volcanism continued through the middle Pleistocene, extending beyond the northern boundary of the Plateau into the modern Etnean region, as evidenced by gravimetric work and drill sampling within the foredeep sediments on the Catania Plain (Branca *et al.*, 2004; Grasso and Ben-Avraham, 1992; Longaretti *et al.*,

1991). This volcanic succession, known as the Hyblean Volcanics, is represented by both submarine and subaerial eruptions and is of tholeiitic to alkaline affinity (Carveni *et al.*, 1991; Schmincke *et al.*, 1997). According to Continisio *et al.* (1997), Hyblean volcanism ceased as movement along the Scicli Line fault (Figure 2) ended in the Pleistocene.

Etnean Volcanism

Based on stratigraphic and structural data, the evolution of Etnean volcanism has been divided into four main phases by Branca *et al.* (2004): the Basal Tholeiitic Phase, the Timpe Fault Phase, the Valle del Bove volcanic centers, and the formation of the modern stratovolcano (Figure 3a-d). The oldest phase, represented by the basal tholeiite series (Figure 3a), began about 500 ka with scattered submarine to subaerial, low-K_2O, tholeiitic fissure-type volcanism (Armienti *et al.*, 2012; Branca *et al.*, 2008; Condomines *et al.*, 1982). This series shares chemical, petrologic, and geographic characteristics with the Hyblean Volcanics, suggesting a genetic relationship between the two volcanic successions. The transition from submarine to subaerial eruptions took place primarily due to regional uplift (Di Stefano and Branca, 2002).

The Timpe Fault Phase (Figure 3b) began approximately 220 ka along the eastern coast of Sicily and the NNW-SSE oriented Timpe fault system and forms a small shield volcano, which today represents the lower southeastern flank of Mt. Etna. The significance of this phase is highlighted by the gradual transition from tholeiitic to subalkaline to Na-alkaline affinity as the primary eruption style progressed from fissure-type volcanism to monogenetic center-type volcanism (Branca *et al.*, 2004, 2008; Corsaro and Pompilio, 2004; Romano, 1982).

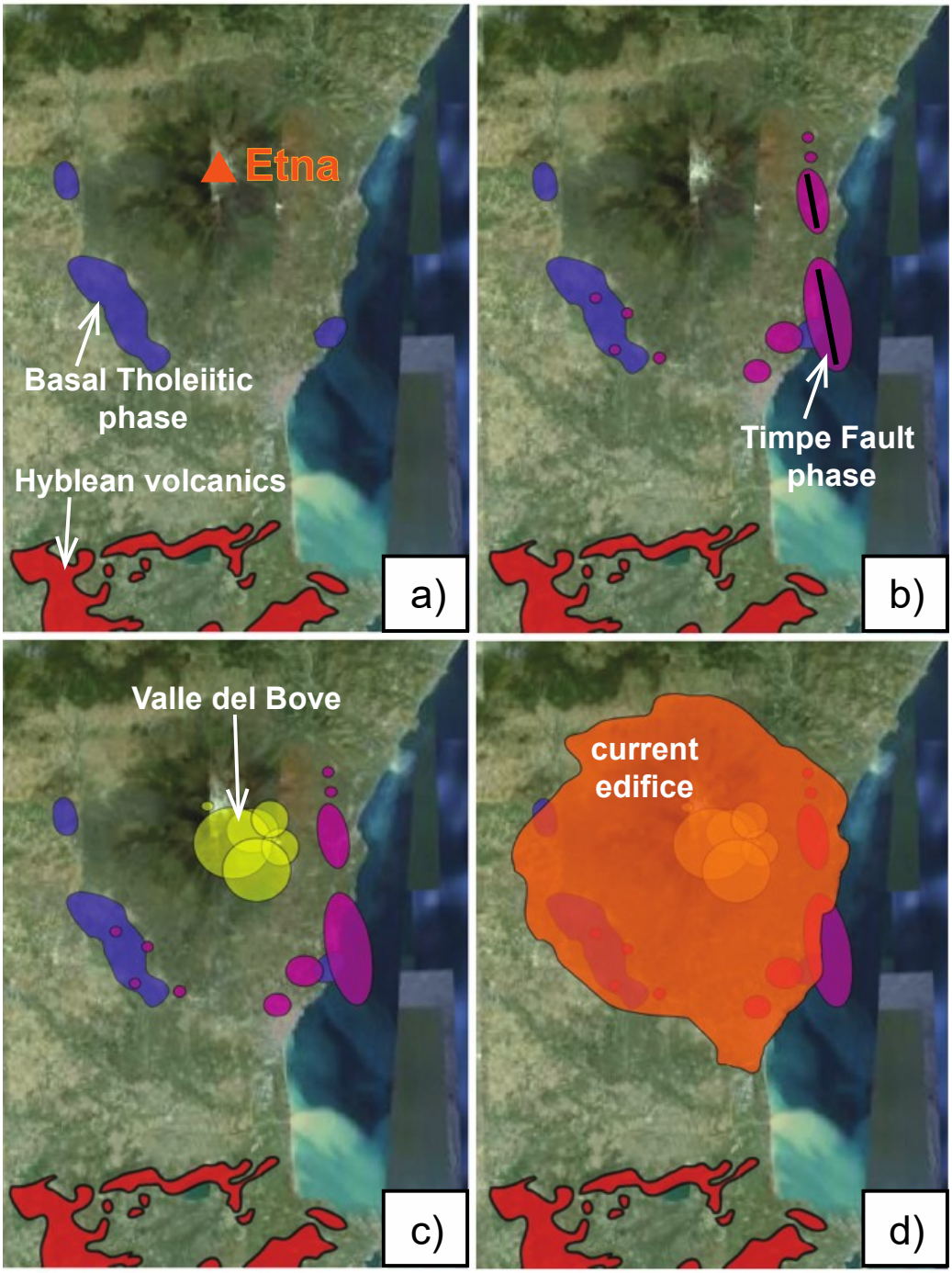

Figure 3. Schematic representation of Etnean volcanism evolutionary phases, superimposed on a Google Earth™ image, from Moses, 2010 (modified after Branca *et al.,* 2004). The snow-capped peak in the upper center of the image defines modern Mount Etna, whereas the Hyblean Volcanics are defined by red. a) Mapped extent of the Basal Tholeiitic phase (purple), b) Timpe Fault phase (pink, black lines represent Timpe faults), c) Valle del Bove volcanic centers (yellow) and d) current edifice (orange).

A main westward shift of the primary magma feeding system relative to the migration of the extensional regime of the Timpe fault system, marks the Valle del Bove volcanic centers phase (Figure 3c), beginning about 120 ka with the construction of a series of nested polygenetic volcanic centers. Throughout this stage, the magma ascent path through the crust became gradually more localized, resulting in more efficient plumbing systems; this is marked by the temporal transition from eruption of smaller, scattered volcanic centers to larger, more stable ones. Deposits from this period consist of thin lava flows of alkaline affinity and volcanoclastic and autoclastic units that are similar in composition and eruption style to those of modern Mt. Etna (Branca *et al.*, 2004, 2008).

The final stage of the evolution of Etnean volcanism, the formation of the modern stratovolcano (Figure 3d), occurred after the final northwestward shift of the feeder, and is marked by the definitive stabilization of the plumbing system. During this phase, a steady conduit remained active for about 60 kyr, experiencing continuous magma intrusion. This condition promoted efficient magma transport from the mantle to the surface, allowing for a consequent increase in magma ascent rate and eruption frequency, thus leading to the growth of a large stratovolcano. Branca *et al.* (2004) divide this stratovolcano development phase into two periods: Ellittico activity and Mongibello activity. The Ellittico volcano was active from ~60 to 15 ka and is characterized by massive to laminated lava flows, autobrecciated deposits and pyroclastic deposits. This period of volcanic activity ended at 15 ka with the occurrence of four caldera-forming eruptions. Finally, the Mongibello period represents the formation of the modern basaltic

stratovolcano, which is defined by Mt. Etna's present edifice and active volcanic center (Branca *et al.*, 2004, 2008). This period has been characterized by a wide range of eruptive styles, from effusive and mildly strombolian to sub-plinian (Romano, 1982; Romano *et al.*, 1979). The historical and recent evolution of Mt. Etna's activity will be discussed in further detail below.

Sources of Magmatism

Due to its complex evolution and geodynamic setting, the mantle source region(s), plumbing structure, and differentiation history of Mt. Etna is challenging to fully elucidate. Mt. Etna resides on Sicilian continental crust, yet helium and carbon isotopic signatures suggest a mantle source similar to that of mid-ocean ridge basalts (Allard *et al.*, 1991, 1997; Barberi *et al.*, 1974; Condomines *et al.*, 1982; Tanguy, 1978). Such chemical indicators contrast with those of the calc-alkaline Aeolian island arc directly to the north (Barberi *et al.*, 1974; Doglioni *et al.*, 1998; Gvirtzman and Nur, 1999), which is related to the subduction of the Ionian microplate beneath Tyrrhenian lithosphere.

Despite residing near major plate boundaries, Mt. Etna displays some characteristics similar to those of an intra-plate volcano. While most volcanism on Earth is located near tectonic plate boundaries, intra-plate volcanism has been attributed to the mantle plumes, which results in hotspot volcanism. The plume model suggests that localized, buoyant upwelling of the lower mantle rises to the surface (Morgan, 1971, 1972; Schellart, 2010a). Several petrological and geochemical studies (Allard *et al.*, 1997; Clocchiatti *et al.*, 1998; Condomines *et al.*, 1982; Patanè *et al.*, 2006; Tanguy,

1978; Tanguy *et al.*, 1996, 1997) support the mantle plume model to explain Mt. Etna's magmatism. The observed spatial and temporal transition from tholeiitic to alkaline magmas and the late Quaternary deformation of eastern Sicily suggest that mantle upwelling has resulted in the development of a deep magma reservoir and temporary shallow chambers within the crust where differentiation occurs via magmatic processes such as polybaric crystal fractionation and selective wall rock assimilation (Tanguy, 1978; Tanguy *et al.*, 1996).

Several other researchers suggest that select structural features at Mt. Etna may explain its magmatism. Cristofolini *et al.* (1979) and Rittmann and Sato (1973) infer that the intersection of three main fault systems at Mt. Etna, trending ENE, NNW and WNW, has created a zone of weakness, leading to magma uprising. Other studies (Monaco and Tortorici, 2000; Paris *et al.*, 1997) propose that the extensional regime associated with the northern prolongation of the Malta Escarpment is related to dilatational strain that facilitates the migration of magma to the surface. Additionally, the instability of the eastern flank of the volcano has been cited as evidence for the decompression of the plumbing system, thereby promoting magma ascent (Branca, 2003; Neri *et al.*, 2004; Patanè *et al.*, 2011).

Although Sicily itself exhibits a lack of chemical and seismological evidence for subduction-related volcanism, several researchers suggest that Mt. Etna's formation may be related to nearby subduction processes (Anderson and Jackson, 1987; Bianchini *et al.*, 1998; Gvirtzman and Nur, 1999; Tanguy, 1978). Using primarily geochemical data, Schiano *et al.* (2001) suggest that over the last 500 ka, volcanic products at Etna preserve

a record of progressive transition from a mantle-plume dominated to a more arc-like expression, due to southwestward migration of the Ionian slab. They conclude that juxtaposition of a subducting slab and a mantle plume beneath Mt. Etna has led to the magmas displaying a more prominent calc-alkaline signature and thus, a more explosive nature.

The importance of the Ionian slab in Etnean volcanism finds support from several other studies, as well. Constructing a three-dimensional model of the region's tectonics, Gvirtzman and Nur (1999) proposed that Mt. Etna's present edifice formed as a consequence of slab rollback, in which the slab migrates backward, thereby generating lateral flow in the mantle. In the case of the Ionian slab, such rollback motion resulted in decompression melting of asthenopheric material from beneath the adjacent African plate (Dvorkin *et al.*, 1993; Nur *et al.*, 1991). Doglioni *et al.* (2001) further develop this concept by proposing that the differential rollback of the continental lithosphere of Sicily and the denser, oceanic Ionian lithosphere kinematically produced right-lateral transtension along the Malta escarpment, thus opening a slab "window" (Figures 4a and 4b) (Doglioni *et al.*, 1998). Offering an alternative to the mantle plume model, Schellart (2010a and b) suggests that rollback has generated decompression melting of the upper mantle, therefore inducing upwelling around the Ionian slab edge and resulting in the episodic volcanism at Mt. Etna.

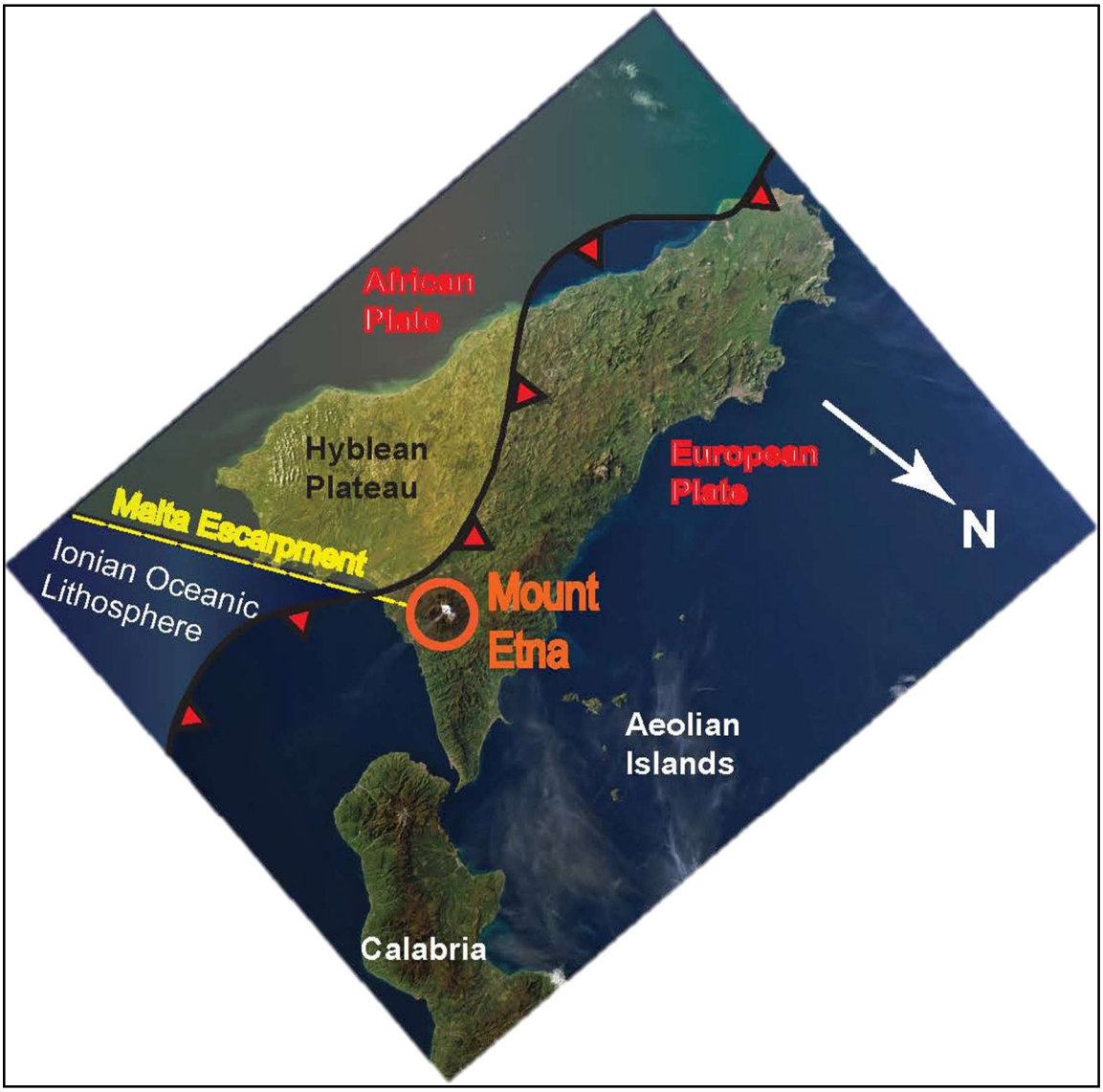

Figure 4a. Geodynamic setting of Mt. Etna. Map based on Gvirtzman and Nur (1999) and Armienti *et al.* (2004). Red teeth indicate the overriding plate.

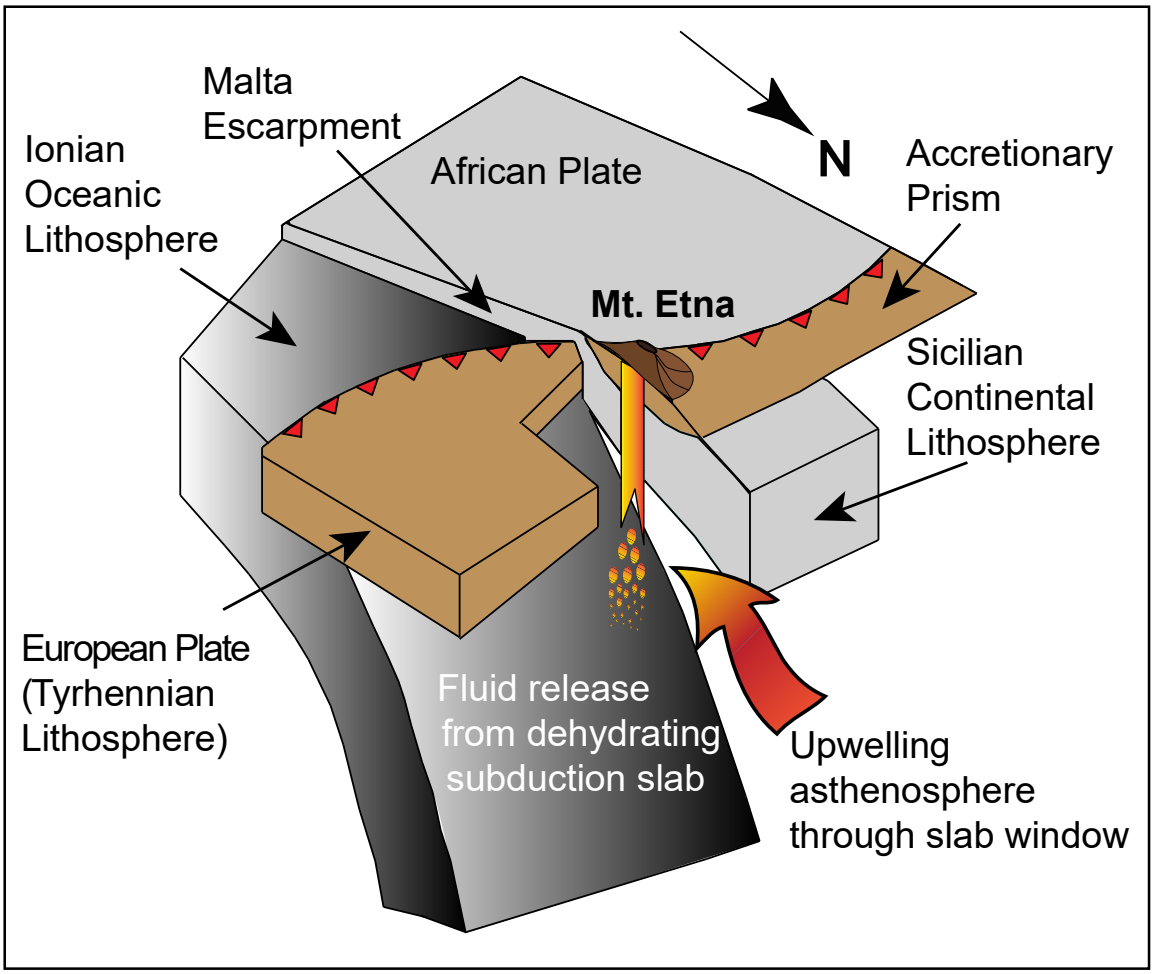

Figure 4b. Geodynamic setting of Mt. Etna. Interpretative block diagram of geodynamic structure beneath Mt. Etna, based on Gvirtzman and Nur (1999) and Armienti *et al.* (2004). Red teeth indicate the overriding plate.

Historical and Recent Evolution of Mt. Etna

Throughout the historical period, and particularly since 1329 AD, Mt. Etna has primarily produced effusive eruptions from summit craters or parasitic vents on its volcanic flanks, accompanied by degassing. Typical activity includes strombolian ejections or short-lived fire fountain episodes (Branca and Del Carlo, 2005; Viccaro *et al.*, 2010). Erupted lavas are generally highly porphyritic, plagioclase-rich K-

trachybasalts, with rare and highly explosive flank eruptions emitting nearly aphyric, plagioclase-poor basaltic-trachybasaltic magmas (Armienti *et al.*, 1988; Correale *et al.*, 2014; Corsaro *et al.*, 2009). Lavas erupted over the last 700 years have yielded data, such as whole rock and mineral geochemical and isotopic signatures, which indicate a complex subvolcanic magma reservoir (Tanguy *et al.*, 1997). Such complexity promotes magma differentiation and interaction at multiple levels in the feeding system, resulting in a complicated petrogenesis involving fractional crystallization, mantle recharge, magma mixing and crustal assimilation (Viccaro *et al.*, 2010).

Variable MgO whole rock data (Figure 5a) throughout this period indicate multiple pulses of magma recharge. Eruptive products also display a progressive increase in alkalinity, as demonstrated by whole rock $^{87}Sr/^{86}Sr$ and K/Nb signatures (Figure 5b-c). In the last 700 years, Etnean lavas have gradually become more alkaline, but since 1971, magmas have displayed a dramatic rise in selected alkali elements such as K, Rb and Cs, with a concomitant increase of $^{87}Sr/^{86}Sr$ (Tanguy, 1978; Tonarini *et al.*, 2001; Métrich *et al.*, 2004; Armienti *et al.*, 2007, 2012). Additionally, post-1971 volcanic eruptions are marked by slightly lower trace element concentrations of Th, U, Ta, Nb and Zr, and higher volatile content compared to historic (1329 to 1971) basaltic products (Peccerillo, 2005; Tanguy *et al.*, 1997; Tonarini *et al.*, 2001; Viccaro and Cristofolini, 2008; Viccaro *et al.*, 2010). This recent alkali-enrichment has been accompanied by greater seismicity and ground deformation, as well as the world's largest current emission of volcanic gases from a single volcano (Kamenetsky *et al.*, 2007). Furthermore, recent eruptions have

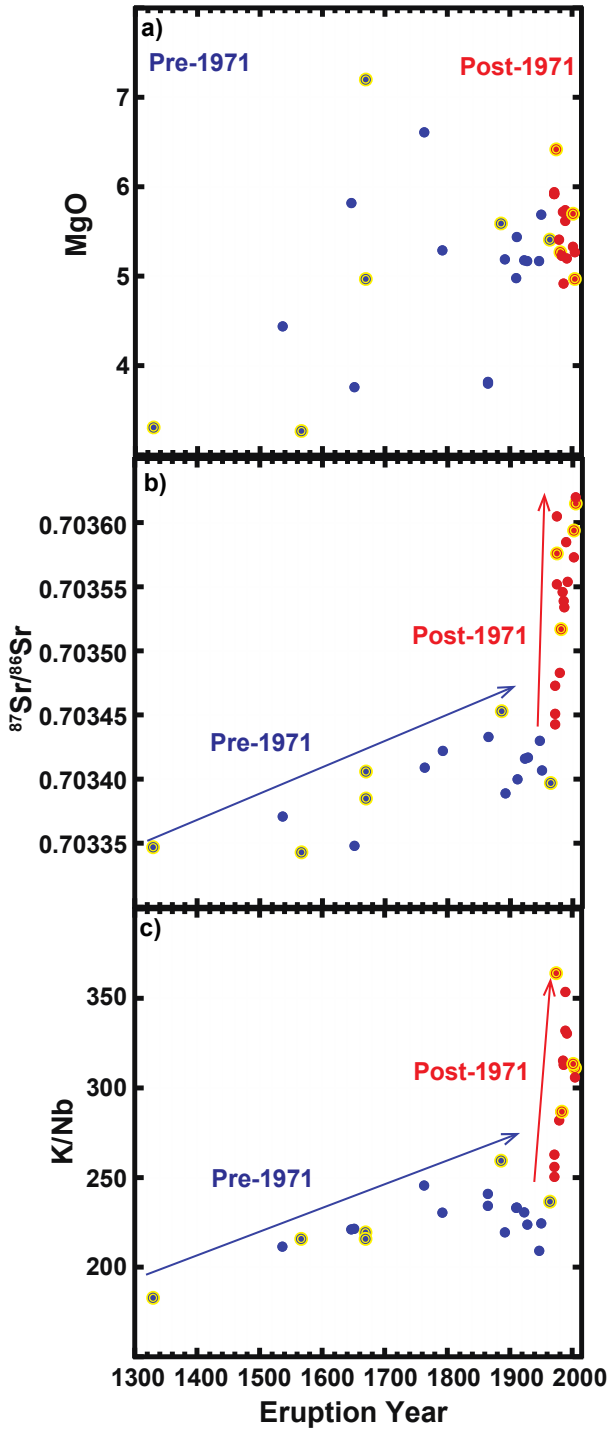

Figure 5. Eruption year vs. whole rock geochemical characteristics: a) MgO (wt. %), b) $^{87}Sr/^{86}Sr$, c) K/Nb. Blue symbols are pre-1971 samples and red symbols are post-1971 samples. Symbols highlighted in yellow are samples used in this study. Arrows highlight the observed alkali-enrichment signature in pre- and post-1971 samples. Unpublished data from Graham and Spera.

become more frequent, voluminous, and explosive (Tanguy *et al.*, 1996; Kamenetsky *et al.*, 2007; Viccaro *et al.*, 2010).

Alkali-Enrichment

Characterized by post-1971 potassium levels (K_2O ~2.2 wt.%, also refer to Figure 5c) that cannot be attributed to simple crystal fractionation, the source of this alkali-enrichment is controversial and widely debated, with end-member hypotheses of mantle vs. upper crust (e.g., Ferlito and Lanzafame, 2010). Citing the enrichment of fluid mobile elements in recent lavas and the influence of local and regional tectonics, one hypothesis proposes that the mantle has been infiltrated by subduction fluids due to a tear or 'window' in the Ionian slab near Mt. Etna (Doglioni *et al.*, 2001; Gvirtzman and Nur, 2001; Schiano *et al.*, 2001b; Tonarini *et al.*, 2001; Métrich *et al.*, 2004). In support of this suggestion, differences in Sr/Ba ratios and anorthite content of plagioclase in historic and recent lavas are interpreted by Viccaro et al. (submitted, Bulletin of Volcanology) to be due primarily to recharge of a geochemically distinct magma derived from heterogeneously metasomatized mantle.

The second hypothesis involves shallow contamination of the basaltic magmas due to the assimilation of rocks from the sedimentary basement and/or the role of associated crustal fluids (Armienti *et al.* 2004; Clocchiatti *et al.*, 1988b; Michaud, 1995; Pitcher, 2011; Tonarini *et al.*, 2001; Viccaro and Cristofolini, 2008; Viccaro *et al.*, 2010). Direct interaction of the magma and crustal wall rocks has been documented in crustal xenoliths that were sampled during phreatomagmatic eruptions and when magma violently ascended through the volcanic conduits (Clocchiatti *et al.*, 1988; Michaud,

1995; Michaud *et al.*, 1988). These xenoliths include siliceous, peraluminous, carbonate and composite lithologies, which exhibit a wide range of petrologic and mineralogical features, reflecting the heterogeneity of the crustal basement beneath Mt. Etna's edifice (Michaud, 1995).

Mt. Etna's Historical and Recent Petrogenetic Record: Constraints from Mineral Phases

Thermodynamic modeling and geobarometry show that Mt. Etna's magma system extends from the Moho to the upper crust (~0.2 GPa, ~6-6.6 km, Putirka et al. 2003; Armienti et al. 2007), with plagioclase crystallizing at shallow depths (<8 km, Moses, 2010). Combining new plagioclase data with existing whole rock analyses, Pitcher (2011) produced strong evidence for alkali-enrichment of an upper crustal origin by comparing pre- and post-1971 plagioclase cores and rims as well as whole rock and groundmass data. His work demonstrated that higher K is displayed exclusively in the rims of post-1971 plagioclase, compared to rims of pre-1971 crystals and cores of both pre- and post-1971 plagioclase. In addition, *in situ* Sr isotope analyses of groundmass are more radiogenic than whole rock. These data strongly indicate that a component of the alkali-enrichment is late-stage and due to interaction of magma with the upper crust. However, because plagioclase crystallization is limited to the upper 8 km below the Earth's surface (Moses, 2010), information about crystallization pathways below this level (>8 km) is necessary in order to build a crustal-scale understanding of Etna's magma storage system as well as to fully elucidate the origin of alkali-enrichment.

Geobarometry documents clinopyroxene crystallization beginning at depths below the Moho up to ~0.2 GPa (<6 km), allowing for comprehensive evaluation of the Etnean plumbing system and its magmatic pathways (Armienti *et al.*, 2007; Putirka *et al.*, 2003). In order to probe Mt. Etna's deep-seated magmatic processes, Armienti *et al.* (2007) applied the Putirka *et al.* (2003) clinopyroxene-liquid geobarometer to historical and recent lavas for clinopyroxene-whole rock pairs, in conjunction with an evaluation of whole rock and clinopyroxene $^{87}Sr/^{86}Sr$ as well as crystal size distribution. Through reconstruction of clinopyroxene crystallization histories, this study produced a temporal and spatial characterization of the magmatic system and its alkali-enrichment. Geobarometry results revealed a range of clinopyroxene growth from ~0.2-1.8 GPa (~2-18 kbar, ~6-54 km), from mantle depths to the upper crust, demonstrating polybaric ascent and magmatic ponding at multiple depths in the system. Furthermore, Sr isotope disequilibrium between the clinopyroxene and their corresponding whole rocks was interpreted to represent the presence of crystal mushes at various depths within the system. Disequilibrium is inferred to be induced as these crystal mushes interact with fresh magma batches supplied by an isotopically heterogeneous mantle source (Marsh, 2004).

In Situ Analysis of Volcanic Crystals

Magma chambers are host to a number of processes that diversify the chemical, mineralogical, and textural features of a magma (Spera and Bohrson, 2001). A primary melt is produced directly from its source rock but is subject to many physical and chemical modifications as it rises; a derivative magma is the ultimate product. Among the

most important processes that alter a magma's chemistry include the closed system process of fractional crystallization, and open system processes of crustal assimilation and magma recharge/magma mixing. These processes typically act when magmas are stalled in crustal reservoirs (Hess and Head, 1990), and because composition is an important influence on eruption style, documentation of these processes has the potential to improve prediction and mitigation of volcanic hazards within areas of high-risk.

As fractional crystallization, crustal assimilation and magma recharge/magma mixing occur, the composition of the magma changes. Minerals (solids) that precipitate from melt in response to these processes record these compositional changes over time. Amazingly, this record of change is preserved within the mineralogical, geochemical and textural features of crystals in a solidified melt (Blatt *et al.*, 2006; Davidson *et al.*, 2007; Tepley *et al.*, 2000). Representing a time sequence from older to younger in the progressive layers or growth zones of a crystal, this concept can be compared to basic lithographic stratigraphy, albeit at a much smaller, microscopic scale (Davidson *et al.*, 2007). These crystals are eventually erupted from the magma chamber along with the surrounding magma; this mass eventually solidifies as a rock, which can then be collected for analysis.

Crystal isotope stratigraphy is a powerful and revealing tool in which the ratios of radiogenic isotopes from the core to rim of a crystal provide potentially diagnostic information concerning the petrogenetic history of magmas. Acting as a petrogenetic 'DNA', these isotopic ratios, along with corresponding textural and major and trace element features, may be assessed and decoded through a variety of analytical techniques,

which have evolved over the last 20-30 years (Davidson *et al.*, 2007). Recent technological advances have reduced the spatial resolution (e.g., 10-100 microns) at which isotopic and elemental changes in mineral composition can be documented. At the time a crystal initially grows, its isotopic composition is identical to that of the host magma from which it is derived. Changes in the isotopic composition of the melt that reflect addition of magma through mixing or crustal assimilation will be reflected in the changing isotopic composition of crystal layers that are added as growth continues. *In situ* analysis therefore affords the opportunity to document and probe the magmatic pathways recorded by a crystal as it resided within a magmatic system.

In order to document an accurate magmatic history for a particular sample, a number of specific criteria apply to the use of crystal stratigraphy. Ideally, a mineral species should record as much of the magmatic history as possible, extending from the liquidus to the solidus, thereby recording all of the processes that influence magma composition (Davidson *et al.*, 2007). Thus, use of minerals that are stable over a range of pressure and composition (including H_2O) is optimal (Martin *et al.*, 2010). Conversely, it is also important that the crystal produces a record of these magmatic processes, and thus ideally, should change composition with evolution. Crystal size and abundance are also a factor; more abundant and larger crystals are advantageous. The final critical aspect to be considered is sufficient abundance of isotopically-relevant elements such as Sr, Pb, and Nd (Davidson *et al.*, 2007). Below, two cases studies are presented that highlight the use of *in situ* analyses to document magmatic processes that contribute to magma evolution.

Case Study #1: Magmatic Processes Recorded in Plagioclase at El Chichón Volcano

In order to constrain and document the dynamic magmatic and mixing processes occurring at trachyandesitic El Chichón Volcano, Mexico throughout its 200 ky history, Tepley *et al.* (2000) applied crystal isotope stratigraphy to plagioclase phenocrysts from select eruptions. Applying Nomarski interferometry, electron microprobe analysis, micromilling techniques and thermal ionization mass spectrometry, Tepley *et al.* (2000) examined changes in textures, An content and $^{87}Sr/^{86}Sr$ ratios along the growth profiles of 11 crystals, successfully identifying the magmatic pathways recorded by the plagioclase during its residence in the magmatic system.

Plagioclase cores were systematically enriched in radiogenic Sr compared to their respective rims, with widely fluctuating An contents and complex textural zoning, demonstrating a dynamic thermal and compositional system. These isotopic, compositional and textural patterns were inferred to represent an initial period of high-level, high-$^{87}Sr/^{86}Sr$ crustal assimilation of the magma, based upon the highly radiogenic cores. The magma then evolved through frequent recharge events to a low-$^{87}Sr/^{86}Sr$ magma, as evidenced by the presence of complex disequilibrium textures and oscillations in An content.

Case Study #2: Sr Isotope Disequilibrium in Columbia River Flood Basalts

To characterize the deep mantle vs. shallow crustal contributions of geochemical variability in the Columbia River flood basalts of the northwestern United States, Ramos *et al.* (2005) applied *in situ* Sr isotope analysis along core-to-rim transects of plagioclase and in groundmass from select lava flows. Microdrilling, chromatographic purification

procedures and Laser Ablation-Multicollector-Inductively Coupled Plasma Mass Spectrometry (LA-MC-ICPMS) provided Sr isotope data, which revealed the occurrence of rapid, late-stage open-system magmatic processes operating at crustal levels.

Results demonstrated internal $^{87}Sr/^{86}Sr$ zoning in plagioclase phenocrysts and isotopic disequilibrium between the plagioclase and their more-enriched host groundmass. $^{87}Sr/^{86}Sr$ profiles of the plagioclase phenocrysts generally exhibited minor internal oscillations or gradual increase toward the rims of the crystals, with one crystal exhibiting an internal rimward decrease in $^{87}Sr/^{86}Sr$. Such oscillations are inferred to represent repeated open-system processes, such as recharge and minor crustal-magma interaction during crystal growth, while the enriched rims and groundmass may be inferred to reflect late-stage crustal contamination. Overall, this study revealed that the geochemical distinctions of these lavas were largely gained shortly prior to eruption, while crystal isotope stratigraphy techniques allowed for the elucidation of magmatic history and evolution on a fine spatial scale.

CHAPTER III

METHODS

The samples from eruption years 1329 to 1981 (E/1329/1, E/1566/1, E/1669/1, E/1669/2, E/1886/1, E/1964, E/1981) used in this study were collected by Drs. Frank Spera (University of California, Santa Barbara) and David Graham (Oregon State University). Unpublished whole rock major and trace element and isotopic data for these samples were also made available for use. Additionally, Dr. Marco Viccaro of the Universita di Catania, Italy generously contributed the samples EV/1974/1, EV/2001/1, EV/2004/1 as well as whole rock major and trace element data and $^{87}Sr/^{86}Sr$ for each of these three lava flows.

Petrographic evaluation informed the collection of clinopyroxene geochemical data and the assessment of textures by electron microprobe analysis and back-scattered electron imaging. Such analyses were combined with existing whole rock data (Graham and Spera, unpublished; Viccaro, unpublished) in order to calculate depths of clinopyroxene crystallization based on the geobarometer of Putirka et al. (2003). This then informed the selection of a subset of clinopyroxene that were microsampled for Sr separation and analysis of $^{87}Sr/^{86}Sr$ by thermal ionization mass spectrometry with Dr. Frank Ramos at New Mexico State University.

Petrographic Analysis and Evaluation

A suite of ten samples noted above, representing historic (pre-1971) and recent (post-1971) eruptions dating from 1329-2004, was selected in order to constrain the 1971 alkali-enrichment event and document the evolution of Etna's magmatic system. This

sample suite is the same as that used in the study by Pitcher (2011). Petrographic analysis of thin sections from these individual lava flows was performed using a Nikon LABOPHOT-2 polarized optical microscope at Central Washington University, in order to assess the size, texture and abundance of clinopyroxene within each sample. Corresponding thick sections were then analyzed petrographically, documenting the size, texture, and presence of inclusions and fractures for each clinopyroxene crystal. Each thick section was electronically scanned, and the location of each clinopyroxene was mapped. Utilizing NIS-Elements software, a photographic library was developed in order to document the size and textures of each crystal. Twelve to thirteen clinopyroxene phenocrysts were imaged in each slide. Further characterization of textures relied upon back-scattered electron imaging, in which a high-resolution image of the sample is obtained by scanning an electron beam over the surface of the thick section. All BSE images may be found in Electronic Appendix A. From analysis of the microscope and BSE images, clinopyroxene phenocrysts and microphenocrysts, representing a variety of textures and ranging in size from ~0.75-2.5 mm and ~20-200 μm, respectively, were selected from each sample.

Electron Microprobe Analysis

Electron-microprobe analysis and BSE imaging were performed at the Peter Hooper GeoAnalytical Laboratory, School of the Environment, Washington State University, using the JEOL JXA-8500F field emission electron microprobe (EMP) under the direction of Dr. Scott Boroughs. This microprobe is equipped with five wavelength dispersive X-ray spectrometers, and a Thermo Noran silicon drift energy dispersive X-ray

spectrometer. The EMP offers a non-destructive form of geochemical analysis, in which the sample is bombarded with an electron beam. A field emission source produces electrons that are accelerated down a column that is maintained at high voltage. This electron stream is then condensed and focused by special lenses, producing the beam and allowing for micrometer-scale spatial analysis. Upon bombardment of the sample surface, the electrons excite the sample and interact with its atoms, resulting in the emission of x-ray photons at wavelengths characteristic of the elements present. Comparison of these measurements to a standard of known composition thus produces a high-resolution quantitative major and trace elemental analysis of each programmed spot (Chatterjee, 2012; Goodge, 2012).

In order to ensure the conduction of the beam electrons away from the sample, a carbon coat is required. Residual carbon coats were removed from the thick sections using a steel grinding apparatus and one-micron diamond paste. Each thick section was then given a new carbon coat approximately 200 Ångströms thick by carbon evaporation under vacuum (Boroughs, pers. comm., 2012). Samples were mounted with double-stick conductive carbon tape to further enhance electronic conductivity of the sample surface and loaded into the instrument.

Operating conditions for the microprobe were set at 15 kV accelerating voltage, 30 nA beam current, peak counting times of 20 seconds, 24 seconds (Na_2O) and 40 seconds (MnO), background counting time of 10 seconds, 12 seconds (Na_2O) and 20 seconds (MnO), and 5 μm focused electron beam. The intensity correction applied was an Armstrong-Love/Scott ZAF matrix correction. Used standards included: diopside for

SiO_2, MgO and CaO, augite for TiO_2, Al_2O_3 and Na_2O, hypersthene for FeO and MnO, and hornblende for K_2O (below detection limit in these samples). The analytical resolution for these analyses is 5 microns, and quantitative uncertainty is 1-2% relative, while scanning resolution is on the order of tens of nanometers (Washington State University, 2015). Detection limits for given elements can be found in the Electronic Appendix B, Electron Probe Microanalysis Data.

Twelve to thirteen clinopyroxene crystals, representing a variety of textures and ranging in size from ~0.75-2.5 mm, were analyzed from each thick section, summing to a total of 109 crystals from the ten lava flows. E1974/1 is an aphyric sample for which 12 microphenocrysts were analyzed. A core-to-rim transect was conducted for each crystal, resulting in 2 to 10 EMP analysis spots per clinopyroxene. This produced an *in situ*, quantitative major and trace element characterization of each crystal, documenting the temporal and spatial changes as each crystal grew. Additionally, 6-11 groundmass clinopyroxene were analyzed from each sample, with the largest microphenocrysts analyzed for both core and rim, for a total of 79 additional EMP analyses.

This data set was evaluated by carefully examining element abundances and cation proportions to eliminate those that included mineral inclusions or groundmass. The EMP data set reported in Electronic Appendix B, which excludes such multiphase analyses, was utilized to assess the compositional range of clinopyroxene in these flows and for thermobarometry calculations of all analyzed clinopyroxene.

Geobarometry

Geobarometry calculations were evaluated based on Putirka *et al.* (2003) and Armienti *et al.* (2007, 2012). The geobarometer of Putirka *et al.* (2003) utilizes clinopyroxene-liquid pairs to determine the depths of formation for each crystal as it grows in equilibrium with melt. This depth estimation utilizes temperature- and pressure-sensitive mineral-melt equilibria to determine the pressures at which the individual clinopyroxene or parts of clinopyroxene formed.

The geobarometer utilized in this study relies on the equilibrium constant (K_{eq}) for the jadeite ($NaAlSi_2O_6^{cpx}$) crystallization:

$$NaO_{0.5}^{liq} + AlO_{1.5}^{liq} + 2SiO_2^{liq} = NaAlSi_2O_6^{cpx}$$

Due to the significant difference between the volume (ΔVr) of its products and reactants (23.5 cm^3/mol), this equation is as an excellent determinant of crystallization pressures for the system (Putirka *et al.*, 2003). In addition, due to the entropy change of this reaction being non-zero, the reaction is also temperature dependent (Richet *et al.*, 1993). Acting as a clinopyroxene thermometer, the following equation may be used to determine the K_{eq} of jadeite-diopside (Jd-Di) + hedenbergite (Hd) exchange equilibrium,

$$CaFmSi_2O_6^{cpx} + NaO_{0.5}^{liq} + AlO_{1.5}^{liq} = NaAlSi_2O_6^{cpx} + CaO^{liq} + FmO^{liq}$$

where Fm = FeO + MgO, and $CaFmSi_2O_6$ represents $Ca(Fe,Mg)Si_2O_6$, or DiHd.

These together comprise a thermobarometric calculation for jadeite crystallization and jadeite-diopside + hedenbergite exchange equilibria that will be used to determine the depths of formation for the clinopyroxene:

$$P(\text{kbar}) = -88.3 + 2.82\times10^{-3}T(\text{K})\ln\left[\frac{[\text{Jd}^{\text{cpx}}]}{\left[\text{Na}^{\text{liq}}\text{Al}^{\text{liq}}\left(\text{Si}^{\text{liq}}\right)^2\right]}\right] + 2.19\times10^{-2}T(K) - 25.1\ln[\text{Ca}^{\text{liq}}\text{Si}^{\text{liq}}]$$
$$+7.03[\text{Mg}'^{\text{liq}}] + 12.4\ln[\text{Ca}^{\text{liq}}]$$

$$\frac{10^4}{T(\text{K})} = 4.60 - 4.37\times10^{-1}\ln\left[\frac{[\text{Jd}^{\text{cpx}}\text{Ca}^{\text{liq}}\text{Fm}^{\text{liq}}]}{[\text{DiHd}^{\text{cpx}}\text{Na}^{\text{liq}}\text{Al}^{\text{liq}}]}\right] - 6.54\times10^{-1}\ln[\text{Mg}'^{\text{liq}}] - 3.26\times10^{-1}\ln[\text{Na}^{\text{liq}}]$$
$$- 6.32\times10^{-3}[P(\text{kbar})] - 0.92\ln[\text{Si}^{\text{liq}}] + 2.74\times10^{-1}\ln[\text{Jd}^{\text{cpx}}]$$

The geobarometry equation of Putirka *et al.* (2003) assumes equilibrium between clinopyroxene and melt (liquid) in order accurately calculate the temperature and pressure values, i.e. the clinopyroxene is in geochemical equilibrium with the melt from which it crystallized. In this study, whole rock values were utilized to represent these melt compositions for the pressure calculation. Therefore, each clinopyroxene-whole rock pair was evaluated for equilibrium, which was determined based on Putirka (2008) and Armienti *et al.* (2012), using the following equation:

$$K_D(\text{Fe-Mg})^{\text{cpx/whole rock}} = 0.27 \pm 0.03,$$

where $K_D(\text{Fe-Mg})^{\text{cpx/whole rock}} = (\text{XMgO}^{\text{whole rock}} * \text{XFeO}^{\text{cpx}})/(\text{XMgO}^{\text{cpx}} * \text{XFeO}^{\text{whole rock}})$, and XMgO and XFeO represent the mole fractions of MgO and FeO in the superscripted phase, clinopyroxene (cpx) or whole rock (Armienti *et al.*, 2012). For equilibrium pairs, the value of this coefficient is 0.27 ± 0.03 (Putirka, 2008; Putirka *et al.*, 2003).

The following steps were taken in order to produce a final equilibrium-evaluated clinopyroxene phenocryst and microphenocryst geobarometry dataset for this study:

1. Each individual EMP analysis spot (each point of a core-to-rim transect) was evaluated for equilibrium using its associated whole rock analysis (i.e. a 1329

clinopyroxene analysis was paired with the 1329 whole rock value) from the databases of Graham and Spera (unpublished) and Viccaro (unpublished) using:

$K_D(\text{Fe-Mg})^{\text{cpx/whole rock}} = 0.27 \pm 0.03$,

2a. If $K_D(\text{Fe-Mg})^{\text{cpx/whole rock}} = 0.27 \pm 0.03$ was achieved, these values were accepted as a valid clinopyroxene-whole rock equilibrium pair. These clinopyroxene and corresponding whole rock values were then input into the Putirka *et al.* (2003) geobarometer.

2b. If $K_D(\text{Fe-Mg})^{\text{cpx/whole rock}}$ 0.27 ± 0.03 was not achieved by the individual clinopyroxene-whole rock pair (i.e., values of 0.22 or 0.46), an alternative whole rock value (from the database of Graham and Spera, unpublished; Viccaro, unpublished) was iteratively substituted until K_D of 0.27 ± 0.03 was achieved. This process thus produced a reconstructed clinopyroxene-whole rock equilibrium pair. These clinopyroxene and alternative whole rock values were then input into the Putirka *et al.* (2003) geobarometer.

Once all equilibrium clinopyroxene-whole rock pairs were identified, final geobarometry results using the computation of Putirka *et al.* (2003) provided a range of pressures for all clinopyroxene analysis spots of the phenocrysts and microphenocrysts. These final geobarometry results then informed the selection of a subset of clinopyroxene phenocrysts that represent the full range of compositions, textures and pressures for *in situ* Sr isotope microsampling.

Microdrilling of Clinopyroxene Crystals for Sr Isotope Analysis

In situ microsampling was performed with the semi-automated New Wave Microdrill at WSU, using a carbide scriber point HP dentist drill bit. Two clinopyroxene

from the 1329, 1566, 1669.1, 1669.2 and 1886 pre-1971 lava flows were selected and sampled for core and rim, resulting in a total of 17 samples. For the post-1971 lava flows, 3-4 crystals were selected from each of 1981, 2001.1, and 2004.1 for core and rim sampling, for a total of 22 samples.

Thick sections slides were placed on the microdrill mount and secured with double-sided tape. The slide was next calibrated for thickness, and the associated microscope was focused upon the crystal of interest. The microdrill software was then programmed to dig a ~1000-4000 μm-length trough. The target depth was 100 μm, which typically required four traverses. Care was taken to avoid potential groundmass and melt inclusions (as informed by the BSE images of each crystal). Drilling then proceeded, as 1-2 drops of ultra-pure deionized (DI) water was applied to the drill site and 30 μL of DI water was placed on clean parafilm to prepare for transfer of slurry to a beaker. Once the trough was drilled, the resulting slurry was extracted from the slide surface with a clean pipette tip and placed in a 7 mL Teflon® beaker. Several aliquots of the DI water were added to the drill site in order to ensure that all sample residue was collected. Following each drilling sequence, the drill bit was rinsed four times in separate aliquots of ultra-pure DI water. Because the concentration of Sr in these Etna clinopyroxenes is estimated to be 60-78 ppm of Sr, each microdrilled sample contained ~5-20 ng of that element.

Sr Separation

Sample Digestion

The digestion of samples in preparation for Sr microcolumn liquid chromatography initiated with the drying of the contents of each 7 mL Teflon® beaker in order to evaporate the water used in microdrilling. This was performed using a hot plate at approximately 190 °C. Drying preceded the introduction of 0.5 milliliters (mL) nitric acid (HNO_3) in order to dissolve carbonates, organics, and sulfates, and 0.5 mL of hydrofluoric acid (HF) to each sample beaker in order to dissolve silicates. This acid + sample mixture was incubated overnight on a hot plate at ~190 °C. Next, the beakers were allowed to dry, resulting in a secondary residue. In order to dissolve any fluorite present as a result of the addition of HF, one mL of 6 Normal (N) hydrochloric acid (HCl) was then added, and the samples were again incubated overnight at ~190 °C. At this time, as well, ~6 µg of standard NBS987, a high-purity ^{84}Sr-enriched spike, was added to two samples, 1329 A-C and 1566 D-R. Prior to being carefully loaded onto the microcolumns, the samples were again dried and then dissolved in 0.04 mL (40 µL) of 2.5 N HCl.

Sr Microchemistry

In preparation for loading the samples onto the microcolumns for liquid chromatography, a cation exchange resin was first loaded into clean microcolumns. This resin was then cleaned over a 48-hour period using 2.5-3 N HCl. and then the columns were backwashed. Next, to facilitate accurate chromatography of the samples, upon resettling, any excess resin was removed and 2 ml of 2.5 N HCl in 1 mL aliquots were

subsequently flushed through the columns to eliminate any diluted acid. The sample was then carefully loaded into the neck of the column; during loading it was critical to avoid sample contamination of the reservoir region that makes up the top of the column.

Due to the high-precision required in Sr microanalysis, it was critical to freshly titrate exactly 2.5 N HCl for each round of chemistry and it was imperative to allow each aliquot of acid to completely flow through the microcolumn, before proceeding to the next step. All waste acid was collected in freshly cleaned beakers in order to preserve the ability to collect Lead (Pb) and Rare Earth elements (REE) at a future time. After loading of the sample, a 0.05 ml 2.5 N wash was first added to each column; upon absorption (settling) of this acid into the resin, an additional 0.05 ml of 2.5 N wash was added and settled. This was followed by an additional 0.1 mL wash of 2.5 N HCl, which was permitted to settle and drain, and then an aliquot of 0.85 mL 2.5 N HCl was added. An additional 0.5 mL wash represented the Rb collection benchmark, although Rb was not collected for these samples, and thus, the acid was collected into the waste containers. A 0.2 mL wash then commenced in two increments of 0.1 mL, in preparation for collection of Sr. At this time, waste containers were carefully replaced with clean Teflon® collection beakers, and 0.7 mL of 2.5 N HCl added to the microcolumn was collected. In preparation for loading of the purified Sr for analysis, the samples were finally carefully dried on the edge of the hot plate, at approximately 190 °C.

Thermal Ionization Mass Spectrometry

Sr isotopes were analyzed using a VG Sector 54-30 TIMS at New Mexico State University, under the direction of Dr. Frank Ramos. Purified Sr samples were loaded onto

pre-outgassed cathodean beads with rhenium filaments. Sr microsamples were first dried and re-dissolved with 1-2 μL of 5% HNO_3 and loaded onto this filament along with 1 μL of a tantalum oxide (Ta_2O_3) and phosphoric acid (H_3PO_4) mixture. In order to ensure that samples were fully dried prior to analyses, they were allowed to air-dry for approximately one hour, and a current of ~0.8-1.4 amps was then run through the filament until it emitted a red glow.

A total of nine unknowns and one NBS987 Sr standard were placed in a ten-sample turret and loaded into the TIMS instrument; the chamber was sealed and pumped to vacuum conditions. The filaments were then slowly heated, resulting in the ionization of the atoms of the sample. These positively charged ions were then accelerated from their source by an electric field, and separated into beams based upon their mass-to-charge ratios by an electromagnet. These separated beams were then collected in Faraday cups that convert the beam into an electric current (Mueller and Vervoort, 2012). Each charge was correlated to a specific isotope of Sr, and isotopic ratios were calculated based upon the ratio of one Faraday cup to another. Signal intensities were recorded for each isotope, and a computer produced a final compilation of the data set. Sr samples were analyzed in dynamic mode using 5 Faraday collectors with an ^{88}Sr intensity of ~3.0V. Sr isotopic ratios were normalized to $^{86}Sr/^{88}Sr = 0.1194$, and samples of analyzed NBS987 standards averaged 0.71029 (n=3). Uncertainty on the standard was typically ± 0.00001.

CHAPTER IV

RESULTS

Petrographic descriptions of the 10 samples are presented, including a detailed characterization of the mineral assemblage in each sample. Next, clinopyroxene textural and geochemical data are presented that describe relationships among microphenocrysts and phenocrysts of pre- and post-1971 samples. Calculated clinopyroxene geobarometry, based on the Putirka (2003) geobarometer, is discussed, and pressures of formation are examined in context with corresponding major and trace elements. Finally, *in situ* $^{87}Sr/^{86}Sr$ clinopyroxene data are presented.

Petrographic Analysis

30-micron thin sections and 100-micron thick polished sections were analyzed for each of the 10 samples using a petrographic microscope. Detailed petrographic descriptions, including modal abundances and key textural features, are located in Electronic Appendix C and summarized in Tables 1-4. Mt. Etna samples are porphyritic or seriate trachybasalts with 2-15% glassy to fully crystallized groundmass. Trachytic textures are absent to fairly prevalent in this sample suite, and vesiculation varies from 0.5%-34%. The typical mineral assemblage includes plagioclase, clinopyroxene, olivine and Fe-Ti oxides (e.g., Ti-magnetite) with these same phases occurring in the groundmass. Tables 1 and 2 summarize estimated modal abundances of phenocrysts (>250 mm) and microphenocrysts (<250 mm) in each sample. Vesicle and glass (in volume %) abundances are also provided. A first order observation of these data is that the modal abundances, degree of vesiculation, and degree of crystallinity (i.e., crystals vs.

glass) vary from sample to sample, as discussed below. Typically, samples range from 51% to 96% groundmass and the degree of vesiculation varies from 0.5% to 34%. Pre-1971 samples display a range of 51% to 70% groundmass and 0.5% to 30% vesiculation, while post-1971 samples display a range of 58% to 96% groundmass and 7% to 34% vesiculation. Note that the most recent lava flows in my sample collection (2001.1 and 2004.1) express the highest degree of vesiculation (34%), consistent with documentation of an increase in volatiles post-1971 for the Etna magmatic system (Clocchiatti *et al.*, 1988; Kamenetsky *et al.*, 2007; Métrich *et al.*, 2004).

TABLE 1. PRE-1971 WHOLE ROCK SAMPLE TEXTURES, PETROGRAPHIC CHARACTERISTICS AND MODAL ABUNDANCES

Sample	Rock Texture	Modal % Phenocrysts	Modal % Groundmass*	Modal % Vesicles	Groundmass Crystallinity	Trachytic Texture
1329/1	Porphyritic	30	70	14	Holocrystalline/ Hypidiomorphic	Fairly prevalent
1566/1	Seriate	42	68	22	Hypocrystalline	Slight
1669/1	Porphyritic	39.5	60.5	30	Hypocrystalline	Slight
1669/2	Seriate/ Porphyritic	44.5	55.5	18	Hypocrystalline	Slight
1886/1	Seriate	49	51	0.5	Holocrystalline/ Hypidiomorphic	Slight
1964/1	Seriate	33	67	5	Hypocrystalline	Fairly prevalent

Modal percentages of phenocrysts and groundmass were calculated using the Nikon "NIS-Elements BR 3.0" software, and normalized to 100% on a vesicle-free basis.
*Microphenocrysts (<250 μm) are included in groundmass abundance.

TABLE 2. POST-1971 WHOLE ROCK SAMPLE TEXTURES, PETROGRAPHIC CHARACTERISTICS AND MODAL ABUNDANCES

Sample	Rock Texture	Modal % Phenocrysts	Modal % Groundmass*	Modal % Vesicles	Groundmass Crystallinity	Trachytic Texture
1974/1	Aphanitic	4	96	7	Hyalopilitic	Slight
1981/1	Seriate	37.5	62.5	15	Holocrystalline Hypidiomorphic	None
2001/1	Seriate	42	58	34	Vitrophyric/ Hypocrystalline	None
2004/1	Porphyritic	37	63	34	Hypocrystalline	None

Modal percentages of phenocrysts and groundmass were calculated using the Nikon "NIS-Elements BR 3.0" software, and normalized to 100% on a vesicle-free basis.
*Microphenocrysts (<250 μm) are included in groundmass abundance.

TABLE 3. PRE-1971 PHENOCRYST (>250 µm) AND MICROPHENOCRYST (<250 µm) MINERAL AND GLASS VOLUME PERCENTAGE

Year	1329/1	1566/1	1669/1	1669/2	1886/1	1964/1
Phenocryst						
Plagioclase	25%	36%	25%	34%	29%	28%
Clinopyroxene	1%	2%	7.5%	6.5%	12%	11%
Olivine	1.5%	1.5%	5%	3%	5%	3%
Opaques	2.5%	2.5%	2%	<1%	3%	<1%
Glomerocrysts	Common	Less Common	Very Common	Very Common	Very Common	Very Common
Microphenocryst						
Plagioclase	35%	30%	17%	17.5%	21%	25%
Clinopyroxene	15%	20%	13.5%	11%	17%	15%
Olivine	10%	5%	10%	8%	5%	10%
Opaques	10%	11%	15%	15%	8%	11%
Glass						
	NONE	2%	5%	4%	NONE	6%

Calculated using the Nikon “NIS-Elements BR 3.0” software, and normalized to 100% on a vesicle-free basis. Prevalance of glomerocrysts is also presented.

TABLE 4. POST-1971 PHENOCRYST (>250 µm) AND MICROPHENOCRYST (<250 µm) MINERAL AND GLASS VOLUME PERCENTAGE

Year	1974/1	1981/1	2001/1	2004/1
Phenocryst				
Plagioclase	NONE	20%	26%	18%
Clinopyroxene	2%	13%	14%	15%
Olivine	2%	2%	1%	3%
Opaques	NONE	2.5%	<1%	1%
Glomerocrysts	Less Common	Very Common	Common	Very Common
Microphenocryst				
Plagioclase	26%	25%	20%	15%
Clinopyroxene	32%	20%	13%	19%
Olivine	10%	7%	5%	5%
Opaques	13%	10%	5%	12%
Glass				
	15%	0.5%	15%	12%

Calculated using the Nikon “NIS-Elements BR 3.0” software, and normalized to 100% on a vesicle-free basis. Prevalance of glomerocrysts is also presented.

A notable feature of the Etna samples is the observed decrease in plagioclase abundance and increase in clinopyroxene abundance (Tables 3 and 4, Figures 6 and 7). Although variability in both mineral abundances is observed from sample to sample, these changes yield a distinct decrease in the plagioclase to clinopyroxene modal abundance ratio over time (Figure 7). The most dramatic change (for the samples in this study) occurs between flows 1566 and 1669.1.

Observed groundmass textures range from seriate to porphyritic, with sample 1974/1 displaying hyalopilitic texture (Tables 1 and 2**)**. Groundmass crystallinity typically ranges from holocrystalline/hypidiomorphic to hypocrystalline, except sample 2001/1, which has vitrophyric texture. BSE images of representative samples displaying these groundmass textures are presented Figure 8a-f. Trachytic texture, in which plagioclase phenocrysts and microphenocrysts are aligned due to flow, is variably developed in most samples, except 2001/1 and 2004/1, which lack this feature. Based on these images, there is little textural distinction between pre- and post-1971 samples.

Groundmass color appears to be dependent upon texture, as samples containing abundant glass (1669/2, 1964/1, 2001/1 and 2004/1) display a light tan to dark brown hue, whereas holocrystalline samples are generally light grey to black. All samples contain monomineralic and polymineralic glomerocrysts, the size and abundance of which are different for each sample (see Electronic Appendix C**)**. Polymineralic glomerocrysts typically consist of plagioclase + clinopyroxene ± olivine ± Fe-Ti oxides ± melt inclusions, while dominantly monomineralic glomerocrysts are primarily comprised

of large aggregations of plagioclase or clinopyroxene with inclusions of melt and Fe-Ti oxides.

Tables 5 and 6 describe the phenocryst size ranges for the primary mineral assemblage of plagioclase, clinopyroxene and olivine. Olivine phenocrysts display a range from 0.25 to 2.4 mm in pre-1971 samples and 0.3 to 1.25 mm in post-1971 samples. These phenocrysts are typically euhedral or, subhedral and embayed and are typically present within polymineralic glomerocrysts in both pre- and post-1971 samples. Plagioclase phenocrysts range in size (long axis) from 0.3-5.0 mm in pre-1971 samples, whereas those in post-1971 samples have a smaller range of 0.3-3.0 mm. Several types of zoning textures are observed, including boxy-cellular morphology and complex oscillatory and patchy zoning. Many plagioclase microlites display swallowtail features. Plagioclase phenocrysts in 1974/1, 1981/1, 2001/1, 2001/2, 2004/1 and 2004/2 were thoroughly characterized texturally by Pitcher (2011). His work defines the abundance of textural types within single crystals. He documents variable combinations of monotonous, oscillatory, convolute, sieve and patchy zoning. Swallowtail features and melt inclusions are also identified. Figures 9a-f and 10a-f illustrate the complex range of

TABLE 5. PHENOCRYST SIZE RANGES (IN MM) FOR PRE-1971 SAMPLES

Year	1329/1	1566/1	1669/1	1669/2	1886/1	1964/1
Phenocryst						
Plagioclase	0.3-3.5	0.3-5.0	0.3-3.75	0.3-5.0	0.5-2.5	0.3-4.0
Clinopyroxene	0.3-2.5	0.3-2.5	0.3-4.0	0.375-3.0	0.3-3.0	0.3-2.7
Olivine	0.3-1.25	0.25-0.5	0.3-2.4	0.375-1.25	0.2-1.25	0.3-2.25

TABLE 6. PHENOCRYST SIZE RANGES (IN MM) FOR POST-1971 SAMPLES

Year	1974/1	1981/1	2001/1	2004/1
Phenocryst				
Plagioclase	NONE	0.3-3.0	0.3-1.875	0.5-2.5
Clinopyroxene	0.3-0.75	0.3-1.8	0.3-2.375	0.3-3.2
Olivine	0.3-1.2	0.3-1.25	0.3-0.9	0.35-1.0

textures and features displayed in the clinopyroxene phenocrysts. Crystals are 0.3 to 4.0 mm (pre-1971) and 0.3-2.38 mm (post-1971) in size and are typically euhedral. Clinopyroxene 1669.1 C (Figure 10f) is an exception, as it is anhedral, which may be indicative of resorption. The most common textural zoning characteristics of phenocrystic clinopyroxene include unzoned crystals, oscillatory zoning, sector hourglass zoning, and complex oscillatory zoning. Clinopyroxene is texturally complex, as evidenced by multiple textures present in an individual sample. Detailed analysis indicates that there are no textural differences among clinopyroxene in pre- to post-1971 samples.

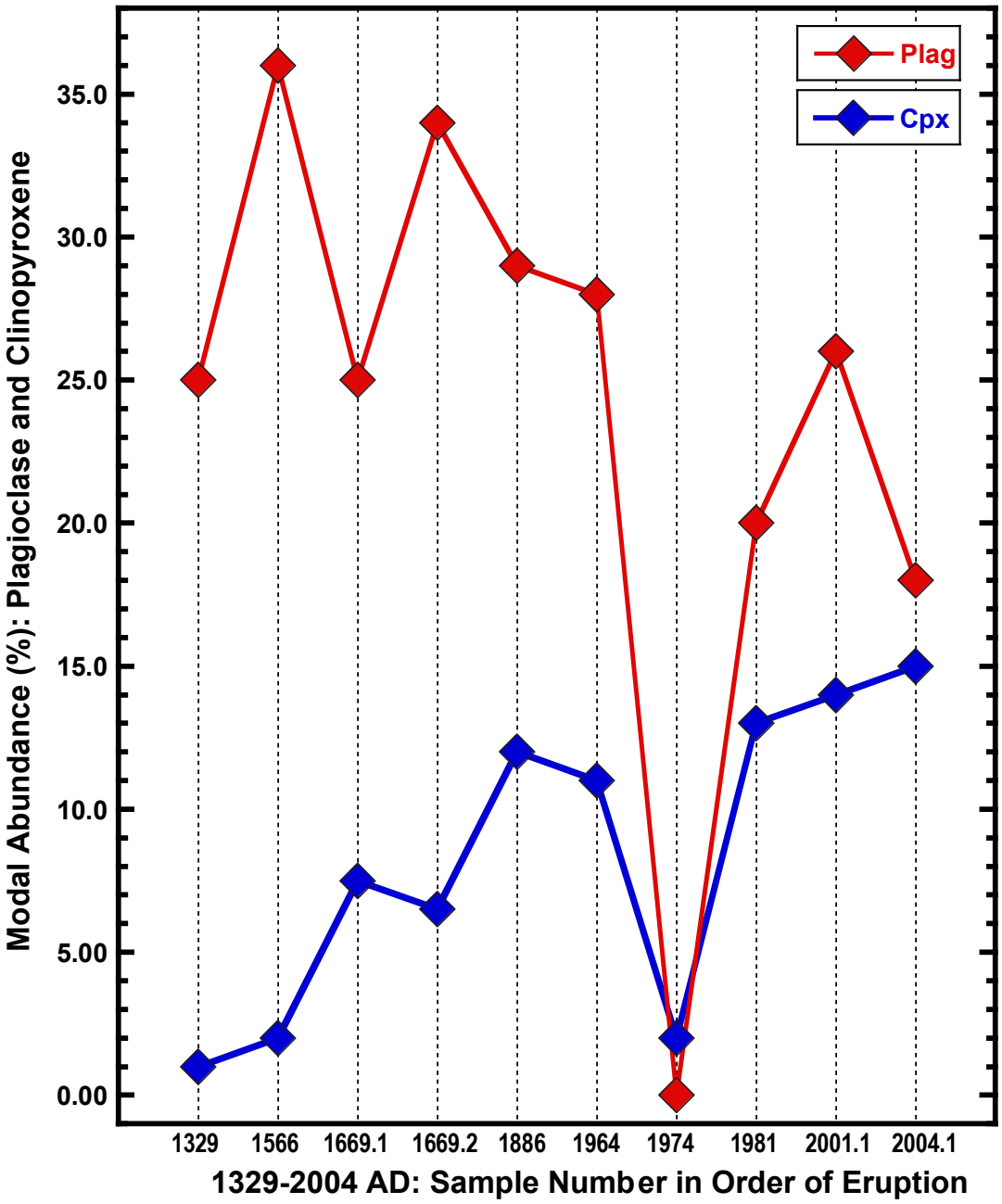

Figure 6. Sample number in order of eruption vs. modal abundance (%): plagioclase and clinopyroxene.

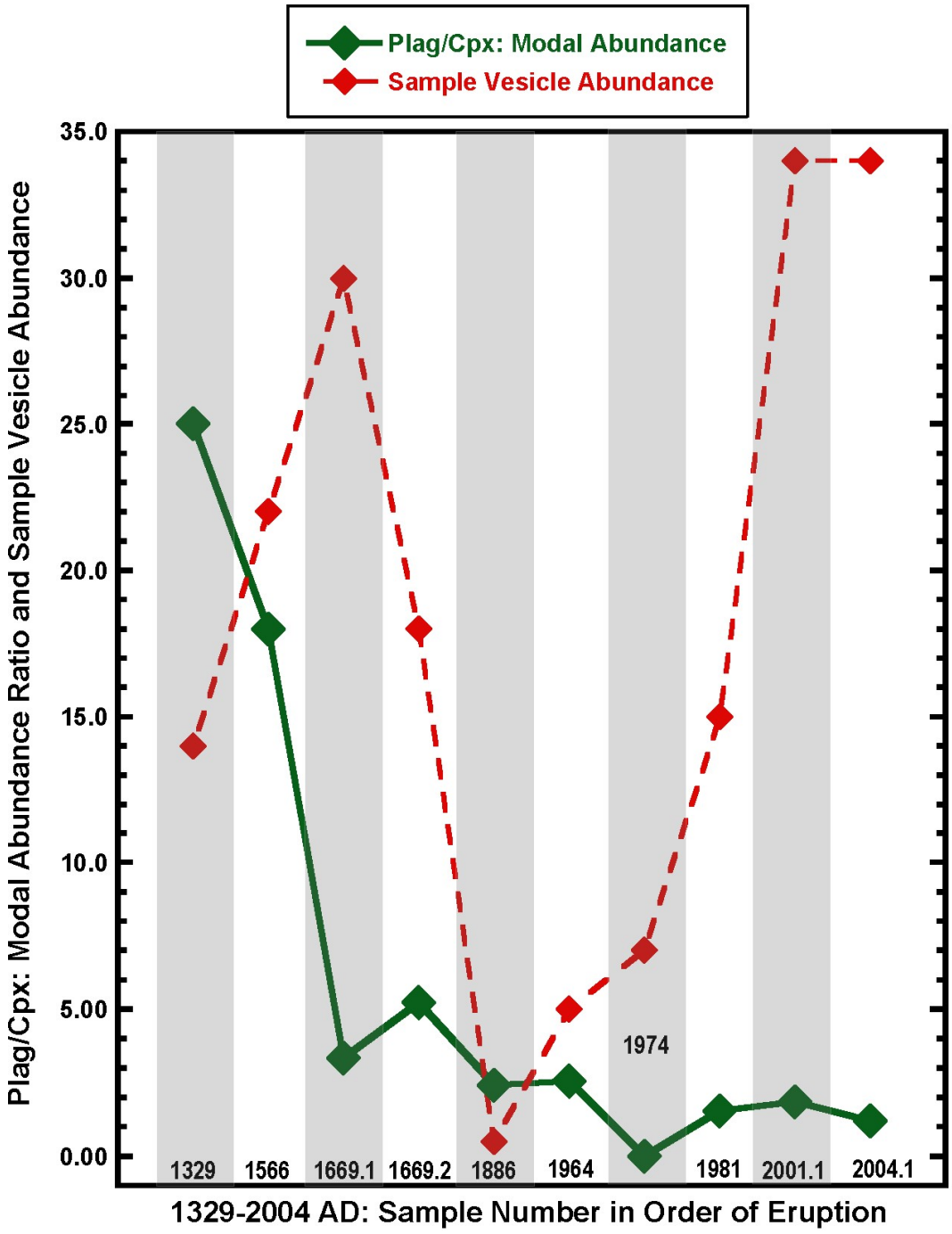

Figure 7. Sample number in order of eruption vs. plagioclase-clinopyroxene modal abundance ratio and total vesicle abundance. Note distinct decrease in plagioclase/clinopyroxene mode ratio from 1329 to 1669 and younger.

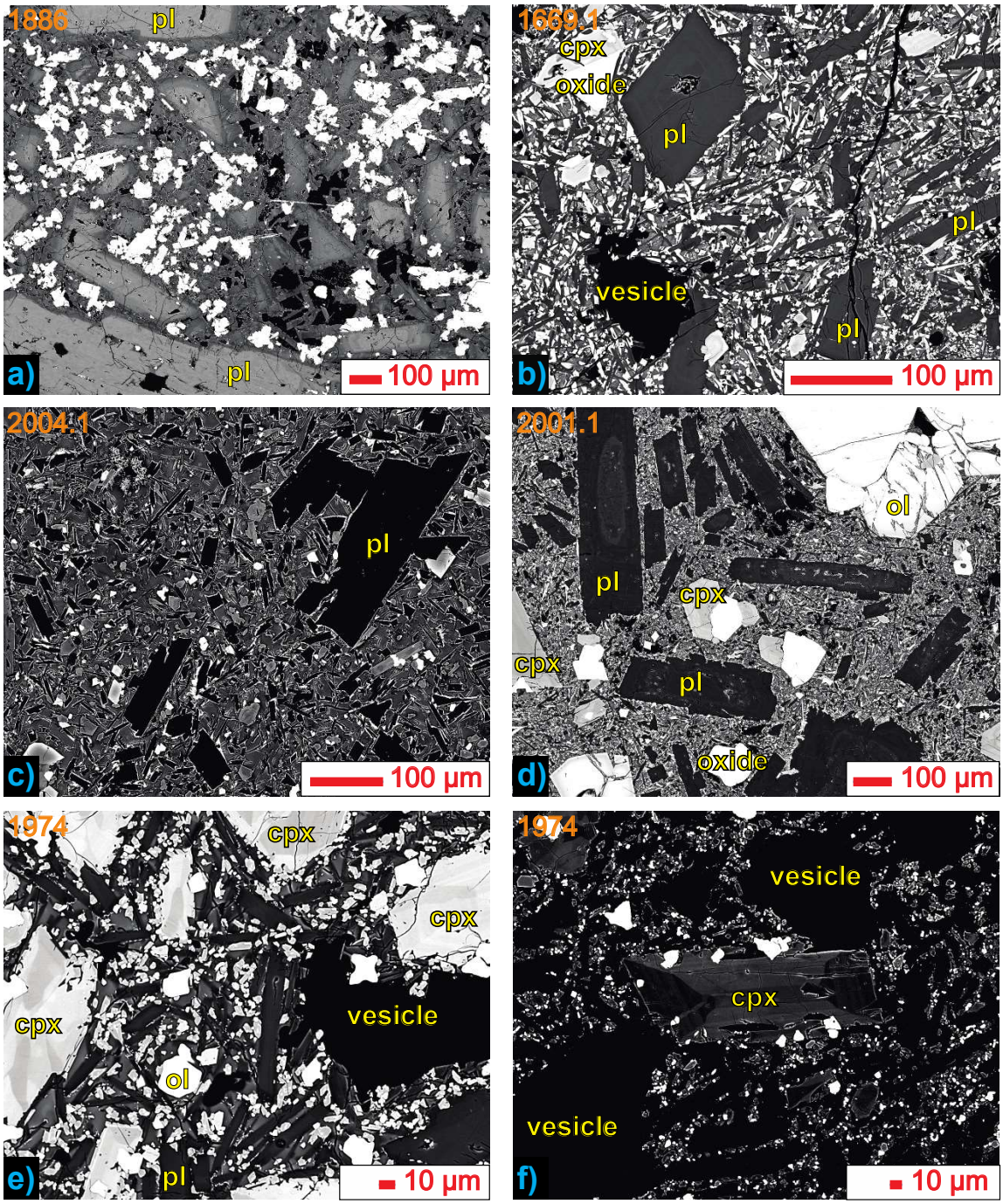

Figure 8a-f. BSE images of groundmass textures displayed in pre-1971 and post-1971 samples: a) 1886 holocrystalline groundmass, b) 1669.1 and c) 2004.1 hypocrystalline groundmass, d) 2001.1 vitrophyric/hypocrystalline groundmass, e) 1974 hyalopilitic texture, f) 1974 hyalopilitic texture with microphenocryst displaying sector hourglass zoning.

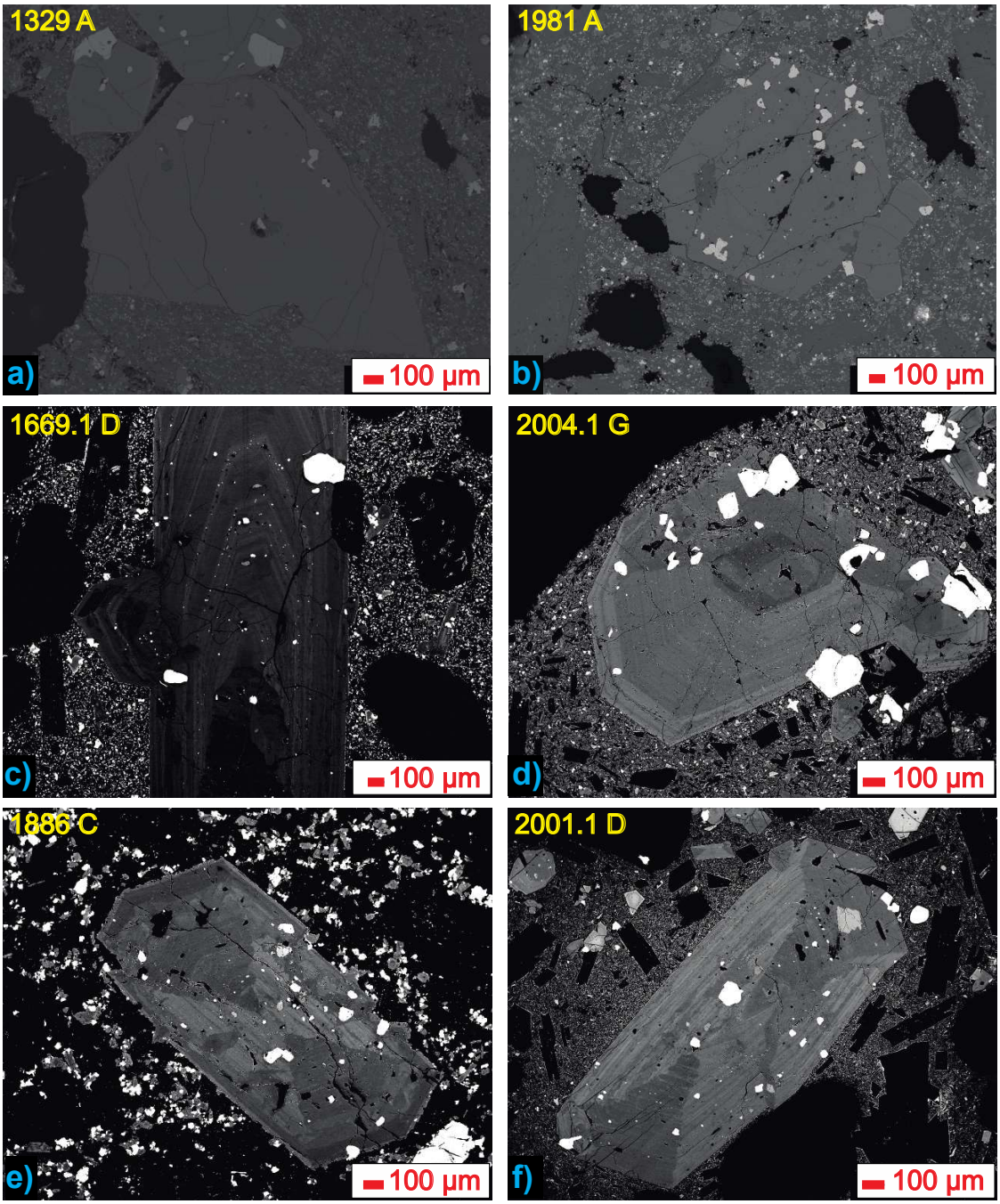

Figure 9a-f. BSE images of clinopyroxene textural features displayed in pre-1971 and post-1971 samples: a) 1329 A and b) 1981 A lack of compositional zoning, c) 1669.1 D and d) 2004.1 G oscillatory zoning, e) 1886 C, f) 2001.1 D sector hourglass zoning.

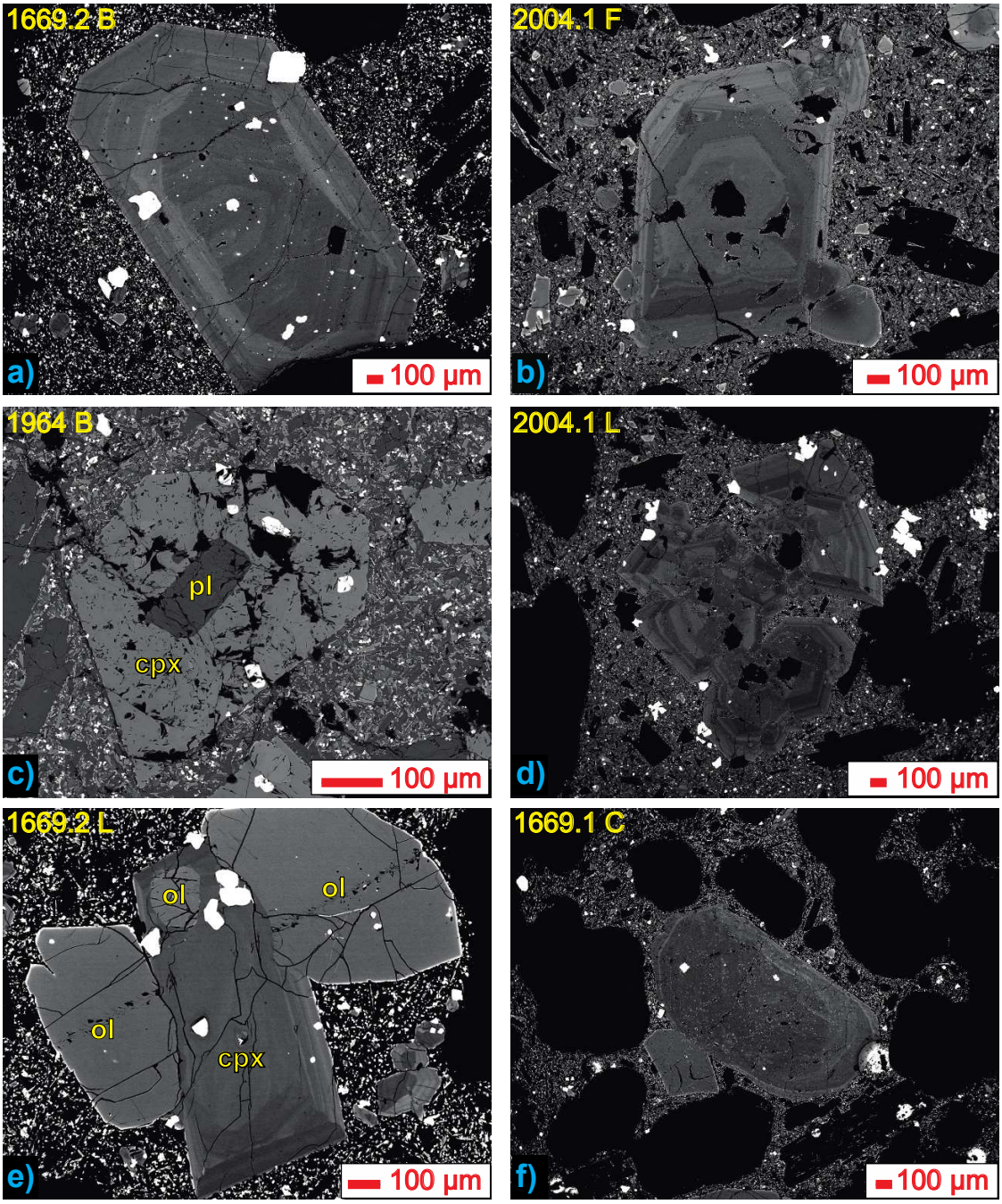

10a-f. BSE images of clinopyroxene textural features displayed in pre-1971 and post-1971 samples: a) 1669.2 B and b) 2004.1 F complex and oscillatory zoning, c) 1964 B cpx with large plagioclase inclusion, d) 2004.1 L monomineralic clinopyroxene glomerocryst, e) 1669.2 L polymineralic clinopyroxene, olivine and Fe-Ti oxide glomerocryst, f) 1669.1 C clinopyroxene displaying resorption feature.

Clinopyroxene Major and Trace Element Data

A total of 109 phenocrysts and 79 microphenocrysts were analyzed via electron microprobe, including 12 microphenocrysts for the mostly aphyric sample 1974/1. Core-to-rim transects were performed for all phenocrysts and typically 3 to 10 spots were analyzed for each crystal. Figure 11 shows an example transect and provides an illustration of the definitions of core, intermediate and rim sections (i.e., analyses) used in this work. Microphenocrysts ~75-200 μm in size were sufficiently large for two analyses: one core and one rim, whereas a single analysis was performed on microphenocrysts less than ~75 μm in size. The following sections outline compositional variations, with particular emphasis on Mg#, defined as (MgO/(MgO+FeO))*100 and weight percent CaO. Electronic Appendix D provides the core-to-rim transects for all phenocrysts, as well as select Mg# geochemical profiles.

En, Fs, and Wo components were calculated on an atomic basis for each analysis in all phenocrysts and microphenocrysts. As displayed in Figure 12, pre- and post-1971 samples are diopside. Compositional zoning is observed in all clinopyroxene, demonstrating minor oscillations in these components. For pre-1971 samples, phenocrysts range from 69.3-79.2 Mg#, and microphenocrysts range from 68.0.-75.3 Mg#. Post-1971 phenocrysts have a range in Mg# from 67.1-81.2 Mg#, whereas microphenocrysts range from 67.3-76.1 Mg#. Overall, there is no clear distinction in En, Fs or Wo between pre- and post-1971 clinopyroxene.

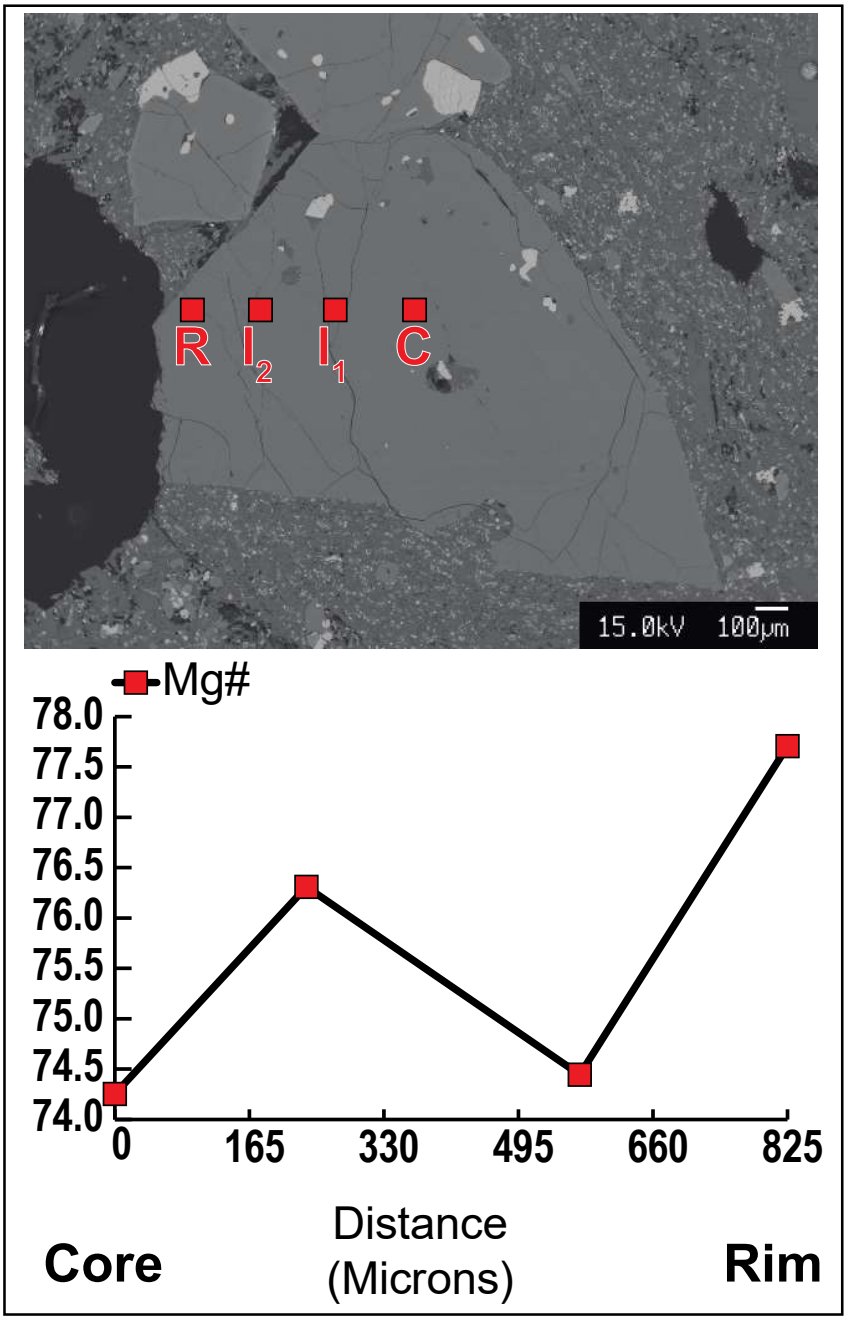

Figure 11. BSE image of Clinopyroxene 1329A, showing an example of a core-to-rim transect, with each electron microprobe analysis represented by a red square. This transect contains one core (C) analysis, two intermediate analyses (I_1 and I_2) and one rim analysis (R). Also shown is a plot of Mg# values along this core to rim transect.

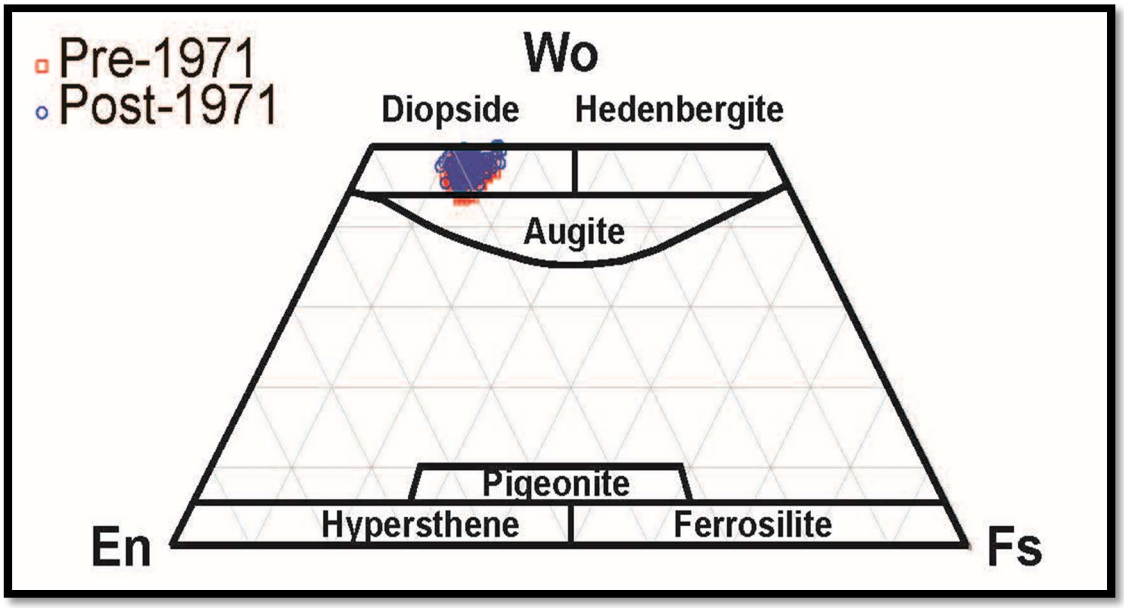

Figure 12. Pre-1971 and post-1971 clinopyroxene is dominantly diopside as shown in this Mg-Fe-Ca pyroxene ternary classification diagram, after Deer *et al.* (1982).

In order to comprehensively illustrate the Mg# range expressed in each sample, Figure 13 presents Mg# values for all analyses of phenocrysts and microphenocrysts for all samples. There is no observed distinction in Mg# between pre- and post-1971 samples, and systematic changes with eruption year are absent as well. Although there is variability in each flow, all phenocrysts share a range of Mg# from ~74.0-77.0 Mg#. The Mg# range for microphenocrysts is typically lower with the maximum at 76.1. All samples contain microphenocrysts with Mg# below 74.0, and microphenocrysts of samples 1669/1, 1669/2, 1974/1 and 1981/1 fall entirely below Mg# 74.0. Sample 1329/1 phenocrysts and microphenocrysts express the most constrained set of values of all samples (70.0-78.0 Mg#), while 2004/1 phenocrysts and microphenocrysts display the most widespread range of values (67.1-81.2 Mg#).

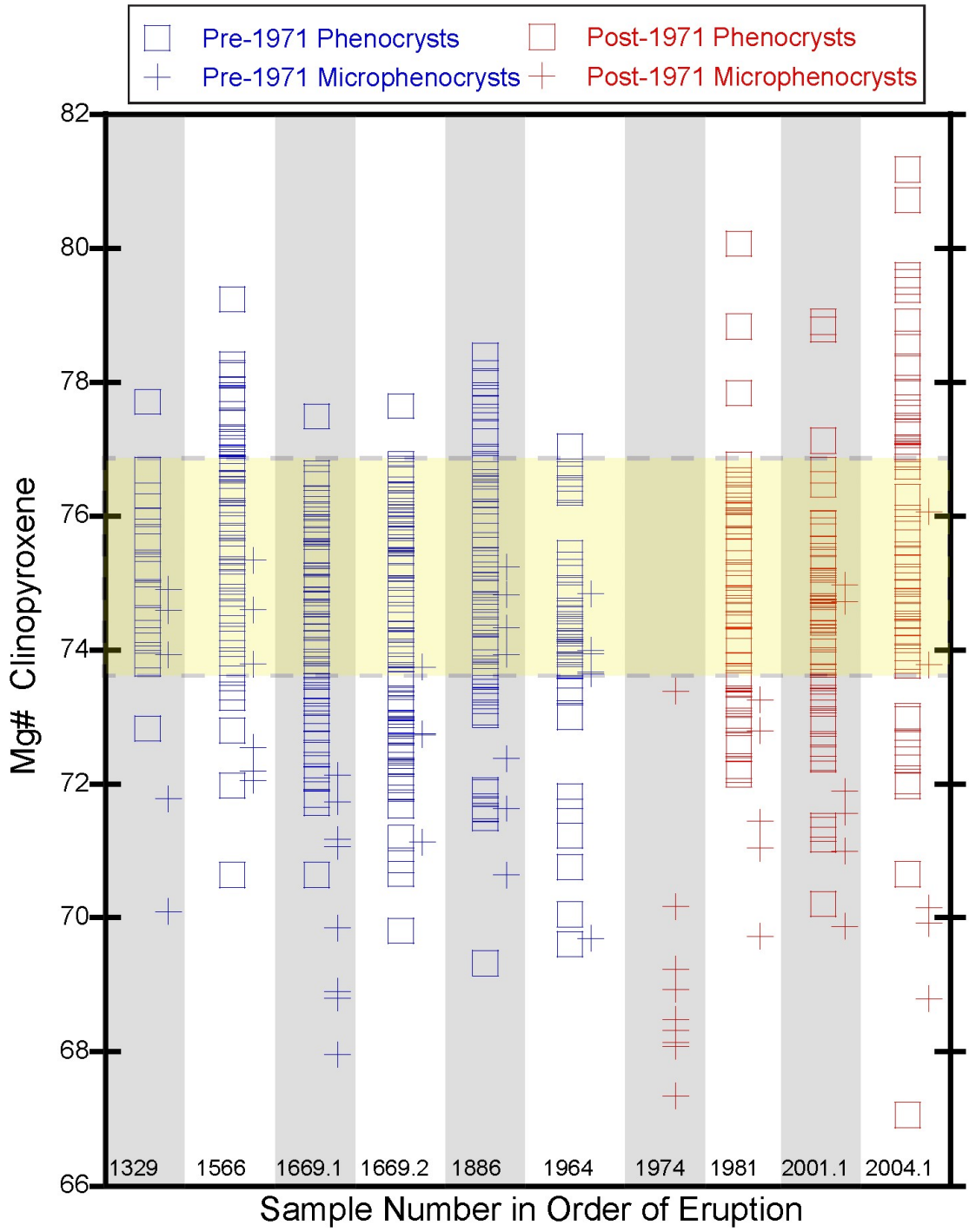

Figure 13. Sample number in order of eruption vs. Mg# clinopyroxene. With the exception of 1974, all samples share Mg# range from 73.8 to 76.7. For definition of Mg#, see text.

Figure 14 shows the mean and standard deviation of Mg# values for all core, intermediate, rim and microphenocryst analyses. A systematic difference between pre-clinopyroxene phenocrysts ranges from 72.9-76.3, whereas pre-1971 microphenocrysts range from 70.2-73.7 Mg#. Post-1971 phenocrysts range from 73.4-76.5, while post-1971 microphenocrysts represent a range of 69.1-72.3 Mg#. The microphenocrysts systematically display the lowest mean values in the samples. All mean core, intermediate and rim values lie within one standard deviation, indicating a lack of major compositional zoning among all samples. The majority of microphenocryst mean Mg# values also lie within one standard deviation of their respective mean core, intermediate and rim Mg# values. The 1669/1 and 1981/1 mean Mg# values are exceptions: the former is distinctly lower than its core, intermediate and rim mean Mg# values, and the latter is distinctly lower than its core mean Mg# value. Figure 15 plots the clinopyroxene Mg# (67.1-81.2) against the whole rock MgO (3.27-7.20 wt. %) values. Despite a broad range of whole rock MgO, there is a great deal of overlap in the Mg# range of clinopyroxene. Thus, there is no correlation between the whole rock MgO and the clinopyroxene Mg# range.

Mg# of pre and post-1971 phenocrysts and microphenocrysts are plotted against major and trace oxides in Figures 16a-h. FeO is, as expected, systematically negatively correlated with Mg#. Scattered negative correlations are also observed in TiO_2 and Al_2O_3, while scattered positive correlations are observed with CaO and SiO_2.

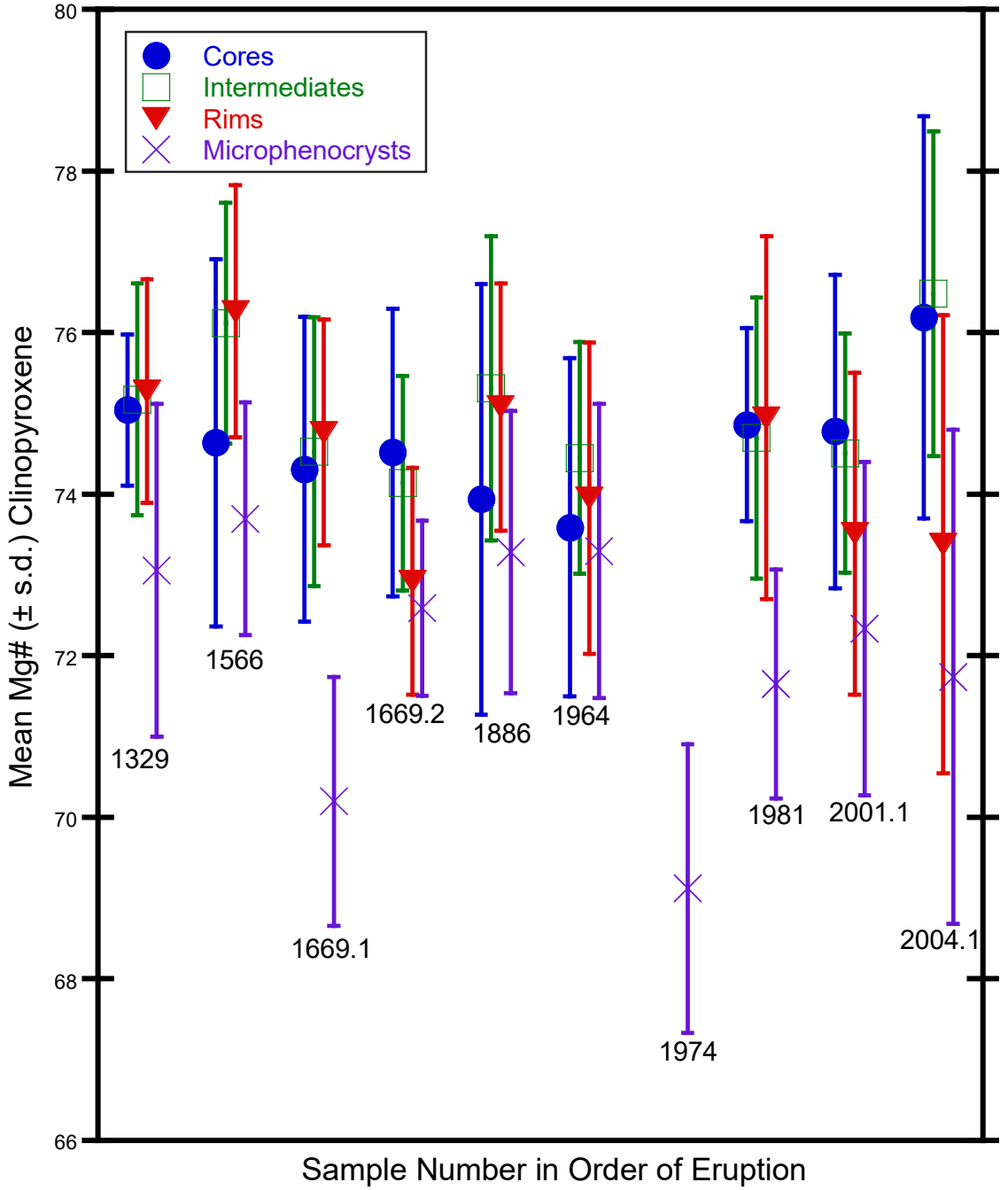

Figure 14. Sample number in order of eruption vs. mean Mg# of cores, intermediates, rims and microphenocrysts. Also shown is one standard deviation for each mean.

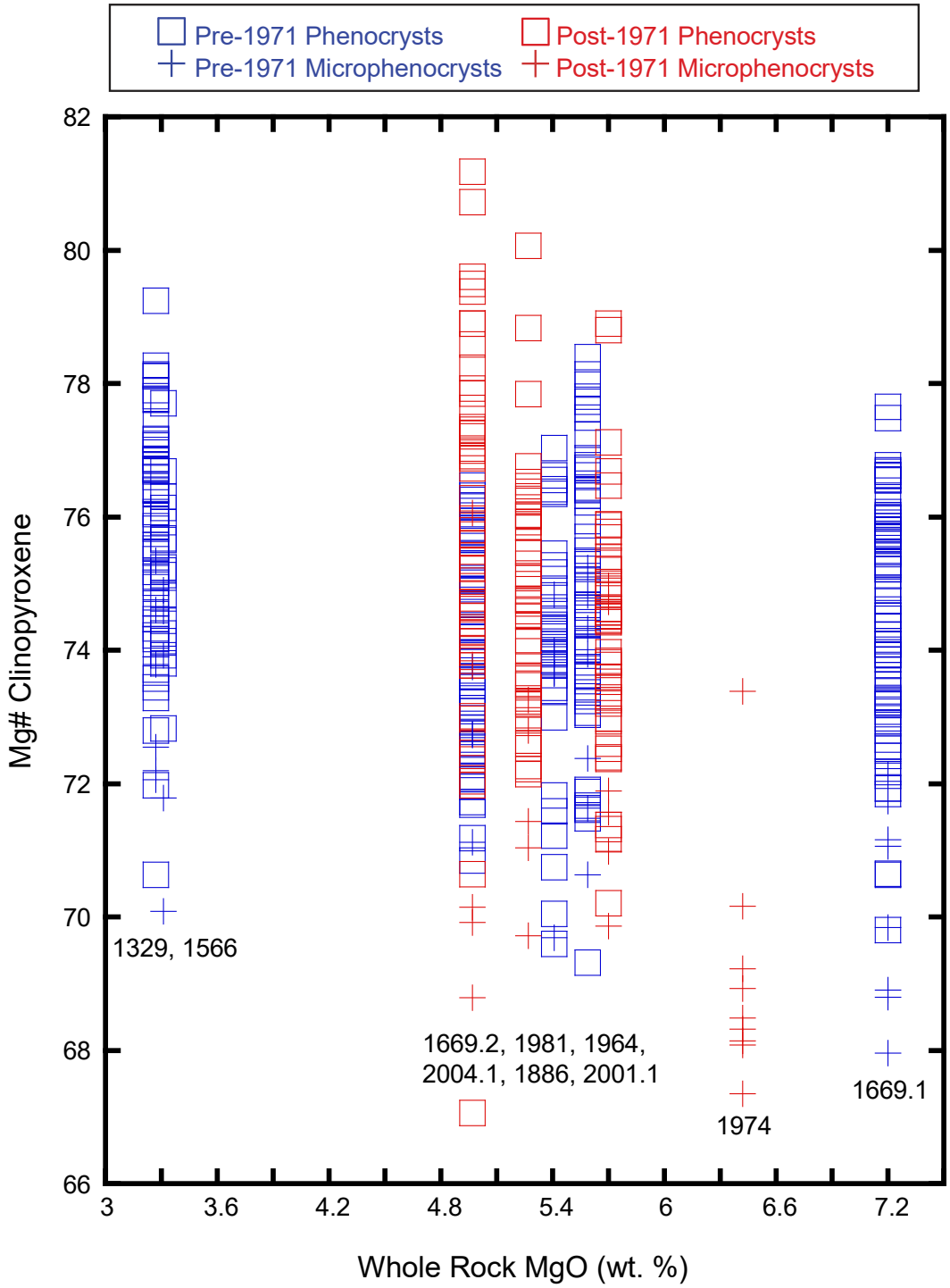

Figure 15. Whole rock MgO (wt. %) vs. Mg# clinopyroxene phenocrysts and microphenocrysts. All colors and symbols are the same as Figure 13.

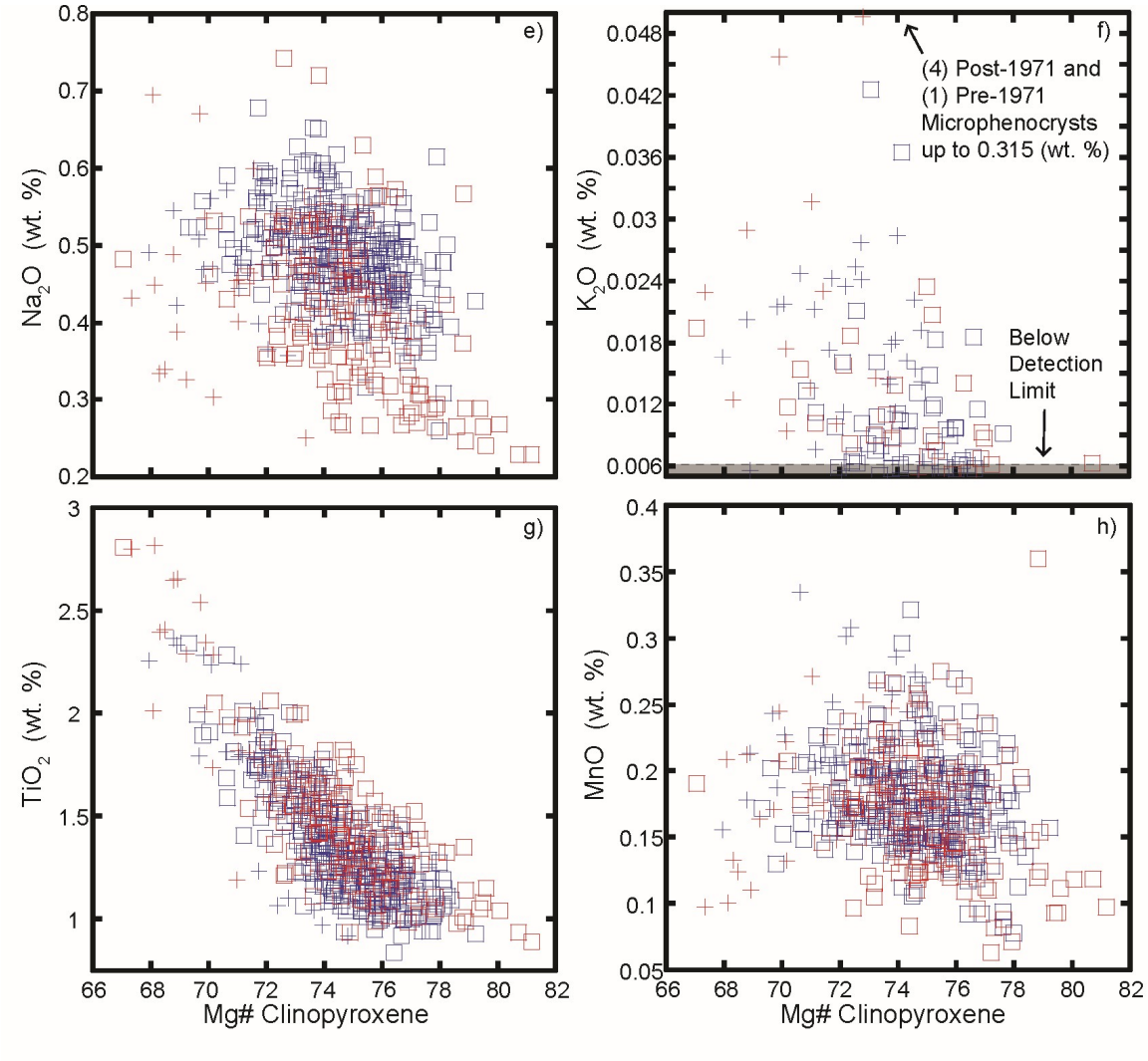

Figure 16a-d. Mg# Clinopyroxene vs. major and trace oxides for pre-1971 and post-1971 phenocrysts and microphenocrysts. All oxides are reported in weight percent. All colors and symbols are the same as Figure 13.

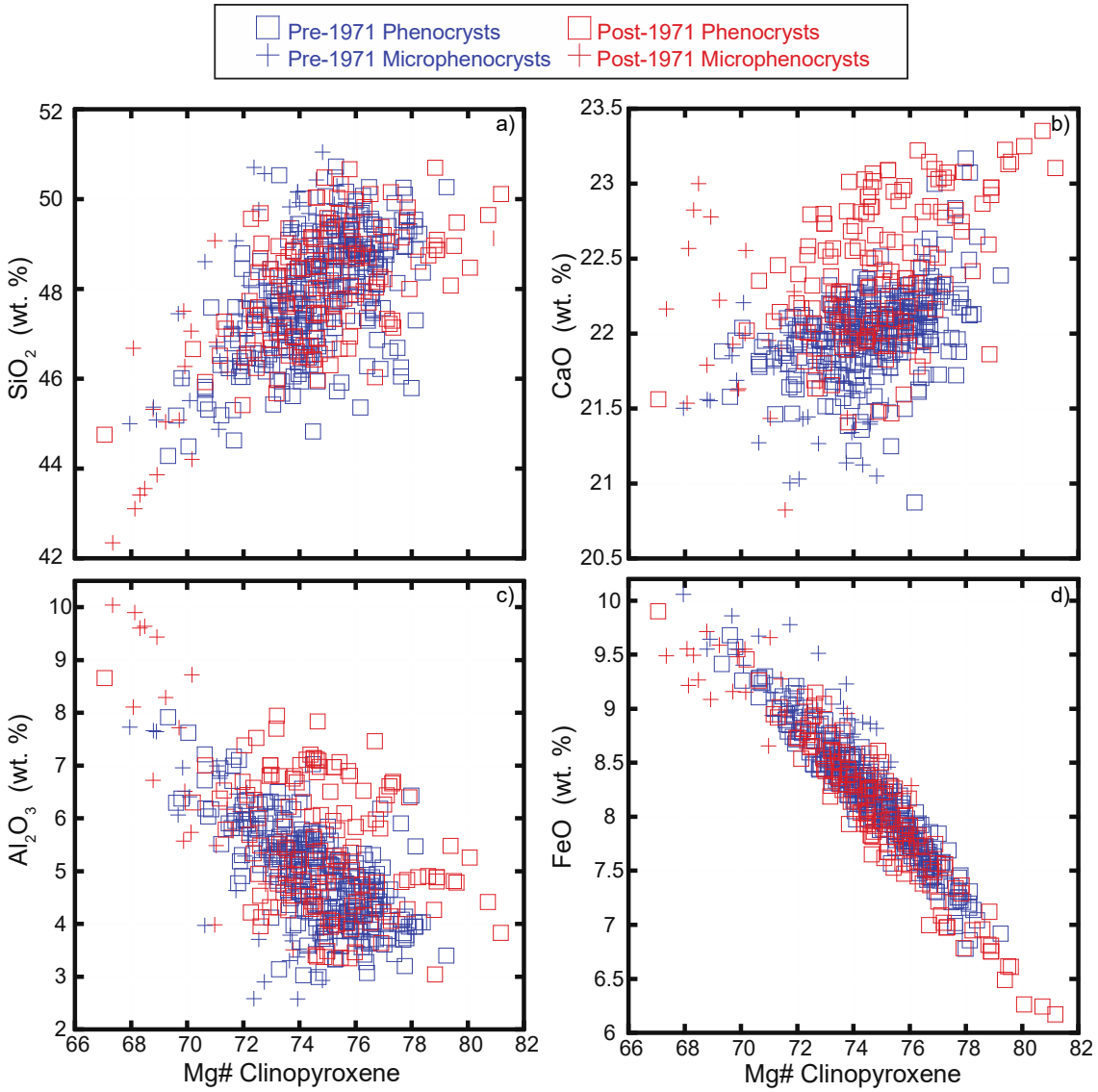

Figure 16e-h. Mg# clinopyroxene vs. major and trace oxides for pre-1971 and post-1971 phenocrysts and microphenocrysts. All oxides are reported in weight percent. All colors and symbols are the same as Figure 13.

Na_2O primarily displays scatter with Mg#, although below 0.3 wt. %, a scattered negative correlation is observed in post-1971 samples. MnO and K_2O (a trace element and often below-detection in clinopyroxene) are not systematically correlated with Mg#.

In terms of pre- vs. post-1971 phenocrysts and microphenocrysts, much overlap is observed, although several microphenocrysts from 1974/1 are characterized by low Mg# values, concurrent with low SiO_2 and Na_2O and high levels of CaO, Al_2O_3 and TiO_2. There exists a population of high-Mg# post-1971 phenocrysts (>78.2) that display elevated CaO and depleted FeO, as well.

Figure 17 represents the range of weight percent CaO in phenocryst and microphenocrysts, and Figure 18 displays the calculated CaO (wt. %) mean and standard deviation for all cores, intermediates, rims and microphenocrysts in each sample. A first-order observation is the elevated CaO values among some 1974/1 microphenocrysts and 1886, 1981, 2001.1, and 2004.1 phenocrysts compared to phenocrysts and microphenocrysts of pre-1971 samples 1329, 1566, 1669.1, 1669.2 and 1964. With the exception of 1886, pre-1971 samples lie systematically below a CaO (wt. %) value of 22.5 (Figures 16a-h and Figure 17) as demonstrated by lower mean CaO (wt. %) values (Figure 18). The samples which contain the high-CaO phenocrysts and microphenocrysts also appear to have more compositionally diverse clinopyroxene populations, compared to the generally smaller standard deviations for phenocrysts and microphenocrysts of samples 1329, 1566, 1669.1, 1669.2 and 1964.

Overlap in core, intermediate, rim and microphenocrysts CaO mean and standard deviation values (Figure 18) is seen in samples 1329, 1669.2, 1964 and 2001.1, while the remaining samples show a higher degree of variance. For samples 1329, 1669.2 and 1964, microphenocrysts lie completely within the field for their corresponding phenocrysts. In contrast, microphenocrysts in samples 1669.1 and 1981 express overlap

with phenocryst intermediates and rims, but lie outside the range of the phenocryst cores, while samples 1566, 1886 and 2004.1 display no overlap with their corresponding phenocryst cores, intermediates and rims.

Figure 19 examines the relationship among CaO phenocrysts and microphenocrysts with their whole rock MgO (wt. %). Pre-1971 samples, with the exception of 1886, are constrained to lower levels of CaO, between 20.8-22.5 weight percent (also seen in Figure 17), despite a wide range of MgO whole rock values (3.31-7.20 wt. %). Samples 1886, 1981, 2001.1 2004.1 (phenocrysts), and 1974 (microphenocrysts) have a more-constrained range of whole rock MgO values from 4.97-6.42 (wt. %) and have the highest and overall widest range of clinopyroxene CaO contents, with maximum values up to 23.4 wt. %.

To further examine these high CaO clinopyroxene, CaO was plotted against a series of oxides (Figures 20a-h). The high CaO group is apparent in all of these diagrams; all phenocrysts within the field greater than 22.5 wt. % CaO are from the 1886, 1981, 2001.1 and 2004.1 samples, and all microphenocrysts within this field are from sample 1974. In addition to elevated CaO, this group of phenocrysts includes a population that is enriched in Mg#, and depleted in FeO, Na_2O and MnO. No distinction is observed in the

Figure 17. Sample number in order of eruption vs. clinopyroxene CaO (wt. %). Sample 1886 and post-1971 samples include a range greater than 22.5, while all other pre-1971 samples lie systematically below this value.

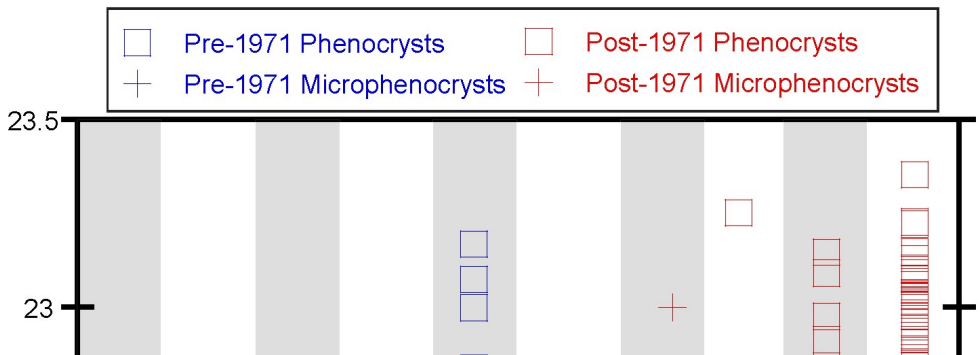

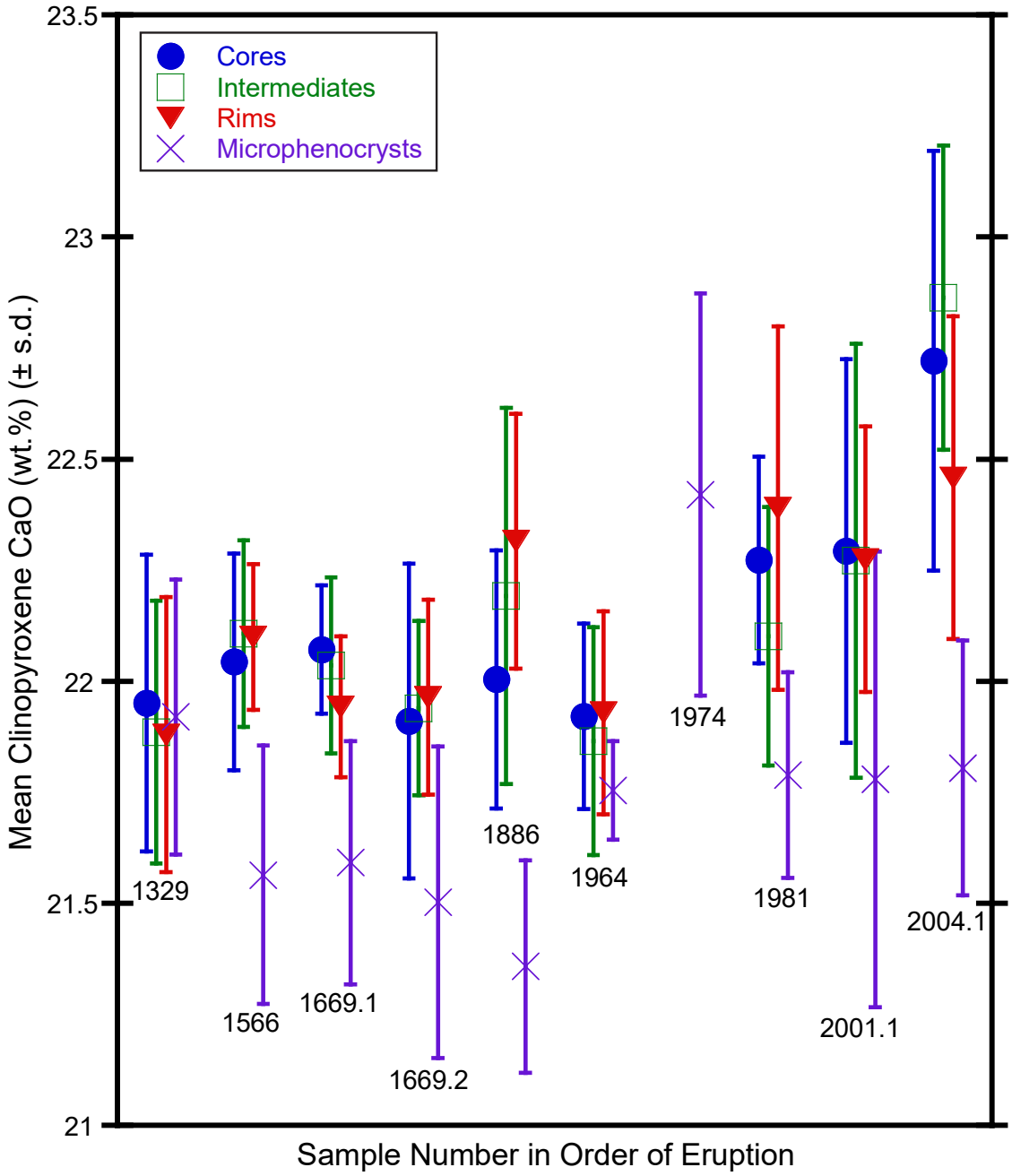

Figure 18. Sample number in order of eruption vs. mean clinopyroxene CaO (wt.%) of cores, intermediates, rims and microphenocrysts. Also shown is one standard deviation for each mean.

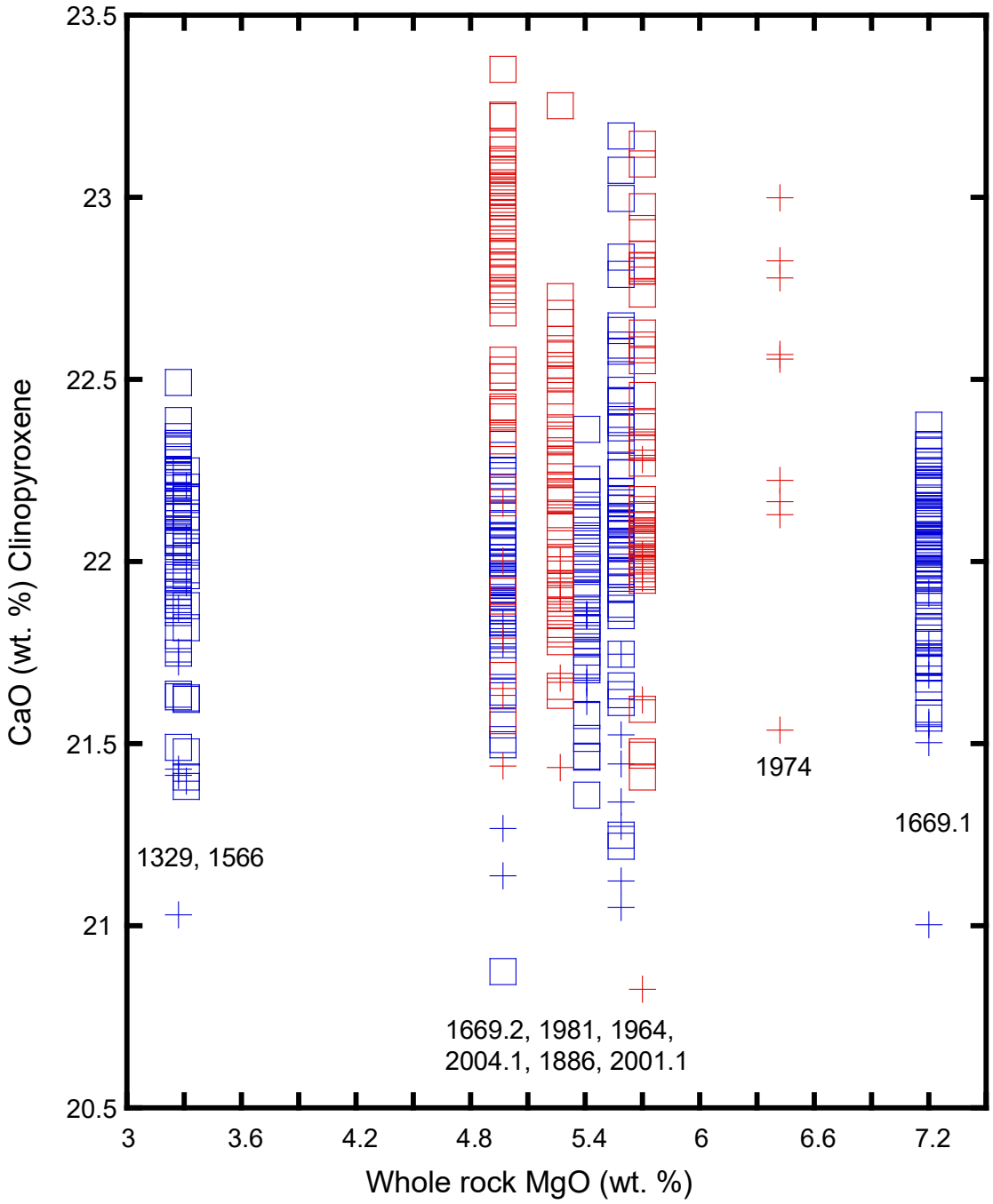

Figure 19. Whole rock MgO (wt. %) for samples 1329-2004.1 vs. CaO (wt. %) clinopyroxene: phenocrysts and microphenocrysts. All colors and symbols are the same as Figure 13.

SiO_2, Al_2O_3, K_2O and TiO_2 components among these high-CaO phenocrysts and the pre-1971 phenocrysts and microphenocrysts. Compared to post-1971 phenocrysts, in combination with elevated CaO, the 1974 microphenocrysts are particularly low in Mg# and SiO_2, and have higher TiO_2, FeO and Al_2O_3.

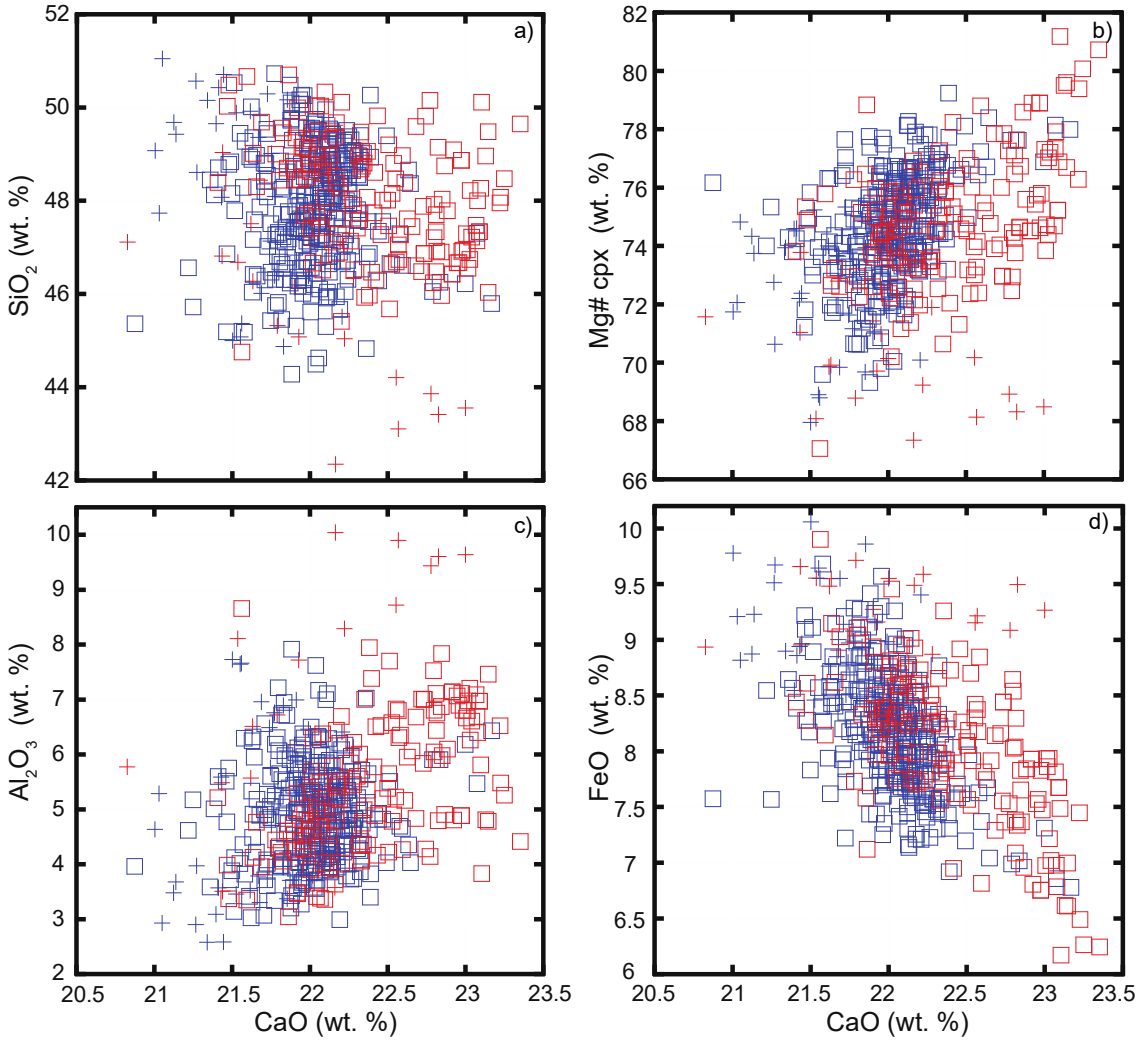

Figure 20a-d. Clinopyroxene CaO (wt. %) vs. major and trace oxides for pre-1971 and post-1971 phenocrysts and microphenocrysts. All oxides are reported in weight percent. All colors and symbols are the same as Figure 13.

Figure 20e-h. Clinopyroxene CaO (wt. %) vs. major and trace oxides for pre-1971 and post-1971 phenocrysts and microphenocrysts. All oxides are reported in weight percent. All colors and symbols are the same as Figure 13.

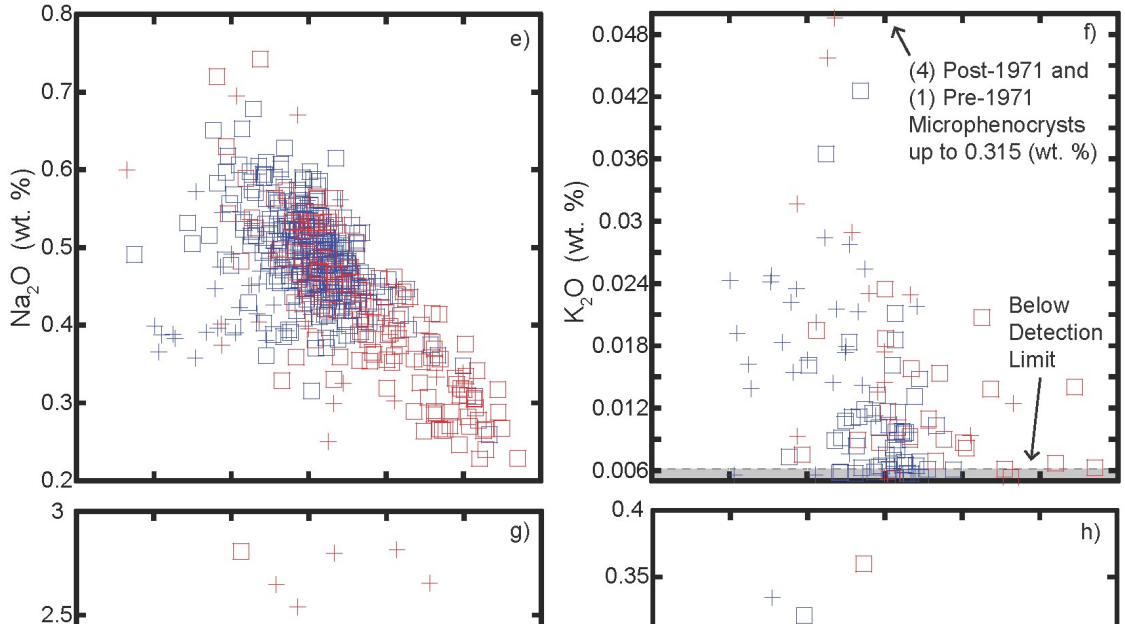

Clinopyroxene Geobarometry

The range of clinopyroxene pressures is 0-7 ± 2 kbar (Putirka *et al.*, 2003) (approximate depths are surface-21 km ± 6 km). These depths of crystallization, as expected based on Armienti *et al.* (2012), vary from deep to shallow within the Etnean plumbing structure, representing a crystallization array from the Moho (~27 km) to the upper crust (<6 km) (Figure 21). No systematic patterns are observed in terms of core, intermediate, rim, and microphenocryst and pressure. Figure 22 presents the eruption year vs. mean pressure for phenocryst cores, intermediates, rims, and microphenocrysts. A dominant range of pressure values is observed at ~2.9-5.5 kbar (~8.7-16.5 km) based on the average values presented in Figure 22. All components overlap in their mean and standard deviation pressure values and there are no clear systematics in terms of pre-1971 versus post-1971 samples.

Figures 23a-f present major and trace elements oxides plotted against pressure, while Figure 24 presents Mg# of the clinopyroxene plotted against pressure. Notably, Figure 23b (enlarged in Figure 25**)** shows an assemblage of post-1971 phenocrysts and 1974 microphenocrysts as well as 1886 phenocrysts (>22.5 wt. % CaO), which (based on calculated pressure values) systematically increase in CaO weight percent with decreasing pressure (~2-5 kbar). Figure 23e (Na_2O wt. % vs. pressure) appears to mirror this relationship: whereas a subset of phenocrysts and microphenocrysts is constrained to ranges of 0.4-0.6 wt. % Na_2O with decreasing pressure, some phenocrysts of the high-CaO population systematically decrease in Na_2O with decreasing pressure. This distinct

population of high-CaO 1886 and post-1971 phenocrysts demonstrate calculated pressures of ~2-4 ± 2 kbar, elevated Mg# and Al_2O_3 and a depletion FeO, Na_2O and MnO values.

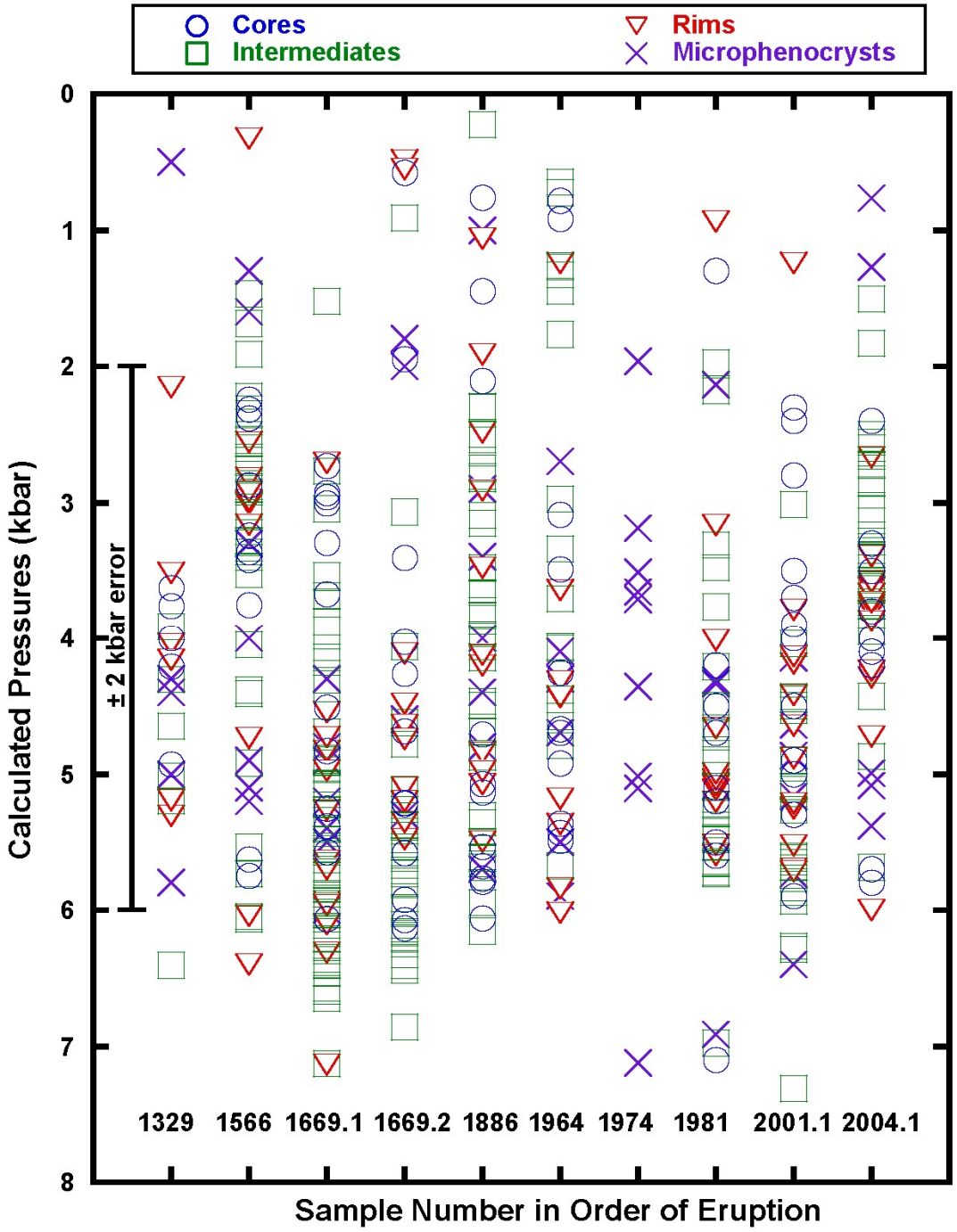

Figure 21. Sample number in order of eruption vs. pressure (kbar) for clinopyroxene phenocryst cores, intermediates, rims and microphenocrysts calculated using Putirka *et al.* (2003).

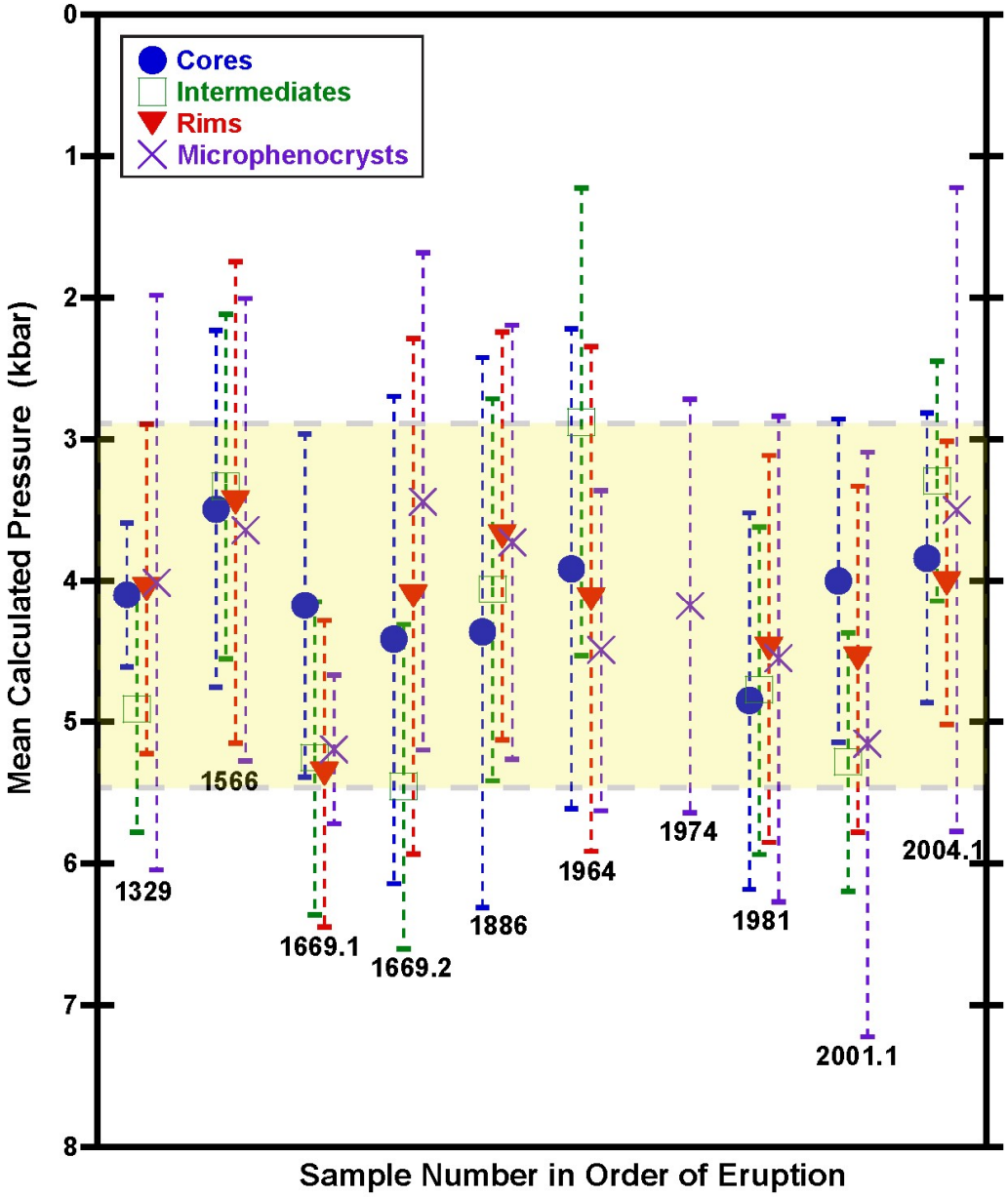

Figure 22. Sample number in order of eruption vs. mean pressures (kbar) for cores, intermediates, rims and microphenocrysts. One standard deviation for each mean is represented by dashed lines. Pressure errors are ± 2 kbar. Yellow region represents a dominant mean pressure range of 2.9-5.5 kbar.

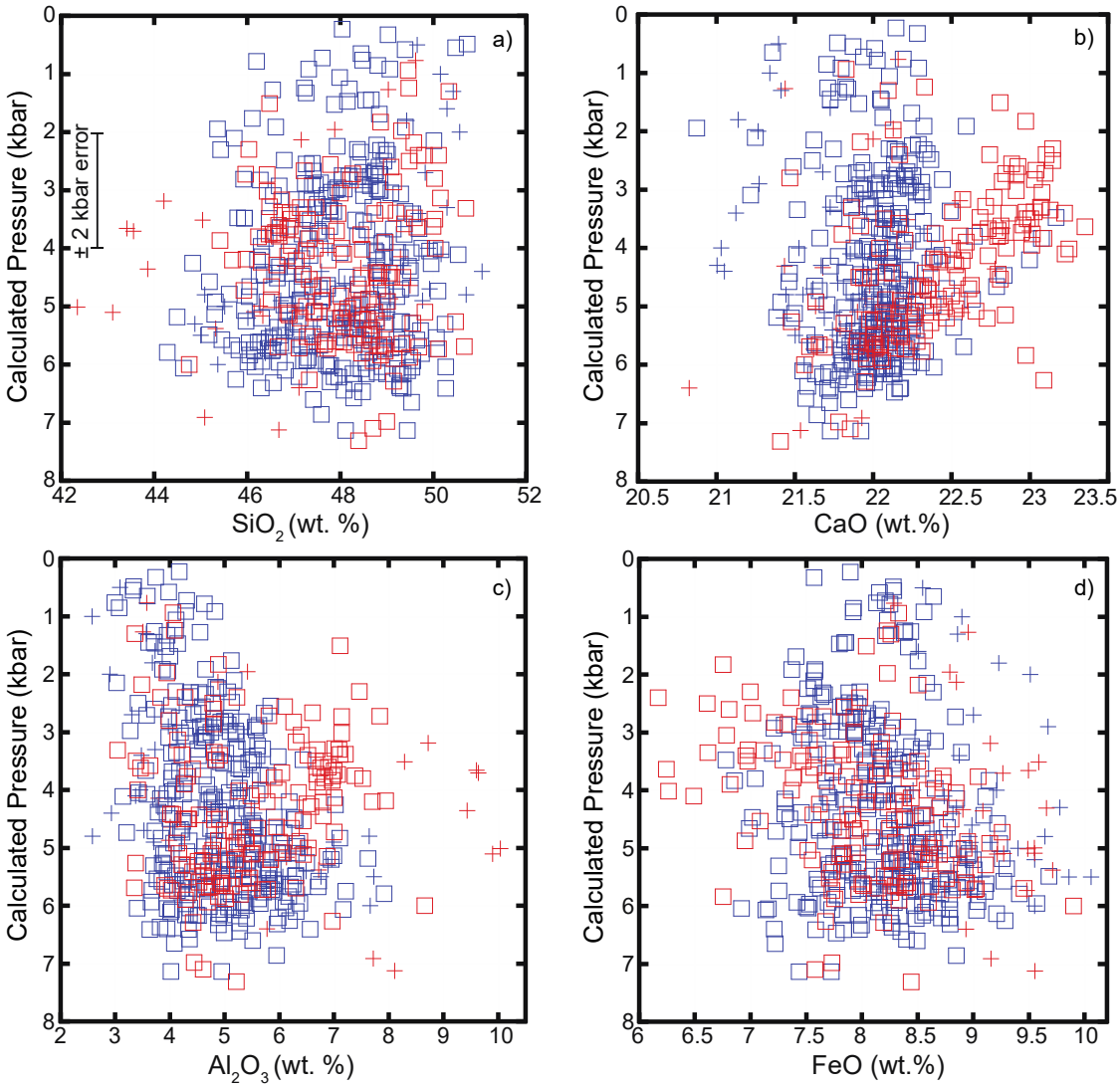

Figure 23a-d. Clinopyroxene major and trace oxides vs. calculated pressure (kbar) phenocrysts and microphenocrysts. All oxides are reported in weight percent. Pressure errors are ± 2 kbar. All colors and symbols are the same as Figure 13

In particular, a subset of microphenocrysts which are greater than 22.5 (wt. %) CaO (n = 5) displays geochemical distinctions that may also be observed in Figures 16a-h and 20a-h. These crystals demonstrate an enrichment or depletion in several components at calculated pressures ~3-5 ± 2 kbar. These microphenocrysts are enriched in CaO, and

tend to increase in CaO with decreasing pressures. They are also depleted in Mg# and SiO_2, and yet generally increase in these components with decreasing pressure. Conversely, the crystals have higher TiO_2, FeO and Al_2O_3 than other phenocrysts and microphenocrysts; yet decrease in these constituents with decreasing pressure.

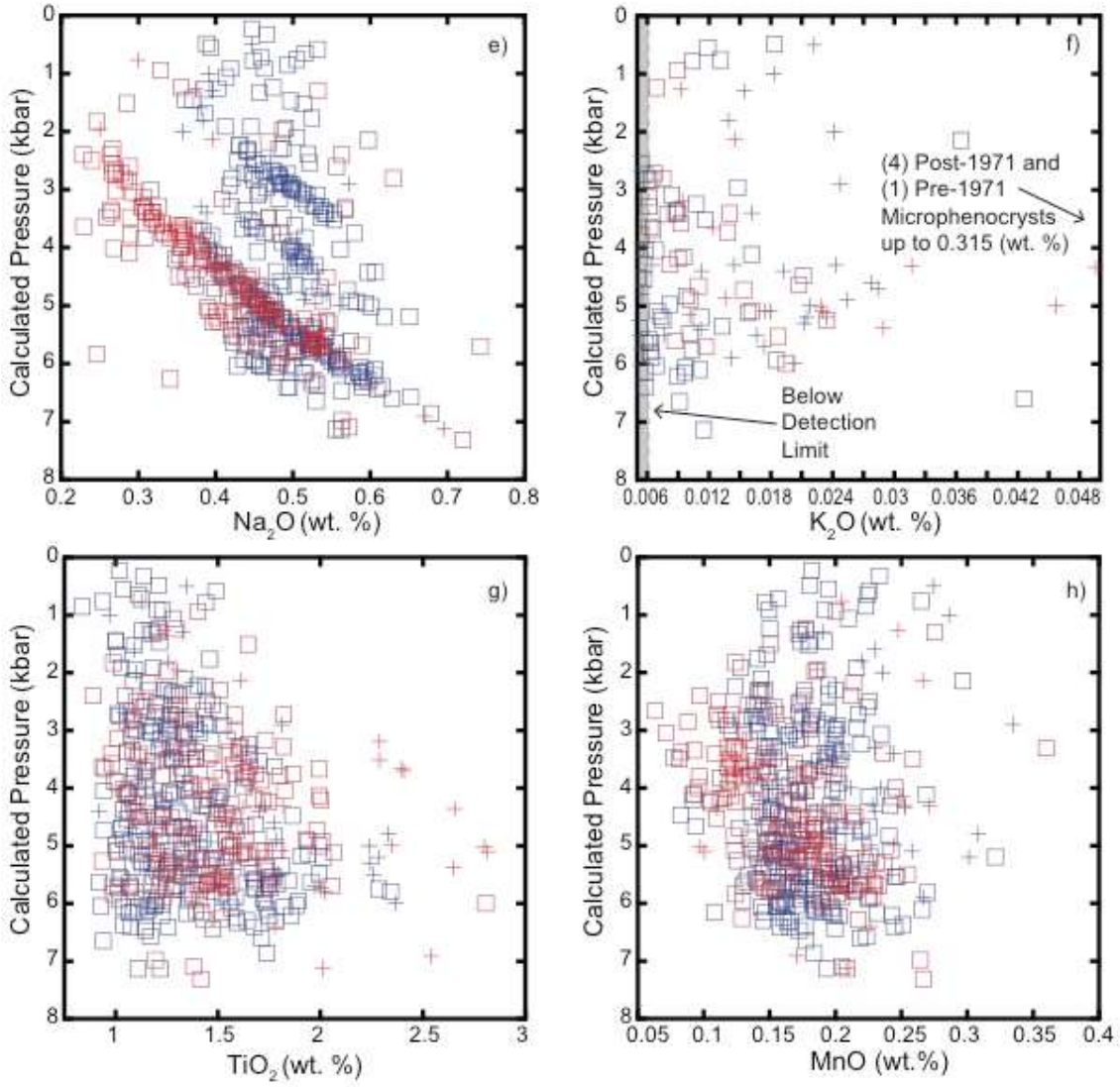

Figure 23e-h. Clinopyroxene major and trace oxides vs. calculated pressure (kbar) phenocrysts and microphenocrysts. All oxides are reported in weight percent. Pressure errors are ± 2 kbar. All colors and symbols are the same as Figure 13.

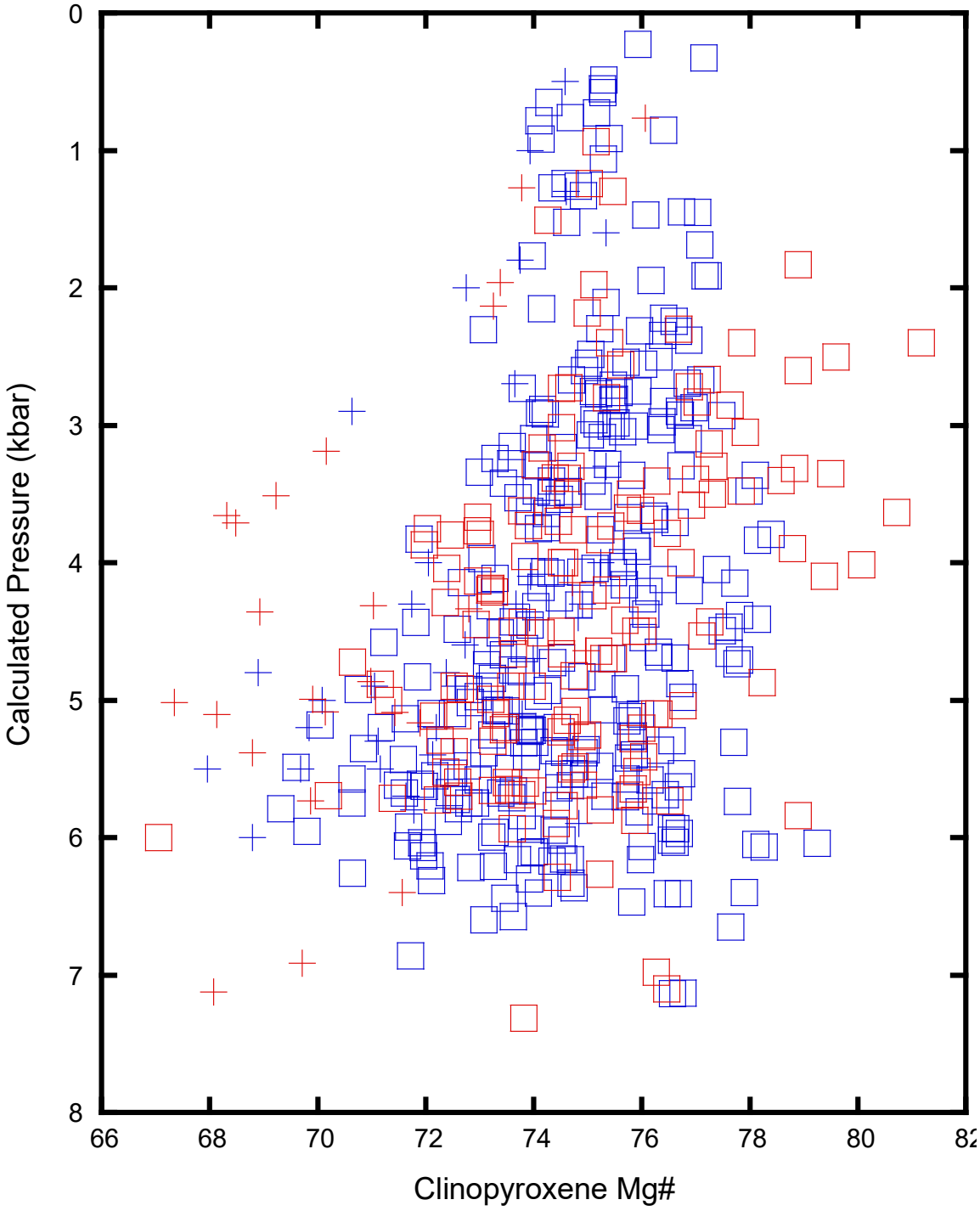

Figure 24. Clinopyroxene Mg# vs. calculated pressure (kbar) for phenocrysts and microphenocrysts. Pressure errors are ± 2 kbar. All colors and symbols are the same as Figure 13.

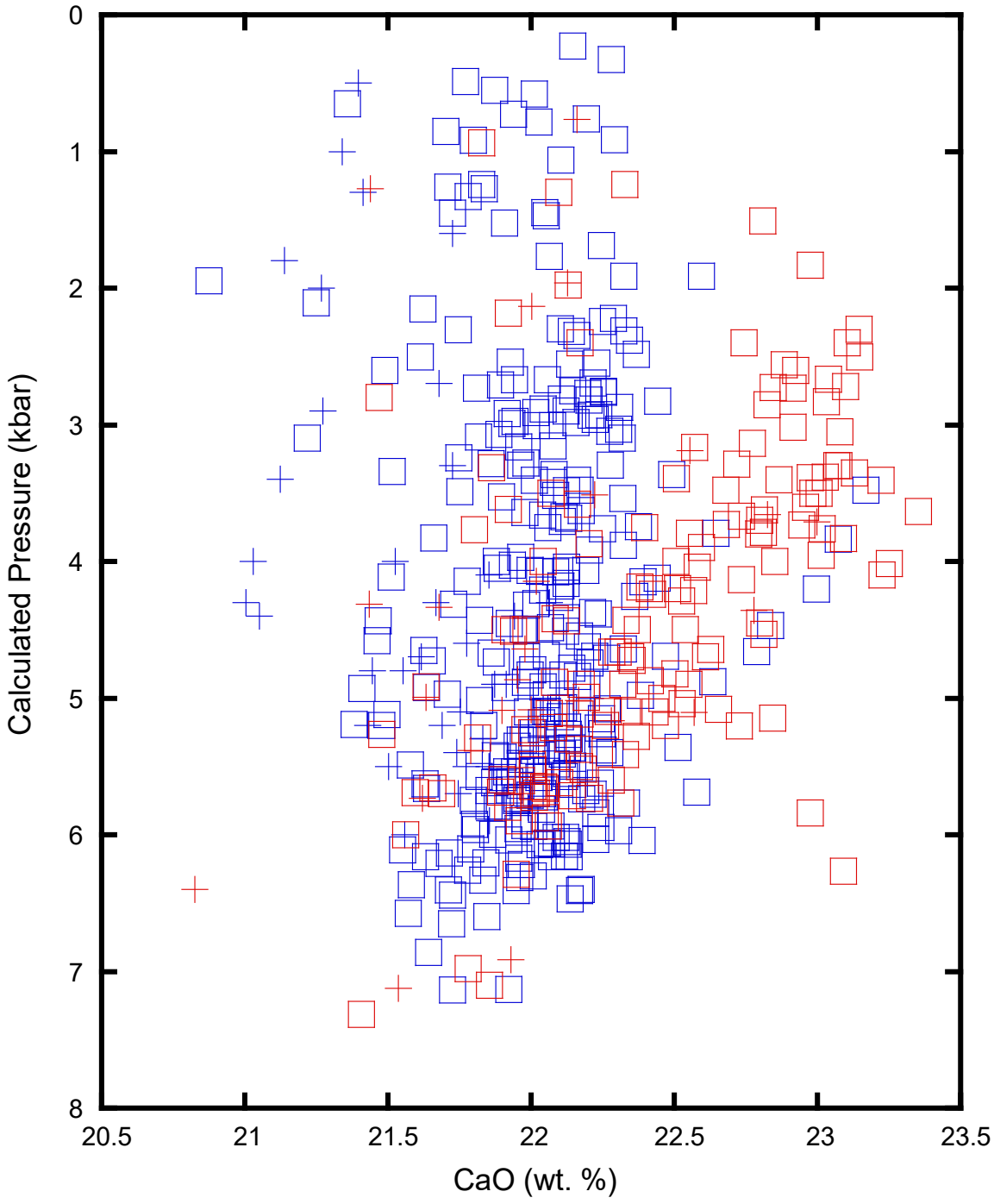

Figure 25. Clinopyroxene CaO (wt. %) vs. pressure (kbar) for pre-1971 and post-1971 phenocrysts and microphenocrysts

Clinopyroxene *In Situ* Sr Isotope Data

The following sections examine the *in situ* Sr isotope core and rim data from pre- and post-1971 samples in the context of eruption year, whole rock $^{87}Sr/^{86}Sr$, and clinopyroxene Mg#, major and trace oxides. I define distinct groups of crystals based on ranges of $^{87}Sr/^{86}Sr$ and close with a discussion of geobarometric relationships. Summary Tables 7 and 8 also provide an overview of these data. There is a difference in spatial resolution between the electron microprobe analyses and the microsampling Sr isotope analyses: the electron beam associated with the microprobe has a spatial resolution 5 microns, whereas the microdrill yields a sample from a volume of, at minimum, $\sim 5.0 \times 10^6$ μm^3, due to the sample size required for the isotopic analyses (Figure 26). In order to compare major and trace element concentrations and pressure estimates with $^{87}Sr/^{86}Sr$, geochemical and geobarometric data were averaged for each electron microprobe crystal point included in the microdrilled core or rim volume.

Sr isotope ratio values for the clinopyroxene cores and rims range from 0.703365 ± 0.000058 to 0.710207 ± 0.000063. In pre-1971 samples, only samples 1669.1 and 1669.2 display cores that are lower in $^{87}Sr/^{86}Sr$ than their corresponding rims. In contrast, most post-1971 samples are characterized by core-rim pairs in which the rim is more radiogenic. Clinopyroxene 2004.1 A is the only exception for the post-1971 samples; its core is the most radiogenic of all analyzed samples.

Examining this dataset as a whole, the $^{87}Sr/^{86}Sr$ range is large. Overlap exists between pre-and post-1971 samples (Figures 27a-d and 28a- h), with no clear patterns for pre- and post-1971 cores and rims in terms of eruption year, whole rock $^{87}Sr/^{86}Sr$, and

geochemical constituents. A comparison of core, rim and whole rock values (Figure 27b, Tables 7 and 8) shows that the majority of analyzed pre-1971 cores and rims (1329, 1566, 1669.1 and 1886) systematically display isotopic disequilibrium and are all more radiogenic than their corresponding whole rock values. Exceptions include 1669.1 B-C, and sample 1669.2 cores (two analyses) and rim (one analysis); these crystals are in equilibrium with the corresponding $^{87}Sr/^{86}Sr$ whole rock value.

In post-1971 samples, much variation is observed: 1981 cores are generally in isotopic equilibrium with the whole rock, with the exception of 1981 D-C, which lies below the whole rock value. In contrast, all 1981 rims are more radiogenic than the whole rock value. Similarly, all 2001.1 cores are in equilibrium with its whole rock, while all of its rims are in disequilibrium at higher $^{87}Sr/^{86}Sr$. Sample 2004.1 cores and rims are all more radiogenic than the whole rock values with the exception of 2004.1 G. While 2004.1 G-C lies below the whole rock equilibrium value, its rim, 2004.1 G-R, lies in isotopic equilibrium with its whole rock.

Although much heterogeneity is exhibited in this dataset, three distinct groups, defined as Groups 1-3, were identified based upon their isotopic ranges and unique features among its clinopyroxene samples (Figure 27a, Figures 27 and 28). Group 1, a population of $^{87}Sr/^{86}Sr$ cores and rims ranging from ~0.70336 to ~0.70386 displays very minor, but generally systematic trends between pre- and post-1971 samples; these trends are presented in Figures 29a-d and 30a-d, and are described in further detail below.

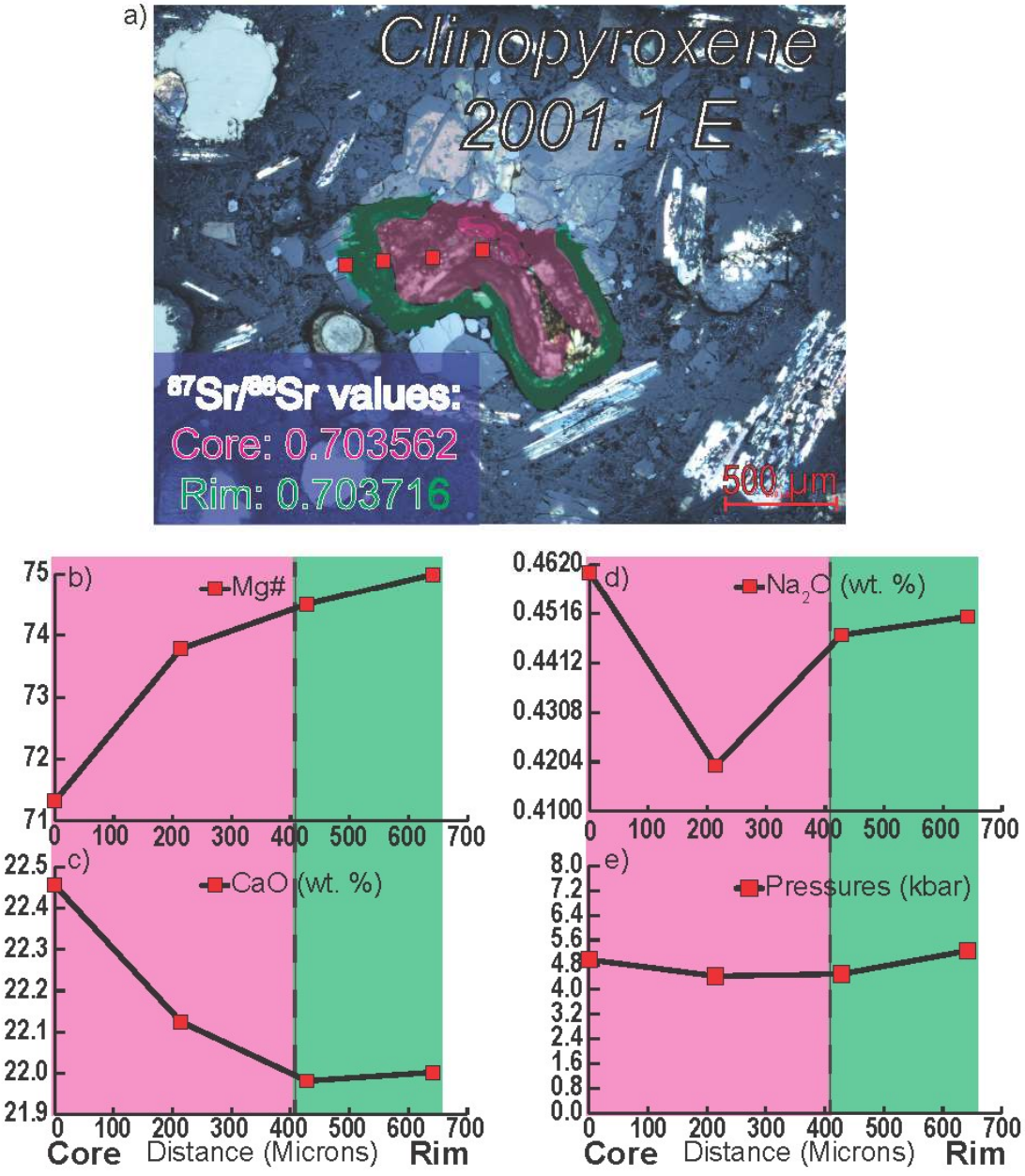

Figure 26. Comparison of spatial resolution of electron microprobe analyses vs. microdrilled regions: a) Green region of crystal drilled and defined as rim; pink region drilled and defined as core for Sr isotope analyses. Red squares are locations of electron microprobe analyses. The electron microprobe spatial resolution is much smaller (5 microns) compared to the 200-400 micron scale of the microdrilled region. Core to rim traverses show 4 electron microprobe analyses vs. b) Mg#, c) CaO (wt. %), d) calculated pressures. Diagrams divided into green (rim) and red (core) regions.

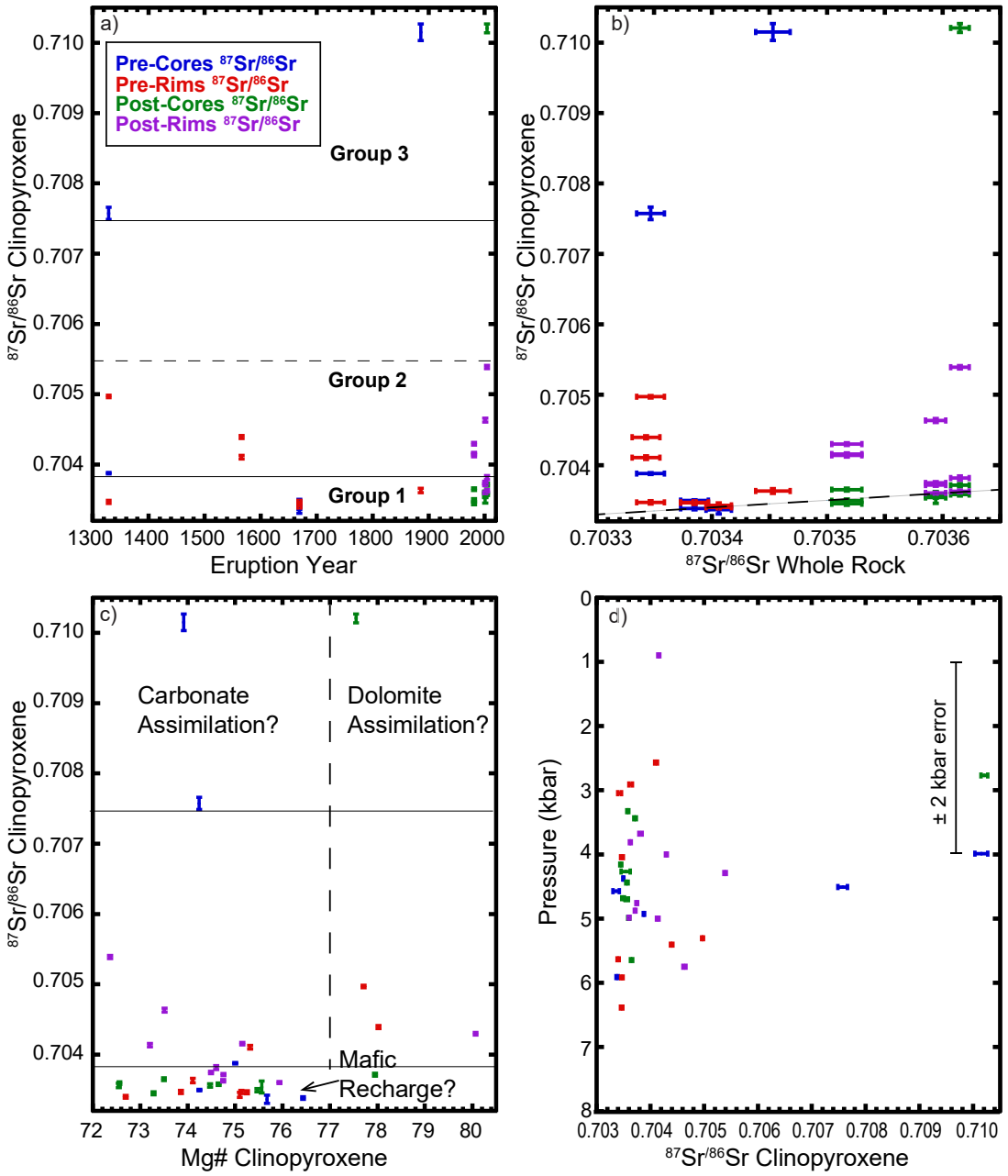

Figure 27a-d. Clinopyroxene core and rim $^{87}Sr/^{86}Sr$: a) eruption year vs. $^{87}Sr/^{86}Sr$ clinopyroxene, b) $^{87}Sr/^{86}Sr$ whole rock (data from Graham and Spera) vs. $^{87}Sr/^{86}Sr$ clinopyroxene, 1:1 indicated by dashed line, c) Mg# clinopyroxene vs. $^{87}Sr/^{86}Sr$ clinopyroxene, d) $^{87}Sr/^{86}Sr$ clinopyroxene vs. pressure (± 2 kbar error). Mg# and pressure values are averaged values of the microsampled region, as shown in Figure 26. 2 sigma uncertainty bars shown for select analyses; all others uncertainties are smaller than or equal to size of symbol.

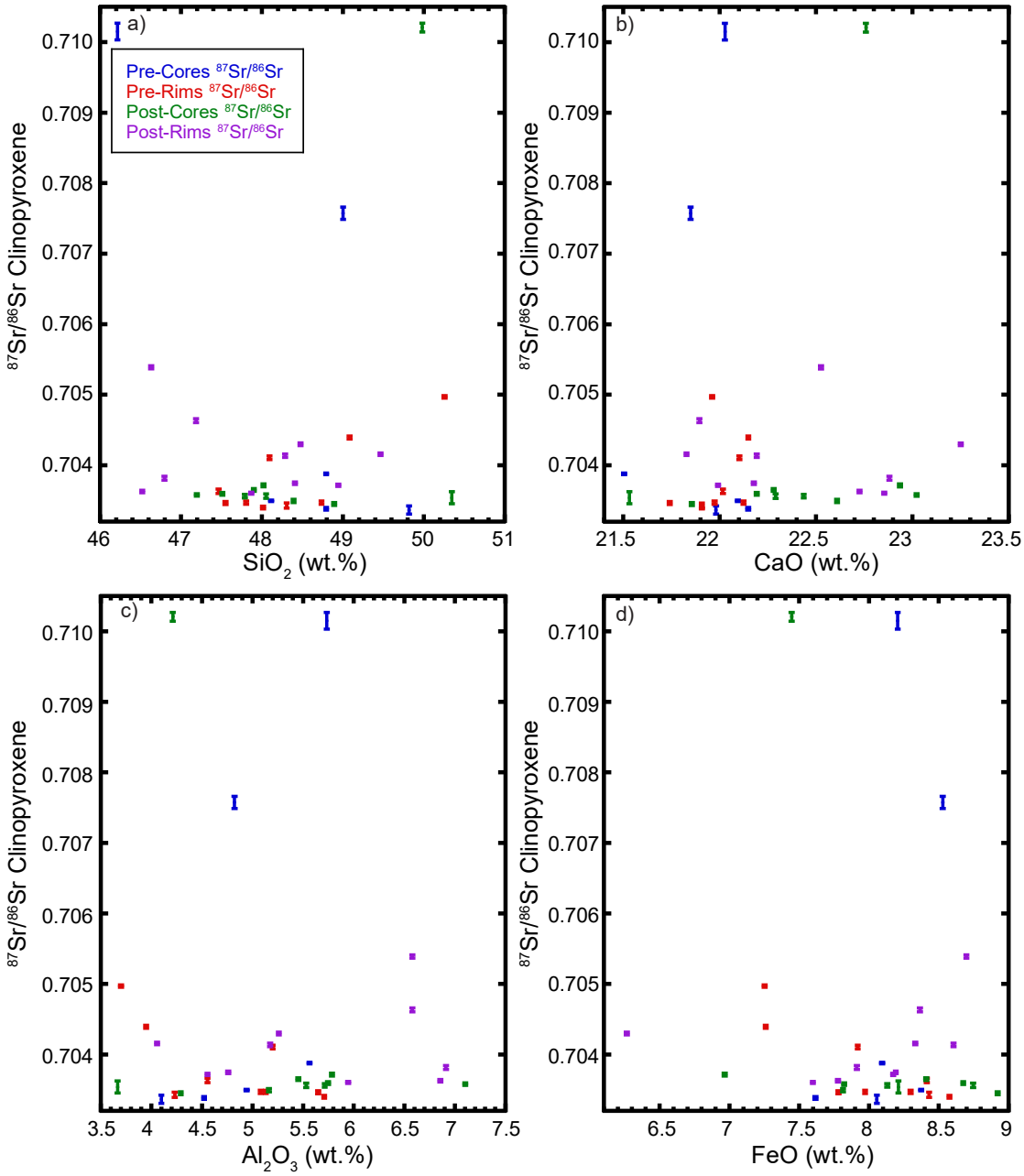

Figure 28a-d. Major and trace oxides (weight %) vs. $^{87}Sr/^{86}Sr$ clinopyroxene cores and rim for pre-1971 and post-1971 phenocrysts. Averaged values of the microsampled region are represented, as shown in Figure 26. 2 sigma uncertainty bars shown for select analyses; all others uncertainties are smaller than or equal to size of symbol.

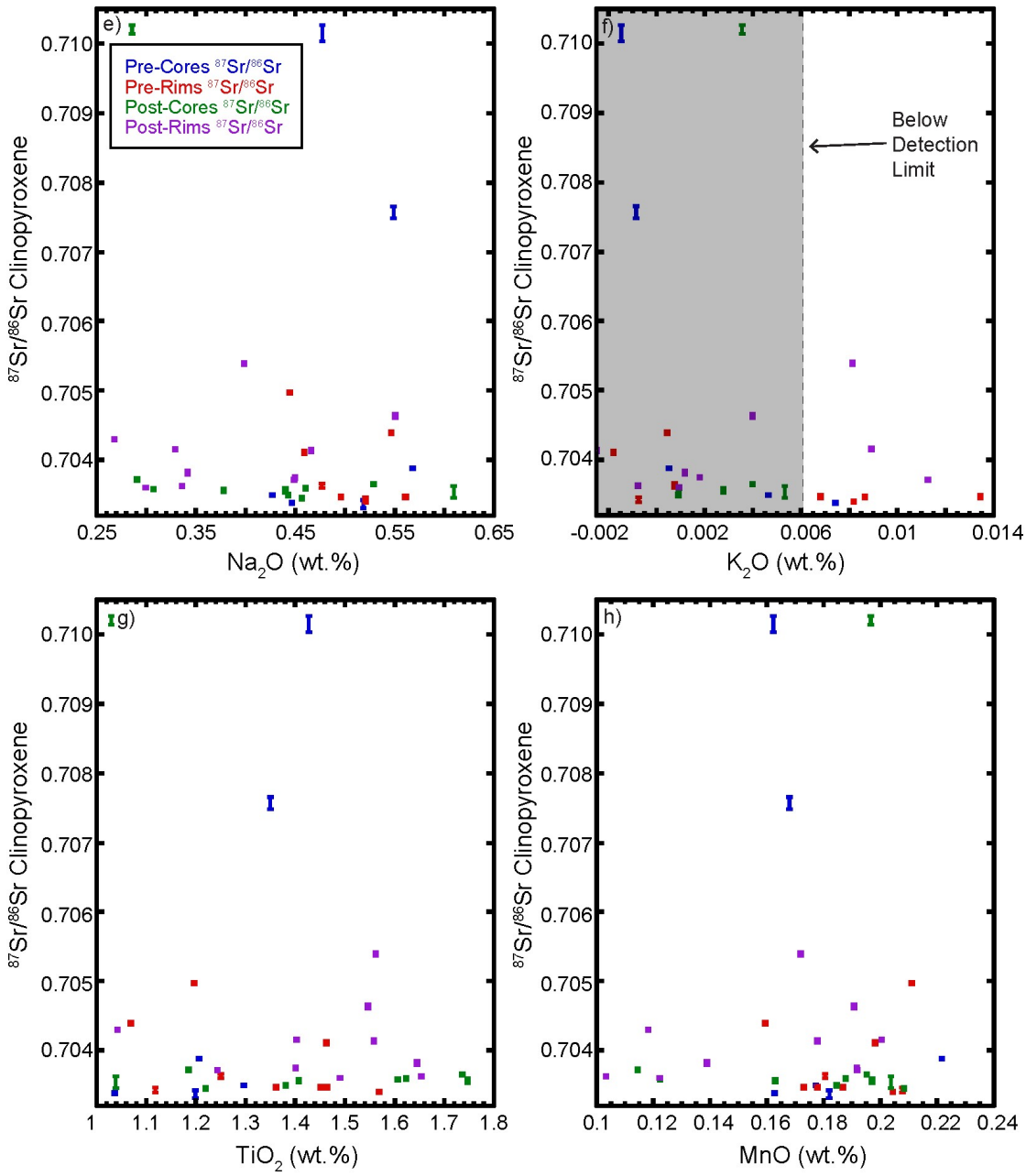

Figure 28e-h. Major and trace oxides (weight percent) vs. $^{87}Sr/^{86}Sr$ clinopyroxene cores and rim for pre-1971 and post-1971 phenocrysts. Averaged values of the microsampled region are represented, as shown in Figure 26. 2 sigma uncertainty bars shown for select analyses; all others uncertainties are smaller or equal to size of symbol.

In contrast, samples of Group 2 and 3 generally lack systematic relationships. An

anomalously high $^{87}Sr/^{86}Sr$ population of exclusively core samples defines Group 3, and includes 1329 B-C, 1886 L-C and 2004.1 A-C. Between these groups, Group 2 is defined by a population of clinopyroxene samples ranging from ~0.70386 to 0.70550. Notably, within this isotopic range, only one core is observed: the core of 1329 A-C, the corresponding and more-radiogenic rim of which (1329 A-R) also lies in this range. The remaining samples are exclusively pre-1971 rims (n = 3) and post-1971 rims (n = 5). The Group 2 core and rims express much overlap between pre- and post-1971 samples. Each of these three groups will be examined in further detail below.

Group 1: ~0.70336 to ~0.70386

Within this isotopic range, Figure 29a-d and Figure 30a-d display scattered but broadly systematic increases in $^{87}Sr/^{86}Sr$ over time, from pre-1971 to post-1971. In addition, a scattered but generally positive correlation is seen between clinopyroxene and whole rock $^{87}Sr/^{86}Sr$. The relationship between Mg# and radiogenic Sr is more complex and lacks clear systematics. Although scattered, $^{87}Sr/^{86}Sr$ broadly increases with increasing CaO, with post-1971 cores and rims displaying the highest values. Conversely, SiO_2, Na_2O and MnO generally decrease with increasing $^{87}Sr/^{86}Sr$, with those post-1971 cores and rims also exhibiting the highest Sr isotope ratios.

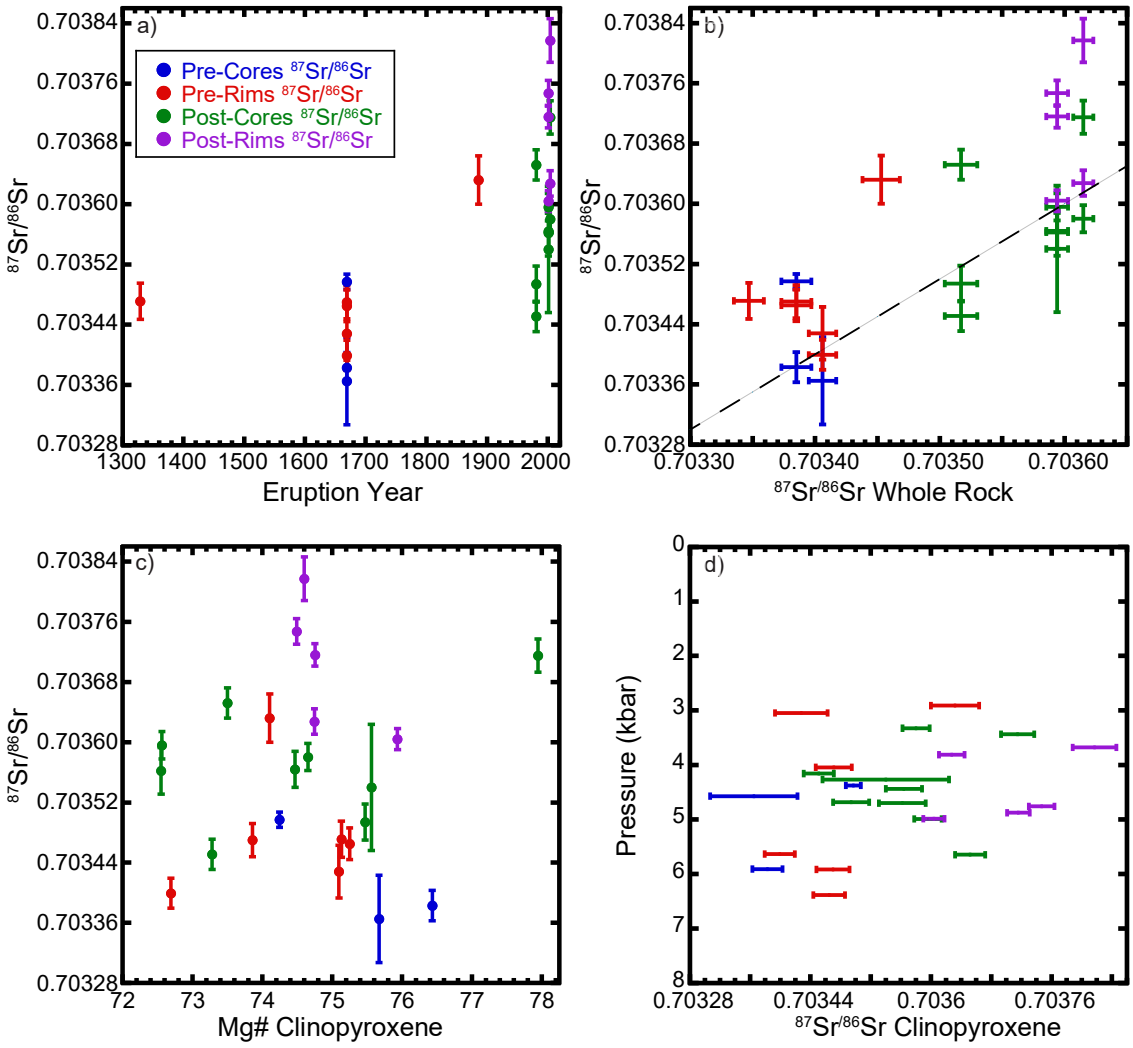

Figure 29a-d. Select clinopyroxene core and rim $^{87}Sr/^{86}Sr$ (Group 1 of Figure 27a, <0.70386): a) eruption year vs. $^{87}Sr/^{86}Sr$ clinopyroxene, b) $^{87}Sr/^{86}Sr$ whole rock (data from Graham and Spera) vs. $^{87}Sr/^{86}Sr$ clinopyroxene, 1:1 indicated by dashed line, c) Mg# clinopyroxene vs. $^{87}Sr/^{86}Sr$ clinopyroxene, d) $^{87}Sr/^{86}Sr$ clinopyroxene vs. pressure (± 2 kbar error). Mg# and pressure values are average values of the microsampled region, as shown in Figure 26. 2 sigma uncertainty bars shown for select analyses; all others uncertainties are smaller or equal to size of symbol.

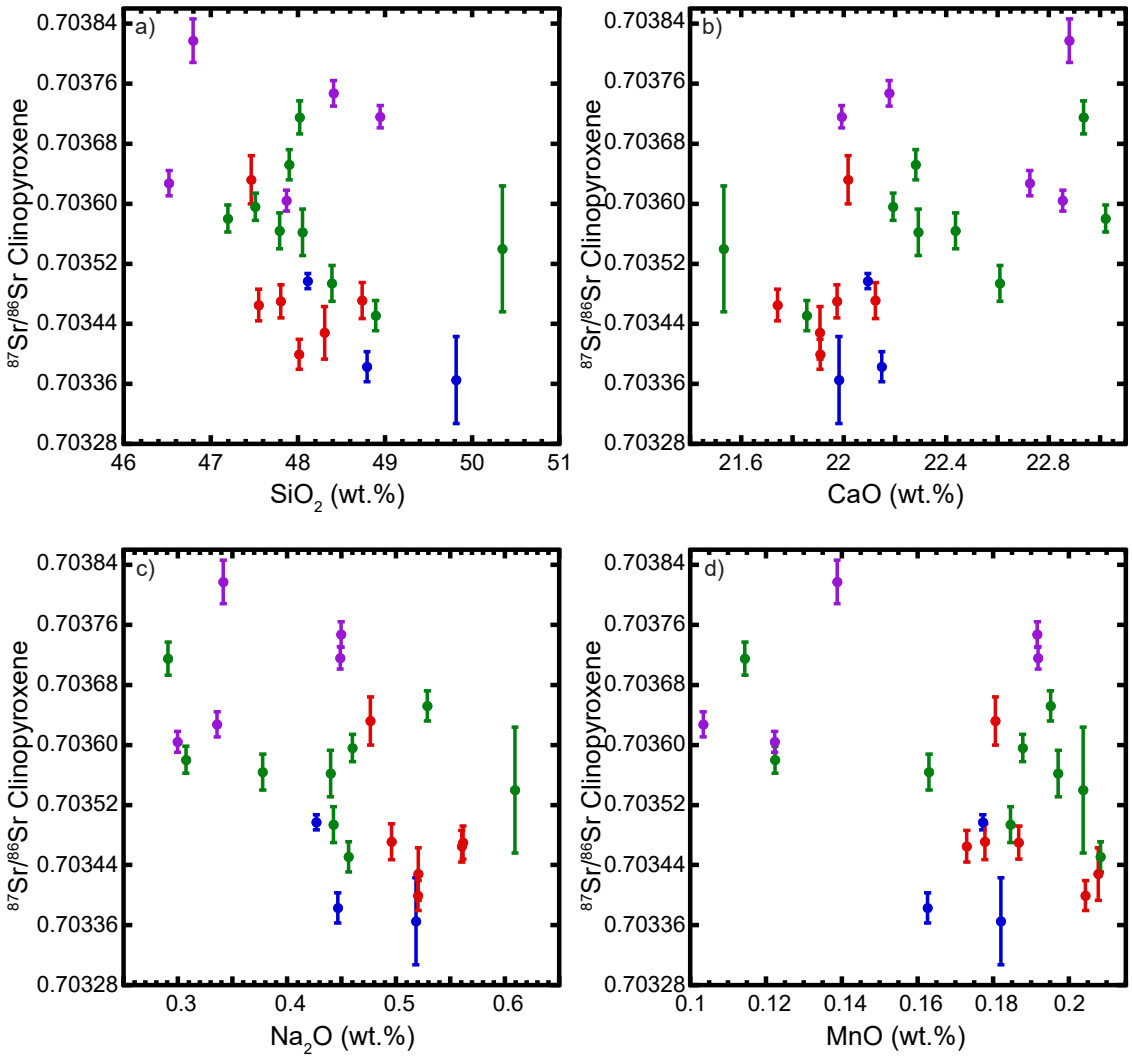

Figure 30a-d. Select clinopyroxene major and trace oxides (weight %) vs. $^{87}Sr/^{86}Sr$ (Group 1 of Figure 27a, <0.70386. Averaged values of the microsampled region are represented, as shown in Figure 26. 2 sigma uncertainty bars shown for select analyses; all others uncertainties are smaller or equal to size of symbol. Symbols same as Figure 29.

Group 2: *~0.70386 to 0.70550*

Among its nine samples, comprised of one pre-1971 core, three pre-1971 rims and five post-1971 rims, this isotopic population displays much heterogeneity. Notably, the single pre-1971 core displays the lowest $^{87}Sr/^{86}Sr$, and its corresponding rim is present in group 3; the two highest rim values, 1329 B-R and 2004.1 A-R, are paired with their corresponding highly-radiogenic cores of Group 2 (Figure 29a, Tables 7 and 8). With the exception of containing primarily rim samples, there are no observed systematic relationships with other geochemical parameters.

Group 3: ~0.70756 to ~0.71015

Three sample cores, two pre-1971 and one post-1971, are represented within this anomalously radiogenic Sr isotope range: 1329 B-C, 1886 L-C and 2004.1 A-C (Figures 27a-d and 28a-d, Tables 7 and 8). In contrast to the Group 1 samples, coherent trends are absent within this group. However, while there are no isotopic rim data for 1886 L, both 1329 B and 2004.1 A exhibit rims which are much less radiogenic, at 0.703471 ± 0.000024 and 0.705389 ± 0.000023, respectively. Among these three crystals, there is an observed increase in wt. % CaO with increasing radiogenic Sr, with the single post-1971 core displaying the highest value. FeO and Na_2O show the reverse trend, with the 2004.1 A the lowest in the geochemical components. Mg#, TiO_2, Al_2O_3, SiO_2 and MnO show more complexity. 2004.1 A is the most depleted of these three samples in TiO_2 and Al_2O_3, and the most enriched in Mg#, SiO_2 and MnO. Conversely, 1886 L-C is the most enriched in TiO_2 and Al_2O_3 are the most depleted in SiO_2 and MnO, while clinopyroxene 1329 B-C lies between the two samples.

Geobarometry

A clear correlation between pre- and post-1971 sample $^{87}Sr/^{86}Sr$ and pressure is lacking. Clinopyroxenes within both the ~0.70336 to ~0.70385 (Group 1) isotopic range and the ~0.70386 to 0.70550 (Group 3) isotopic range exhibit a pressure range 3-6 ± 2 kbar (Figures 27d and 29d, Tables 7 and 8) with the exception of the shallowest recorded microsampled crystal, 1981 L-R of group 1, at 1 ± 2 kbar. The anomalously-high ~0.70757 to ~0.71015 (Group 2) isotopic population, demonstrates a slightly more shallowly-constrained range of pressures at 3-5 ± 2 kbar therefore indicating that their growth occurred at common depths within the Etnean magmatic plumbing system (Figure 27d, Tables 7 and 8).

TABLE 7. SUMMARY OF SELECT PRE-1971 CLINOPYROXENE PRESSURE, GEOCHEMICAL AND $^{87}Sr/^{86}Sr$ AND WHOLE ROCK $^{87}Sr/^{86}Sr$ DATA:

Sample	P (kbar)	Mg#	SiO_2	CaO	Na_2O	WR MgO* EQ	WR MgO* Obs.	$^{87}Sr/^{86}Sr$ Whole Rock	error	$^{87}Sr/^{86}Sr$ Clinopyroxene	error
Pre-1971:											
1329.A-C	4.9	74.3	48.7	21.4	0.6	3.31	3.31	0.703350	1.20E-05	0.703880	1.10E-05
1329.A-I1	4.7	76.3	48.9	21.6	0.5	4.21	3.31			0.703880	1.10E-05
1329.A-I2	5.2	74.4	48.8	21.5	0.6	3.31	3.31			0.703880	1.10E-05
1329.A-R	5.3	77.7	50.3	22.0	0.4	5.18	3.31			0.704971	1.70E-05
1329.B-C	4.0	75.7	49.8	21.9	0.5	3.31	3.31			0.707574	8.80E-05
1329.B-I	5.0	72.8	48.3	21.8	0.6	3.31	3.31			0.707574	8.80E-05
1329.B-R	4.0	75.1	50.3	22.0	0.4	3.31	3.31			0.703471	2.40E-05
1566.D-C	3.8	74.1	47.2	22.1	0.6	3.27	3.27	0.703343	1.20E-05	0.704375†	5.00E-04†
1566.D-I1	5.7	77.8	49.0	22.2	0.5	5.18	3.27			0.704375†	5.00E-04†
1566.D-I2	6.1	78.1	49.5	22.1	0.5	5.44	3.27				
1566.D-I3	4.4	78.1	48.9	22.1	0.5	5.44	3.27			0.704395	2.10E-05
1566.D-R	6.4	77.9	49.3	22.2	0.6	5.41	3.27			0.704395	2.10E-05
1566.J-C	5.8	70.6	45.8	21.8	0.5	2.94	3.27	0.703343	1.20E-05	0.703439†	1.90E-04†
1566.J-I1	4.9	72.8	46.4	21.6	0.6	3.31	3.27			0.703439†	1.90E-04†
1566.J-I2	3.4	74.3	47.6	22.2	0.5	3.27	3.27			0.703439†	1.90E-04†
1566.J-I3	2.2	76.4	48.8	22.3	0.4	3.27	3.27			0.704106	2.50E-05
1566.J-R	2.9	74.2	47.4	21.9	0.5	3.27	3.27			0.704106	2.50E-05
1669.1.B-C	6.1	76.0	48.1	22.1	0.5	5.34	7.20	0.703385	1.20E-05	0.703383	2.00E-05
1669.1.B-I1	5.6	76.7	49.4	22.1	0.4	5.20	7.20			0.703383	2.00E-05
1669.1.B-I2	6.0	76.6	48.9	22.2	0.5	5.20	7.20			0.703383	2.00E-05
1669.1.B-I3	5.6	75.7	49.2	22.1	0.5	5.05	7.20				
1669.1.B-I4	6.4	74.7	49.3	21.6	0.5	4.89	7.20				
1669.1.B-I5	5.1	76.0	48.9	22.0	0.4	5.05	7.20				
1669.1.B-I6	7.1	76.8	48.1	21.9	0.6	5.20	7.20				
1669.1.B-I7	6.7	77.6	49.5	21.7	0.5	5.27	7.20			0.703465	2.10E-05
1669.1.B-I8	6.4	74.1	46.3	21.7	0.6	4.61	7.20			0.703465	2.10E-05
1669.1.B-R	6.1	74.0	46.8	21.8	0.6	4.61	7.20			0.703465	2.10E-05

Calculated clinopyroxene pressure error is ± 2 kbar.

All oxides are reported in weight percent.

*EQ Whole rock MgO represents an estimate of a whole rock MgO value that is in equilibrium with observed characteristics of clinopyroxene as defined by $K_D(Fe\text{-}Mg)^{cpx\text{-}whole\ rock}$ (=0.27 ± 0.03), and Obs. is the observed value for whole rock samples.

†$^{87}Sr/^{86}Sr$ were not used due to high error values.

TABLE 7. SUMMARY OF SELECT PRE-1971 CLINOPYROXENE PRESSURE, GEOCHEMICAL AND $^{87}Sr/^{86}Sr$ AND WHOLE ROCK $^{87}Sr/^{86}Sr$ DATA

Sample	P (kbar)	Mg#	SiO_2	CaO	Na_2O	WR MgO* EQ	WR MgO* Obs.	$^{87}Sr/^{86}Sr$ Whole Rock	error	$^{87}Sr/^{86}Sr$ Clinopyroxene	error
Pre-1971 (cont.):											
1669.1.C-1	4.8	71.8	46.0	22.1	0.4	2.94	7.20	0.703385	1.20E-05	0.703497	1.00E-05
1669.1.I-1	4.9	73.2	47.2	22.2	0.5	4.61	7.20			0.703497	1.00E-05
1669.1.I-2	5.7	72.6	46.4	22.0	0.5	4.61	7.20			0.703470	2.20E-05
1669.1.I-R	5.6	74.5	48.5	22.0	0.6	4.64	7.20			0.703470	2.20E-05
1669.1.C-2	3.0	75.4	48.9	22.0	0.3	4.89	7.20			0.703497	1.00E-05
1669.1.I-1	5.1	75.3	49.0	22.1	0.5	4.89	7.20			0.703497	1.00E-05
1669.1.I-2	4.1	75.5	49.5	22.0	0.5	4.89	7.20			0.703497	1.00E-05
1669.1.I-3	3.7	76.2	48.6	22.1	0.4	4.21	7.20			0.703497	1.00E-05
1669.1.I-4	6.6	73.1	47.4	21.8	0.6	4.61	7.20				
1669.1.I-R	5.7	75.3	48.8	22.0	0.5	4.89	7.20				
1669.2.F-C	5.9	71.7	47.3	21.8	0.6	2.94	4.97	0.703406	1.10E-05		
1669.2.F-I1	6.2	72.8	48.0	22.0	0.6	4.61	4.97				
1669.2.F-I2	5.4	73.1	47.9	22.0	0.5	4.61	4.97				
1669.2.F-I3	5.8	72.6	48.6	21.9	0.5	4.61	4.97			0.703399	2.00E-05
1669.2.F-R	5.5	72.8	47.4	22.0	0.5	4.61	4.97			0.703399	2.00E-05
1669.2.K-C	3.4	75.1	49.6	22.0	0.6	3.27	4.97			0.703365	5.80E-05
1669.2.K-I1	5.7	76.3	50.1	22.0	0.5	5.11	4.97			0.703365	5.80E-05
1669.2.K-I2	5.5	74.9	50.1	21.9	0.5	4.89	4.97			0.703428	3.50E-05
1669.2.K-R	0.6	75.3	50.5	21.9	0.4	3.32	4.97			0.703428	3.50E-05
1886.G-C	5.1	71.6	45.3	22.1	0.5	2.94	5.59	0.703453	1.50E-05		
1886.G-I1	2.5	76.3	48.9	21.6	0.4	4.97	5.59				
1886.G-I2	5.3	74.0	47.7	22.0	0.5	4.61	5.59				
1886.G-R	2.9	74.1	47.5	22.0	0.5	3.31	5.59			0.703632	3.20E-05
1886.L-C	5.7	71.6	46.8	21.9	0.5	2.94	5.59			0.710150	1.19E-04
1886.L-I1	3.5	74.6	45.9	22.1	0.5	4.89	5.59			0.710150	1.19E-04
1886.L-I2	2.8	75.5	45.9	22.1	0.4	3.76	5.59			0.710150	1.19E-04
1886.L-I3	5.7	76.4	47.3	22.6	0.4	4.97	5.59				
1886.L-R	4.1	76.4	47.3	22.4	0.4	4.97	5.59				

Calculated clinopyroxene pressure error is ± 2 kbar.

All oxides are reported in weight percent.

*EQ Whole rock MgO represents an estimate of a whole rock MgO value that is in equilibrium with observed characteristics of clinopyroxene as defined by $K_D(Fe\text{-}Mg)^{cpx\text{-}whole\ rock}$ (=0.27 ± 0.03), and Obs. is the observed value for whole rock samples.

TABLE 8. SUMMARY OF SELECT PRE-1971 CLINOPYROXENE PRESSURE, GEOCHEMICAL AND $^{87}Sr/^{86}Sr$ AND WHOLE ROCK $^{87}Sr/^{86}Sr$ DATA

Sample	P (kbar)	Mg#	SiO_2	CaO	Na_2O	WR MgO* EQ	WR MgO* Obs.	$^{87}Sr/^{86}Sr$ Whole Rock	error	$^{87}Sr/^{86}Sr$ Clinopyroxene	error
Post-1971											
1981.D-C	4.5	73.6	49.3	21.9	0.4	4.61	5.27	0.703517	1.30E-05	0.703451	2.00E-05
1981.D-I1	3.8	73.0	48.4	21.8	0.5	4.61	5.27			0.703451	2.00E-05
1981.D-I2	4.9	72.6	49.0	21.6	0.5	4.61	5.27			0.703451	2.00E-05
1981.D-I3	5.3	72.3	49.6	21.8	0.5	4.61	5.27			0.704298	1.80E-05
1981.D-R	4.0	80.1	48.5	23.3	0.3	6.16	5.27			0.704298	1.80E-05
1981.I-C	4.2	73.2	45.7	22.5	0.4	4.61	5.27			0.703652	2.00E-05
1981.I-I1	3.5	77.8	49.6	22.7	0.3	5.27	5.27			0.704137	2.40E-05
1981.L-C	4.7	75.5	48.4	22.6	0.4	4.89	5.27			0.703494	2.40E-05
1981.L-I1	5.7	76.5	50.1	22.2	0.5	5.27	5.27			0.703494	2.40E-05
1981.L-R	0.9	75.2	49.5	21.8	0.3	3.27	5.27			0.704156	1.80E-05
2001.1.B-C	2.8	75.3	50.0	21.5	0.6	3.32	5.70	0.703594	8.75E-06	0.703540	8.40E-05
2001.1.B-I1	5.7	75.8	50.7	21.6	0.6	4.82	5.70			0.703540	8.40E-05
2001.1.B-I2	5.3	74.9	50.5	21.5	0.5	4.89	5.70				
2001.1.B-I3	7.3	73.8	48.4	21.4	0.7	4.61	5.70			0.704633	2.70E-05
2001.1.B-R	4.2	73.2	46.0	22.4	0.4	4.61	5.70			0.704633	2.70E-05
2001.1.D-C	4.9	72.5	47.6	22.3	0.4	4.61	5.70			0.703596	1.80E-05
2001.1.D-I1	5.1	72.6	47.4	22.1	0.5	4.61	5.70			0.703596	1.80E-05
2001.1.D-I2	5.1	73.3	48.0	22.3	0.5	4.61	5.70			0.703596	1.80E-05
2001.1.D-R	4.4	75.7	48.8	22.1	0.4	4.72	5.70			0.703747	1.70E-05
2001.1.E-C	5.0	71.3	47.3	22.5	0.5	2.94	5.70				
2001.1.E-I1	4.4	73.8	48.8	22.1	0.4	4.61	5.70			0.703562	3.10E-05
2001.1.E-I2	4.5	74.5	49.1	22.0	0.4	4.64	5.70			0.703562	3.10E-05
2001.1.E-R	5.3	75.0	48.8	22.0	0.5	4.89	5.70			0.703716	1.50E-05
2001.1.H-C	5.9	74.4	49.2	22.0	0.5	4.94	5.70				
2001.1.H-I1	3.0	74.5	46.4	22.9	0.3	3.27	5.70			0.703564	2.40E-05
2001.1.H-I2	6.3	75.2	47.3	23.1	0.3	2.94	5.70			0.703564	2.40E-05
2001.1.H-I3	5.8	78.9	48.9	23.0	0.2	4.61	5.70			0.703604	1.40E-05
2001.1.H-R	4.1	73.0	46.9	22.7	0.4	3.80	5.70				

Calculated clinopyroxene pressure error is ± 2 kbar.

All oxides are reported in weight percent.

*EQ Whole rock MgO represents an estimate of a whole rock MgO value that is in equilibrium with observed characteristics of clinopyroxene as defined by $K_D(Fe\text{-}Mg)^{cpx\text{-}whole\ rock}$ (=0.27 ± 0.03), and Obs. is the observed value for whole rock samples.

TABLE 8. SUMMARY OF SELECT PRE-1971 CLINOPYROXENE PRESSURE, GEOCHEMICAL AND $^{87}Sr/^{86}Sr$ AND WHOLE ROCK $^{87}Sr/^{86}Sr$ DATA

Sample	P (kbar)	Mg#	SiO_2	CaO	Na_2O	WR MgO* EQ	WR MgO* Obs.	$^{87}Sr/^{86}Sr$ Whole Rock	error	$^{87}Sr/^{86}Sr$ Clinopyroxene	error
Post-1971 (cont.):											
2004.1.A-C	2.4	77.8	49.8	22.7	0.3	4.97	4.97	0.703615	8.00E-06	0.710207	6.30E-05
2004.1.A-I1	3.1	77.3	50.2	22.8	0.3	4.97	4.97			0.710207	6.30E-05
2004.1.A-R	4.3	72.4	46.6	22.5	0.4	4.61	4.97			0.705389	2.30E-05
2004.1.E-C	3.5	77.3	47.3	23.0	0.3	4.97	4.97			0.703715	2.20E-05
2004.1.E-I1	3.4	78.6	48.7	22.9	0.3	5.82	4.97			0.703715	2.20E-05
2004.1.E-I2	3.7	75.4	46.7	22.9	0.3	4.97	4.97			0.703817	2.90E-05
2004.1.E-R	3.6	73.8	46.9	22.8	0.4	4.61	4.97			0.703817	2.90E-05
2004.1.G-C	3.3	74.7	47.5	23.1	0.3	4.97	4.97			0.703562	1.80E-05
2004.1.G-I1	3.4	74.6	46.9	23.0	0.3	4.97	4.97			0.703562	1.80E-05
2004.1.G-I2	3.4	74.4	46.7	23.0	0.3	4.97	4.97			0.703606	1.70E-05
2004.1.G-R	4.2	75.1	46.3	22.4	0.4	4.97	4.97			0.703606	1.70E-05

Calculated clinopyroxene pressure error is ± 2 kbar.

All oxides are reported in weight percent.

*EQ Whole rock MgO represents an estimate of a whole rock MgO value that is in equilibrium with observed characteristics of clinopyroxene as defined by $K_D(Fe\text{-}Mg)^{cpx\text{-}whole\ rock}$ (=0.27 ± 0.03), and Obs. is the observed value for whole rock samples.

CHAPTER V

DISCUSSION

While Mt. Etna is one of the most well-documented volcanoes in the world (Martelli *et al.*, 2008), its extensive history is marked by both progressive and dramatic shifts in its geochemical, seismic and eruptive behavior, representing a continually evolving and highly dynamic system (Corsaro and Pompilio, 2000). Data presented in this study (*in situ* clinopyroxene textural, geochemical and isotopic data, and calculated pressures of formation) provide an opportunity to characterize Mt. Etna's magmatic system, and thereby, further elucidate the roles of magmatic pathways such as fractional crystallization, crustal contamination, recharge and mixing within the Etnean magmatic plumbing system, including the source and timing of alkali-enrichment. These data also help to reconstruct the structure of Mt. Etna's subvolcanic plumbing system and elucidate its evolution in time and space.

In the following sections, I will discuss how *in situ* clinopyroxene textural, geochemical, geobarometric and isotopic data help to address and resolve several questions regarding the last 700 years of volcanic history at Mt. Etna, Sicily:

1) What information does clinopyroxene provide about the location of the primary zone(s) of crystallization?
2) What magmatic processes are implied by the integration of whole rock data, clinopyroxene textures, and core-to-rim clinopyroxene major element and Sr isotope data?

3) What inferences and constraints may be made regarding the source and timing of alkali-enrichment?
4) What does the Etnean magmatic storage and transport system look like with regard to its structure, location, size and geometry, and what do pre- and post-1971 variations tell us about its evolution from 1329-2004 AD?

Clinopyroxene Crystallization Regime

Several researchers (Chiarabba *et al.*, 2000; Laigle and Hirn, 1999; Murru and Montuori, 1999; Murru, 2005; Murru *et al.*, 2007) have used seismological evidence to identify a strong high-velocity anomaly located in the mid- to upper crust beneath the Etnean edifice. Monitoring seismic activity and applying tomographic modeling, Chiarabba *et al.* (2000) produced a three-dimensional velocity model which revealed the presence of high-density cumulates of solidified magma intrusions in the crust, containing portions of melt, at ~3-18 km depth. This shallow intrusive area is likely composed of vertical dikes and lateral sills which are also locations of preferential magma ponding and differentiation (Armienti *et al.*, 2004; Murru and Montuori, 1999; Murru, 2005; Trigila *et al.*, 1990). While there is no evidence for a large low-velocity anomaly in the mid- to upper-crust, Armienti *et al.* (2004, 2012) describe potential locations of magma ponding at the mantle-crust boundary (20-25 km, Hirn *et al.*, 1997), possibly indicating a magma source region at depth. This concept of a deep magma reservoir is described by many others researchers, as well, and likely represents a feeding zone for the high-velocity magma mush and melt/cumulate area at shallower depths

(Chiarabba *et al.*, 2000; Laigle and Hirn, 1999; Patanè *et al.*, 2004, 2006; Sharp *et al.*, 1980).

Based on pressure estimates of 0-7 ± 2 kbar (approximate depth equivalent to surface-21 km ± 6 km) presented in the Chapter IV and Figure 21, the clinopyroxene crystallization zone ranges from below the Moho (~27 km) to the upper crust (<6 km); these estimates are consistent with experimental studies (Trigila *et al.*, 1990) and geobarometric and thermodynamic modeling (Armienti *et al.*, 2004, 2007; Ghiorso, 2002; Moses, 2010). As demonstrated by the mean pressure range (Figure 22), the dominant range of clinopyroxene growth occurs at approximately 4.2 kbar (~2.9-5.5 kbar, ~8.7-16.5 km). These data are consistent with the concept of a multi-stage, polybaric crystallization history for Mt. Etna, primarily within a crustal-scale magmatic system (Armienti *et al.*, 2004, 2012; Corsaro and Pompilio, 2000; Tonarini *et al.*, 2001). Additionally, the documentation of crustal xenoliths in historic and recent Etnean lavas indicates interaction between magmas and the heterogeneous shallow crust: a 10-km-thick sedimentary-metamorphic pile composed of the autochthonous carbonate units of the Hyblean Foreland, which is overlain by the allochthonous flyschoid series of Apeninic-Maghrebian Chain (Romano, 1983; Clocchiatti *et al.*, 1988; Lentini *et al.*, 1994; Michaud, 1995). The dominant zone of crystallization, at 4.2 kbar (~2.9-5.5 kbar, ~8.7-16.5 km), indeed suggests that a primary magma storage zone exists within the Hyblean carbonate basement that resides at approximately 5-15 km depth, (1.67 to 5 kbar) (Heap *et al.*, 2013). The Hyblean Plateau is composed of an autochthonous series of limestone and dolomite, in which long-standing magma bodies are inferred to be present

based on several seismological and experimental methods: mapping of *b*-values (Murru *et al.*, 1999), P-wave-inversion tomography (Chiarabba *et al.*, 2000; Villaseñor *et al.*, 1998), and thermo-mechanical numerical modeling (Bonaccorso *et al.*, 2010; Del Negro *et al.*, 2009). Additionally, eccentric reservoirs or peripheral dikes are also recorded at these common depth intervals within the carbonate substratum, feeding recent flank eruptions (Acocella *et al.*, 2013; Andronico *et al.*, 2004; Behncke and Neri, 2003; Bonforte *et al.*, 2009; Carbone *et al.*, 2009).

Magmatic Processes Recorded by Clinopyroxene Crystals

Magma differentiation and evolution pathways are dominated by the dynamics of magmatic recharge and mixing processes, assimilation of country rock, and fractional crystallization (RAFC) (Bohrson and Spera, 2001). These magmatic pathways are recorded in the petrography, textures, geochemistry and isotopic signatures of the erupted products and their minerals. The following sections will examine these features within the pre- and post-1971 samples of 1329-2004 AD, to assess the efficacy of key processes of a) fractional crystallization, b) magmatic recharge, focusing primarily on clinopyroxene Mg#, and c) crustal assimilation/contamination, focusing on clinopyroxene wt. % CaO. Finally, three phenocrysts are discussed in detail in order to highlight the dominant RAFC pathways recorded throughout their petrogenetic histories.

Core to Rim Characteristics of Clinopyroxene: ΔCaO vs. $\Delta Mg\#$

Petrographic, compositional, geobarometric and isotopic complexity among clinopyroxene support a highly dynamic, crustal-scale, polybaric crystallization regime (Armienti *et al.*, 2004; Corsaro and Pompilio, 2000; Corsaro *et al.*, 2006; Pitcher, 2011;

Viccaro *et al.*, 2010, this study), providing evidence for magmatic ascent through pathways within a plexus of interconnected dikes and sills. In such a dynamic system, a core-to-rim profile of a single crystal may reveal complex geochemical pathways from which multiple magmatic processes, such as recharge, crustal assimilation, and fractional crystallization may be inferred.

In order to characterize these magmatic processes, CaO (wt. %) and Mg# were selected to explore distinct geochemical pathways. Due to the anomalous abundance of CaO (wt. %), particularly in 1886 and post-1971 phenocrysts as well as 1974 microphenocrysts (Figure 17), this constituent was selected in order to: a) probe clinopyroxene core-to-rim changes with CaO among all clinopyroxene phenocrysts and 1974 microphenocrysts, and b) to represent potential crustal assimilation of carbonate wall rock into basaltic magma. Mg# was similarly selected to represent the addition of a hotter, more mafic recharge magma into the system, and/or the occurrence of dolomite wall rock assimilation. Electron microprobe analyses were performed along a core-to-rim transect where analyses (five micron spatial resolution) were spaced at approximately every 50-200 microns, and therefore may not reflect every geochemical "event" recorded within the crystal's history.

Delta CaO and Mg# diagrams are presented in Figures 31a-c (i.e. ΔCaO and ΔMg#, Figures 31a-e). Note that two types of delta calculations were performed: a) a preceding intermediate to rim calculation, in which the rim value is subtracted from the intermediate value, and b) an intermediate-intermediate calculation, in which the intermediate value is subtracted from the next intermediate value, continuing to the core

value. Figure 31d shows the four delta-delta quadrants and my interpretations of the associated processes: fractional crystallization, magma recharge, assimilation of crustal rocks, and recharge accompanied by carbonate assimilation. Clinopyroxene are presented in three distinct populations: Figure 31a displays pre-1971 samples, Figure 31b reveals post-1971 samples, and, Figure 31c represents clinopyroxene samples which exhibit exclusively CaO wt. % values greater than 22.5, in order to further probe this particular population. The majority of these crystal profiles are clustered within ±3.0 ΔMg# and ±0.25 ΔCaO, while a population of more distinct crystal profiles resides in each of the quadrants, as well.

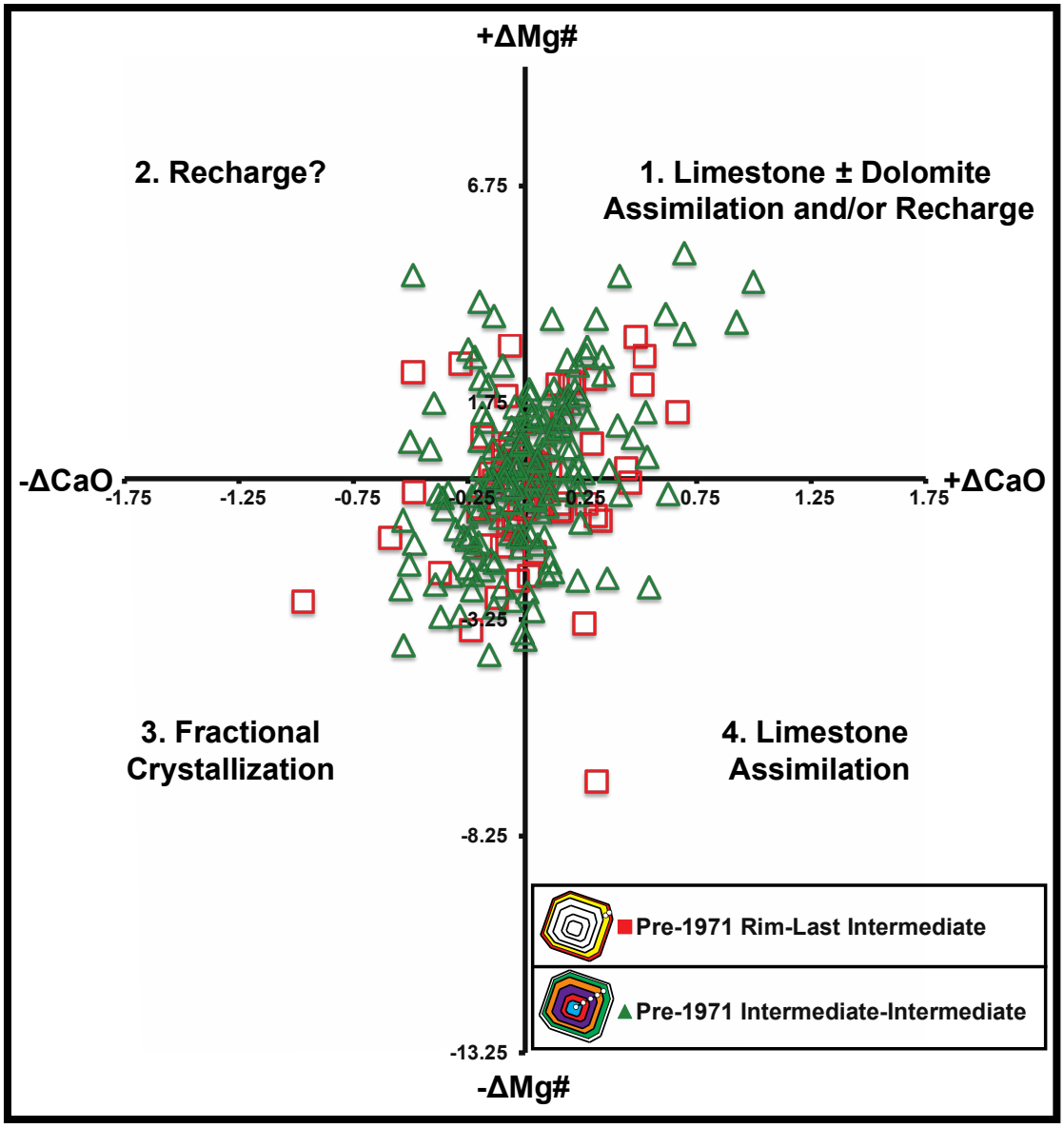

Figure 31a. ΔCaO vs. ΔMg# diagrams. Pre-1971 clinopyroxene analyses recording geochemical evidence for RAFC processes. See text for definitions of ΔMg# and ΔCaO.

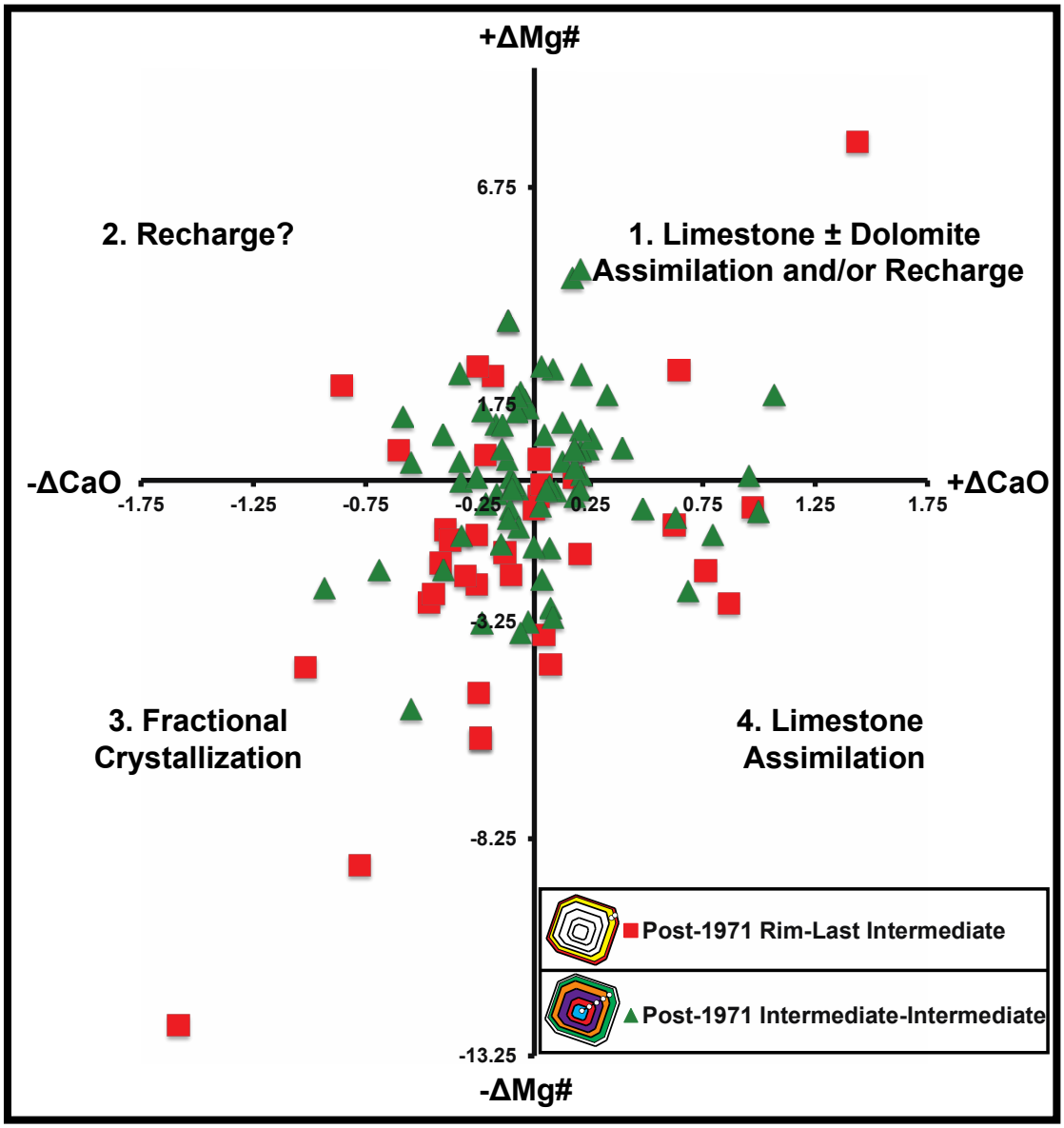

Figure 31b. ΔCaO vs. ΔMg# diagrams. Post-1971 clinopyroxene analyses recording geochemical evidence for RAFC processes. See text for definitions of ΔMg# and ΔCaO.

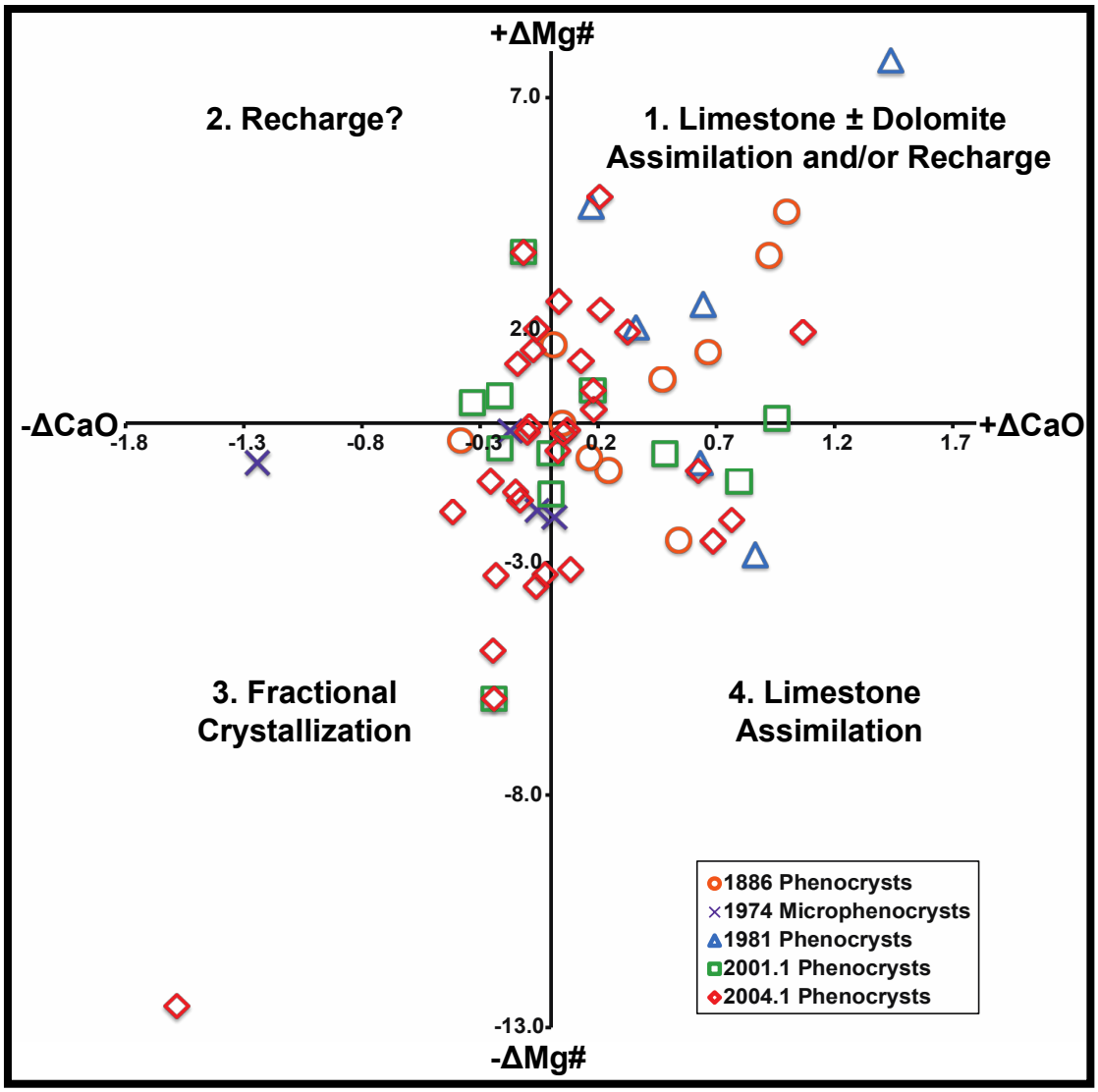

Figure 31c. ΔCaO vs. ΔMg# diagrams. Select clinopyroxene with >22.5 CaO (wt.%), recording geochemical evidence for RAFC processes. See text for definitions of ΔMg# and ΔCaO.

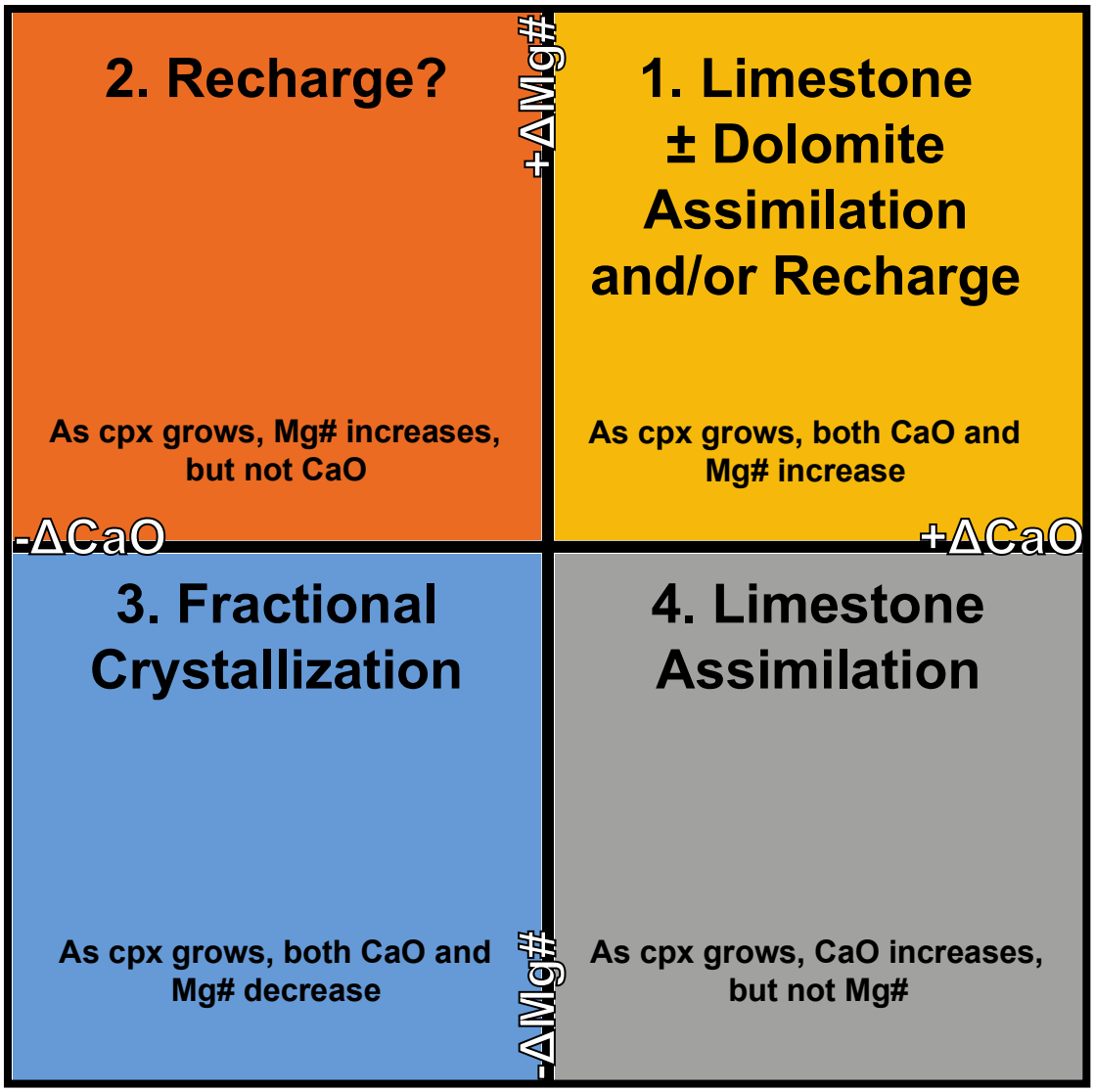

Figure 31d. ΔCaO vs. ΔMg# diagrams. Interpretation of processes represented by ΔCaO vs. ΔMg# diagrams. See text for discussion and definitions of ΔMg# and ΔCaO.

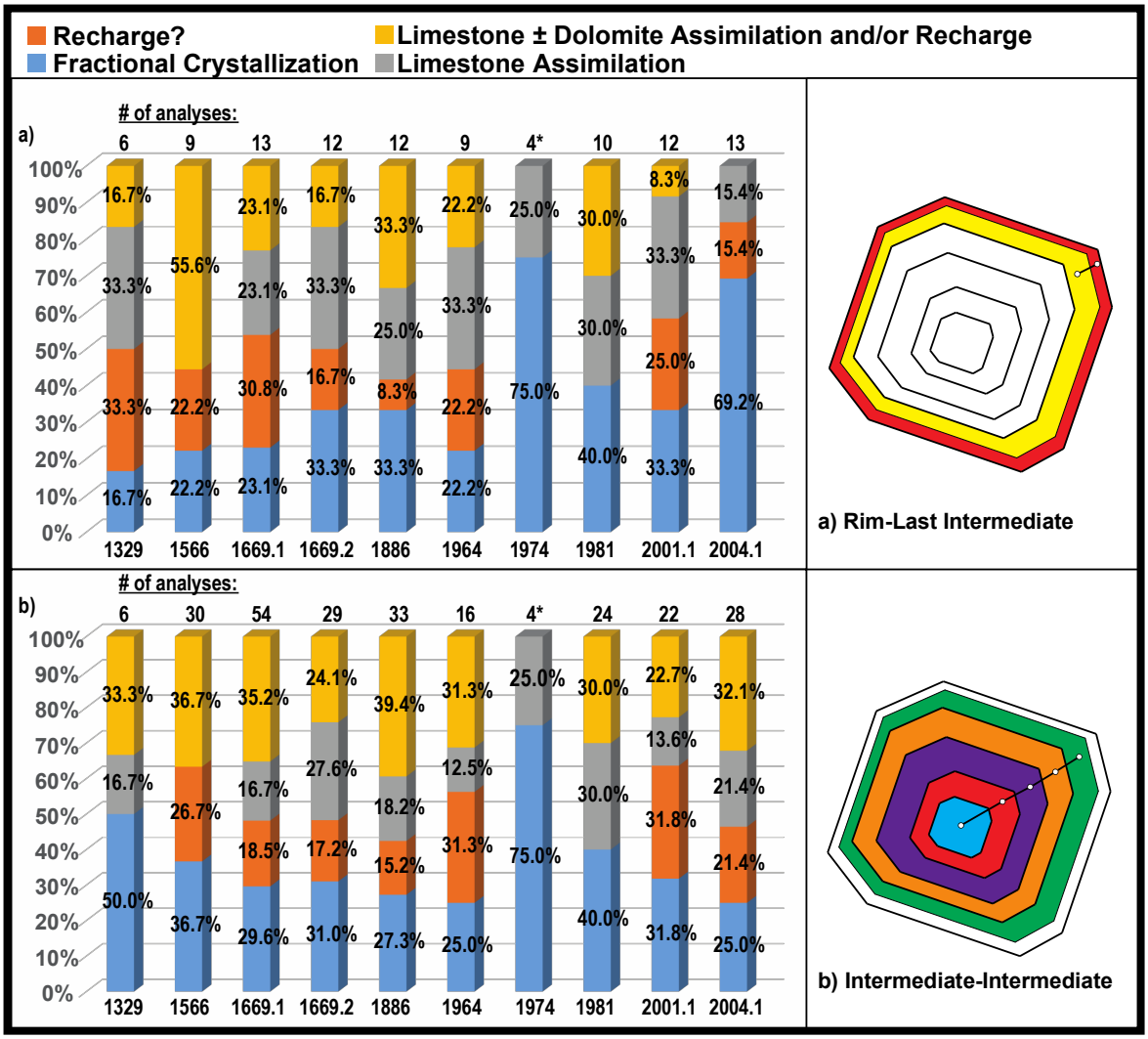

Figure 31e. ΔCaO vs. ΔMg# diagrams. Frequency diagrams for sample number in order of eruption: a) Frequency diagrams illustrate percentage of rim-last intermediate that plot in Quadrants 1-4 of Figure 32d, b) Frequency diagrams illustrate percentage of intermediate-intermediate that plot in Quadrants 1-4 of Figure 31d.

Evidence for Fractional Crystallization

As displayed in Figures 32a and 32b, whole rock data from eruptions of 1329-2004 AD show correlations that strongly suggest an important role for fractional crystallization. For example, the trend for MgO vs. SiO_2 (Figure 32a) is relatively tightly constrained and negatively correlated, as anticipated for fractionation of mafic phases

such as olivine and clinopyroxene. Systematic relationships observed among whole rock trace element concentrations (Figure 33a-e) are also consistent with fractional crystallization process. Additionally, consistent with the major and trace element trends, phenocrystic clinopyroxene and olivine are observed (refer to Chapter IV, petrography section) in most samples. Oscillatory zoning textures in selected clinopyroxene are present in most samples, consistent with equilibrium or near-equilibrium crystallization. Such textural zoning is prominent in all pre- and post-1971 samples, with the exception of 1329 clinopyroxene phenocrysts (n = 5), which display a lack of compositional zoning.

Fractional crystallization is also supported by chemical data from core to rim traverses in clinopyroxene. Referring to Figures 31a-d, those crystals that plot in Quadrant 3 represent a decrease in CaO as well as Mg# along a core to rim profile of the crystal, consistent with decreasing CaO in response to clinopyroxene crystallization and a decrease in Mg# consistent with clinopyroxene and olivine crystallization. In addition, as observed in Figures 13 and 14, microphenocrysts systematically exhibit lower Mg#, consistent with crystallization from a more highly fractionated melt.

Intriguingly, the two crystal profiles within Quadrant 3 that exhibit a decrease in the ΔMg# greater than 8.25 (Figure 31b), are from the 2004.1 lava flow, which also contains similarly evolved microphenocrysts, thus indicating that a population of crystals from this lava flow grew from a melt more evolved than that represented by the whole rock. These low-Mg# 2004.1 crystals lie within a range of 67.1-70.1 Mg#, similar to the evolved 1974 microphenocrysts which range from 67.3-70.2 Mg# (Figure 13). Furthermore, collectively, geobarometry indicates that these crystals grew at ~4-6 ± 2

kbar, as seen in Figure 24. Additionally, as displayed in Figure 31e, the growth profile of a), Rim-Last Intermediate, is dominated by the fractional crystallization pathway for both the 1974 and 2004.1 flows. Overall, this may indicate that the magma erupted in 2004 interacted with a batch of highly evolved melt located at ~4-6 ± 2 kbar from which these crystals inherited this low-Mg# composition.

As presented and discussed in Putirka (2008) and Armienti *et al.* (2012), and described in detail in Chapter III, equilibrium between clinopyroxene and the nominal coexisting liquid, which is inferred from the whole rock composition of each distinct lava flow, $K_D(Fe\text{-}Mg)^{(cpx\text{-}liq)}$, is achieved at 0.27 ± 0.03 (Figures 34 and 35). However, as displayed in Figure 32a, the majority of clinopyroxene cores, intermediates, rims and microphenocrysts from the samples demonstrate a range greater or less than the 0.27 ± 0.03, thus representing disequilibrium among clinopyroxene and the whole rock. Values that are higher than 0.27 ± 0.03 represent clinopyroxene compositions that are more evolved than those that would be in equilibrium with the whole rock, while values below 0.27 ± 0.03 represent compositions that are more mafic than clinopyroxene that would be in equilibrium with the corresponding whole rock. The presence of clinopyroxene above, below, and within the field of equilibrium within a single sample, demonstrates the presence of mixed crystal populations, and therefore open-system magma processes at work, potentially including magma recharge/mixing and crustal assimilation. These data may also imply that these clinopyroxene grew within a dynamic and interactive system

in which crystals are recycled one or several times in the magmatic system before inclusion in the final host magma; such crystals are referred to as antecrysts (Jerram and Martin, 2008).

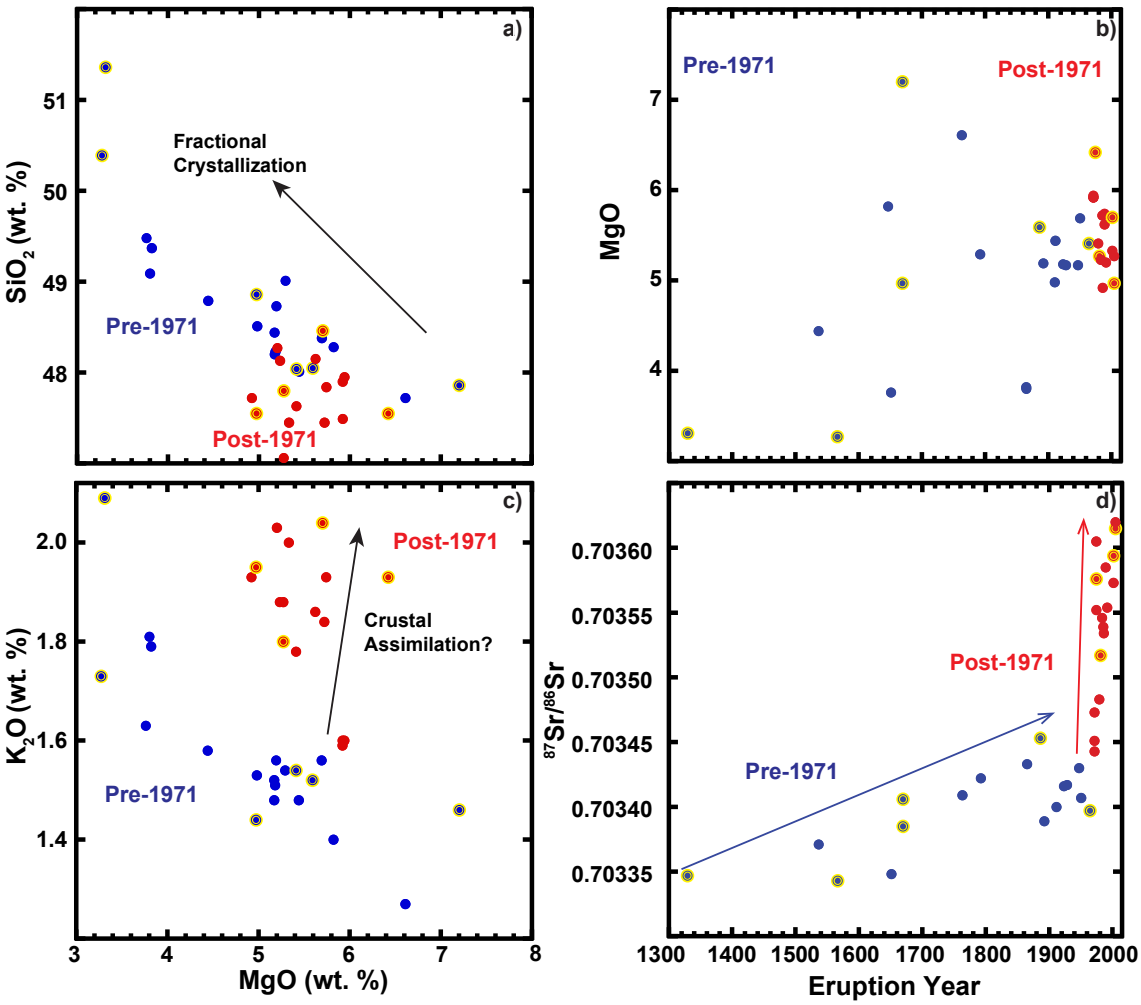

Figure 32a-d. Whole rock data plots for pre- and post-1971 samples: a) MgO vs. SiO_2, b) Year vs. MgO, c) MgO vs. K_2O, d) Year vs. $^{87}Sr/^{86}Sr$. Samples used in this study are highlighted in yellow.

Figure 33a-e. Whole rock MgO (wt. %) vs. select trace element concentrations (ppm) from pre- and post 1971 samples (1329-2004 AD), demonstrating the selective enrichment in alkali elements, and providing evidence for fractional crystallization, recharge and crustal assimilation in the Etna magma storage and transport system: MgO vs. a) Ba, b) Sr, c) Nb, d) Rb, e) La.

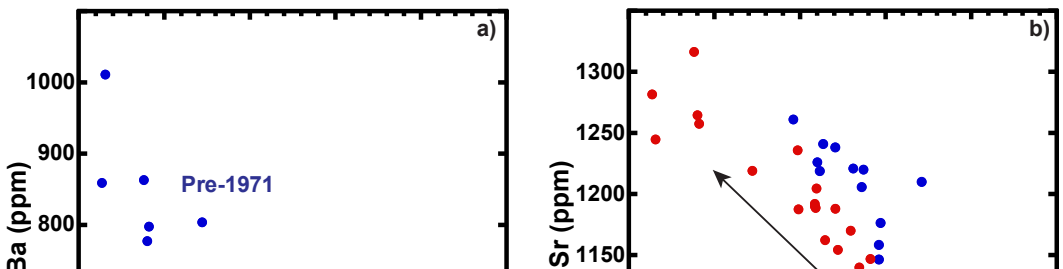

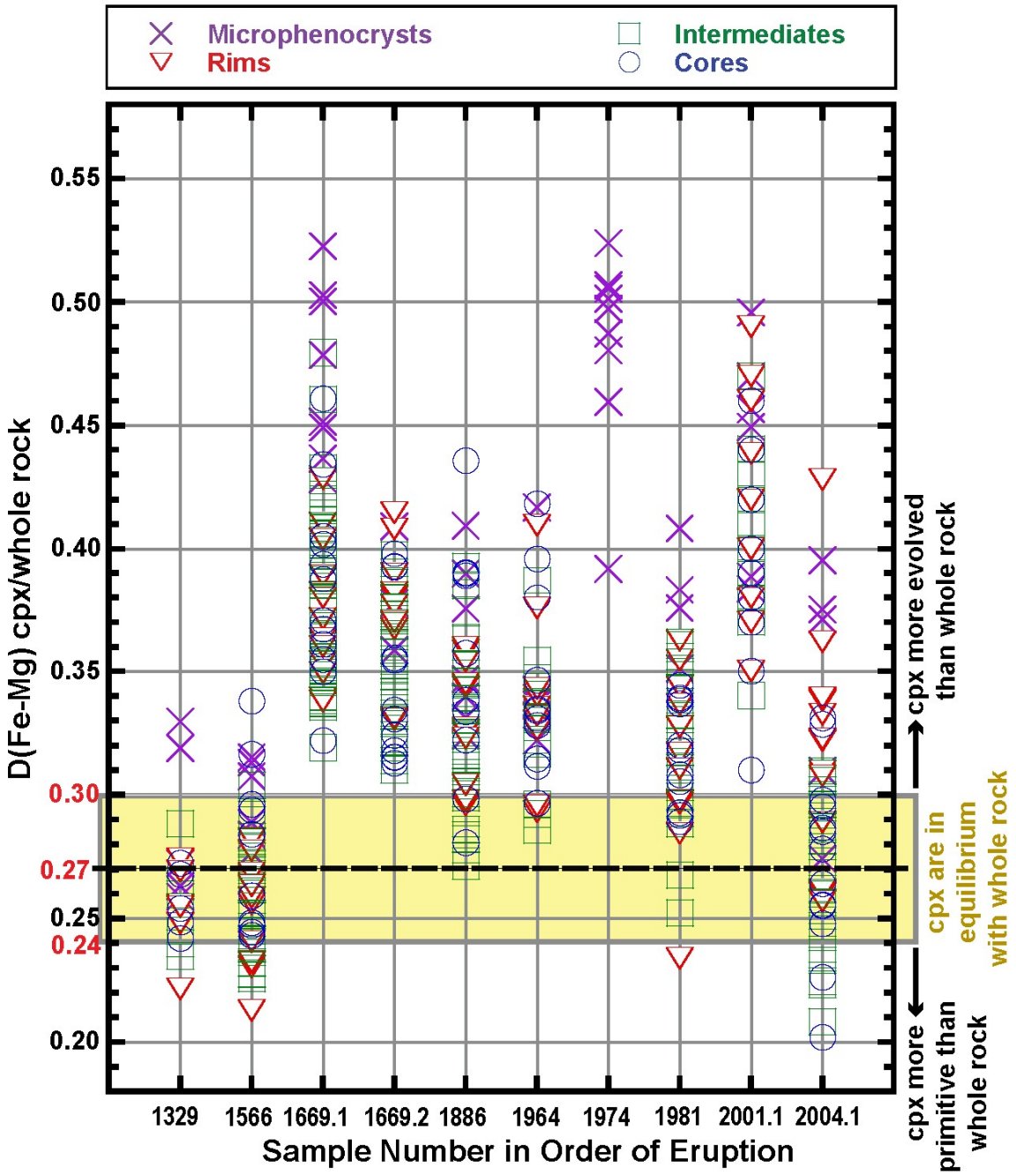

Figure 34. Sample number in order of eruption vs. D(Fe-Mg)$^{cpx/whole}$ rock. Observed whole rock MgO and FeO (wt. %) values evaluated with clinopyroxene MgO and FeO (wt. %) values. Equilibrium range of D(Fe-Mg)$^{cpx/whole\ rock}$ shown in yellow (0.27 ± 0.03), based on Putirka *et al.* (2008) and Armienti *et al.* (2012). See text for discussion.

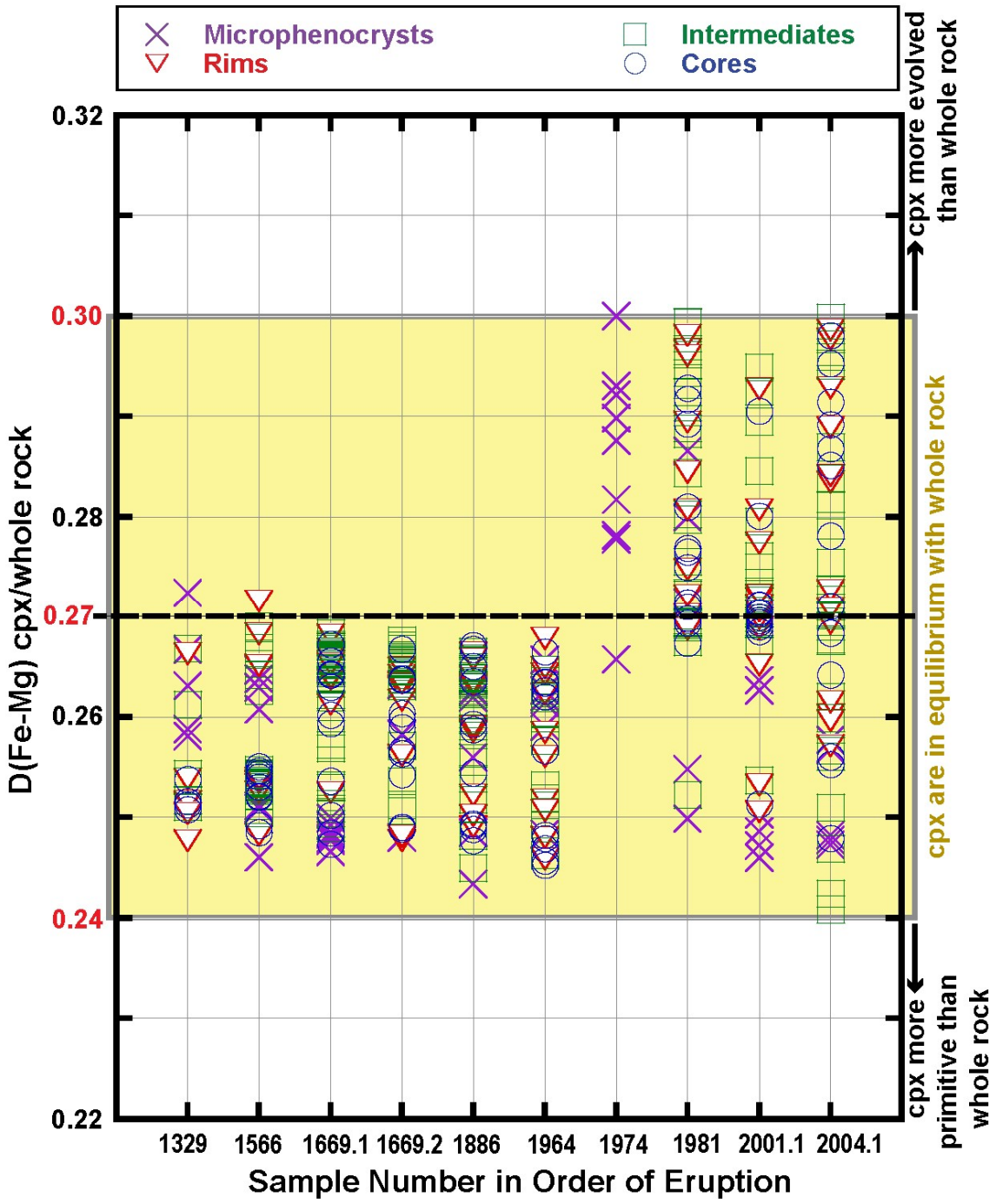

Figure 35. Sample number in order of eruption vs. $K_D(Fe\text{-}Mg)^{cpx\text{-}whole\ rock}$ evaluated for a reconstructed whole rock composition, in order to bring the crystals into equilibrium conditions at 0.27 ± 0.03. K_D calculated using whole rock values that achieve equilibrium with clinopyroxene analyses. Equilibrium range of $D(Fe\text{-}Mg)^{cpx/whole\ rock}$ shown in yellow (0.27 ± 0.03), based on Putirka *et al.* (2008) and Armienti *et al.* (2012). See text for discussion.

Evidence for Magma Recharge and Magma Mixing

Whole rock (Figures 5a, 32b and 33c) and clinopyroxene data support the importance of fractional crystallization in the Etna magmatic system. However, in addition to disequilibrium between Fe-Mg in whole rock and clinopyroxene, heterogeneity in whole rock and clinopyroxene $^{87}Sr/^{86}Sr$ data clearly demonstrate the operation of open-system processes, as well. In this section, I consider the role that magmatic recharge and mixing have played. The likely recurrence of recharge/mixing into Mt. Etna's magmatic system over the last 700 years is demonstrated by the variations in MgO vs. year (Figure 32b), including eruptions that exhibit increased whole rock MgO compared to previous eruptions (e.g., 1669 AD). The simplest interpretation of these observations is that intrusion of more mafic magma occurs episodically.

Furthermore, disequilibrium textures displayed in plagioclase (inclusion-rich envelops, boxy-cellular morphology, patchy zoning and embayment features and swallowtail features), in clinopyroxene (resorption features, particularly in 1669.1 and 1669.2 samples), rare inclusion-rich envelops, and complex sector and oscillatory zoning), and in olivine (skeletal morphologies and embayment features) may all be indicative of the injection of a hotter, more mafic melt from depth (Pitcher, 2011).

Consistent with these observations, an increase in Mg# along a core to rim profile of clinopyroxene may reflect a recharge event. For example, clinopyroxene 2001.1 D shows progressive increase in Mg#, exhibiting a core value of 72.5, two intermediate values which increase from 72.6 to 73.3 and a final rim value at 75.7 (see Table 8). Geobarometry results suggest the crystal grew isobarically (within error), with an average

pressure range of 4.9 ± 2 kbar. CaO concentration is tightly constrained for this crystal, barely fluctuating from 22.3, 22.1, 22.3, and 22.1 weight percent from core to rim, respectively. Core $^{87}Sr/^{86}Sr$ is 0.703596 ± 0.000018 is paired with a more radiogenic rim at 0.703747 ± 0.000017. The systematic increase in Mg#, coupled with a more radiogenic rim, suggests that if recharge is responsible, then the recharge melt/magma was more primitive and more radiogenic.

Viccaro and Cristofolini (2008) and Viccaro *et al.* (2010) performed systematic studies on historic (pre-1971) and recent (post-1971) lavas, documenting whole rock major and trace element and isotopic data and examining textural and compositional zoning (An% and FeO variations) in plagioclase phenocrysts. Based on textural variations, data trends and numerical modeling, pure fractional crystallization and crustal assimilation, in the absence of recharge, was determined to be insufficient in explaining variations in trace elements such as Rb and Th as well as $^{87}Sr/^{86}Sr$. They propose the partial melting and contribution of a heterogeneously metasomatized mantle yielded primitive, volatile-rich magmas that recharged various levels of the feeding system. Numerous other studies (Behncke and Neri, 2003; Correale *et al.*, 2014; Corsaro *et al.*, 2009; Ferlito *et al.*, 2008; Kahl *et al.*, 2013; Paonita *et al.*, 2012) conclude that recharge and mixing have been important.

Evidence for Crustal Assimilation of Limestone and Dolomite

Several observations of whole rock data trends suggest that crustal contamination may be operative, including year vs. K/Nb, Rb/Nb, and $^{87}Sr/^{86}Sr$ (Figure 36a-c) and MgO (wt. %) vs. K_2O and Rb (ppm) (Figures 32c, 33d). A critical examination of crustal

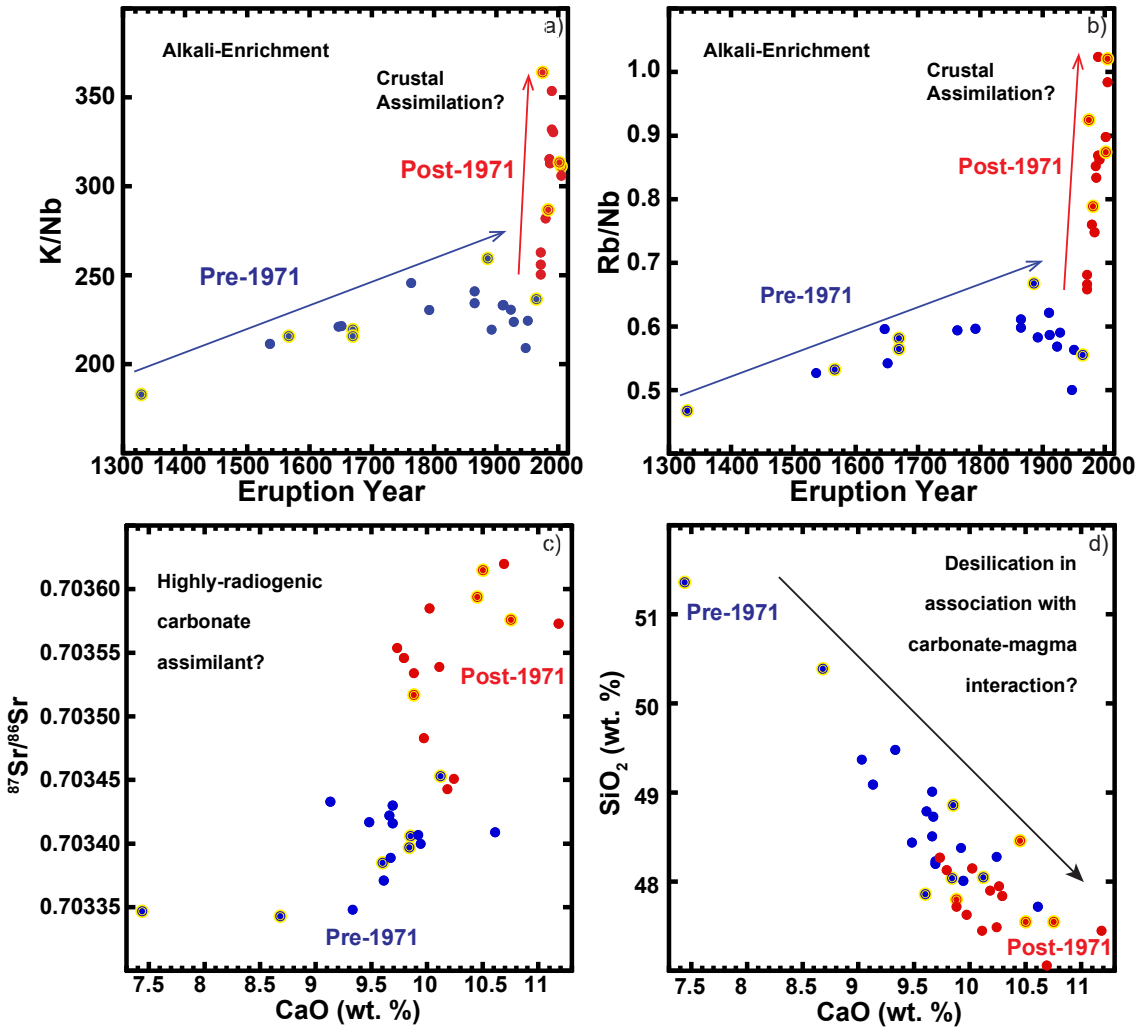

Figure 36a-d. Whole rock data plots for pre- and post-1971 samples: a) Year vs. K/Nb, b) CaO vs. Rb/Nb, c) CaO vs. $^{87}Sr/^{86}Sr$, d) CaO vs. SiO_2. Samples used in this study are highlighted in yellow.

assimilation with a particular emphasis on limestone and dolomite wall rock and basaltic magma interactions will be performed in the following sections. I will first review the scientific literature, which substantiates the existence of interactions between the basaltic magma and the sedimentary substratum at Mt. Etna, as well as scientific work detailing the effects of carbonate assimilation and basaltic magma within a volcanic system. *In situ* textural, geochemical, isotopic and geobarometric data from clinopyroxene will then be presented and explored in order bridge this information with my hypotheses regarding the occurrence of carbonate assimilation processes in the Etnean magmatic system.

Direct interaction of the magma and crustal wall rocks has been documented in crustal xenoliths during phreatomagmatic eruptions at Etna and in conditions accompanied by violent ascent of the magma in the volcanic conduits (Clocchiatti *et al.*, 1988; Michaud, 1995; Michaud *et al.*, 1988). These xenoliths, sampled at Etna, which include siliceous, peraluminous, carbonate and composite varieties, exhibit a wide range of petrologic and mineralogical features that reflect the heterogeneity of the crustal basement beneath Mt. Etna's edifice (Michaud, 1995).

The effects of magma-carbonate interaction on magma dynamics and evolution have been constrained by several recent experimental and petrological studies (Barnes *et al.*, 2005; Chadwick *et al.*, 2007; Coulson *et al.*, 2007; Freda *et al.*, 2008; Gaeta *et al.*, 2009; Iacono Marziano *et al.*, 2007a, 2007b; Wenzel *et al.*, 2002). Such magma contamination is documented to result in the abundant crystallization and overgrowth of CaO-rich phases, principally clinopyroxene, while the magma becomes progressively depleted in silica and enriched in alkalis. Release of CO_2 and Ca-rich fluids (Ague, 2003;

Barnes *et al.*, 2005; Freda *et al.*, 2008; Heap *et al.*, 2013; Iacono Marziano *et al.*, 2007a) is also hypothesized. Mollo *et al.* (2010) performed petrological magma-carbonate interaction experiments that revealed a three-phase process involved in the carbonate assimilation whose main products are: 1) clinopyroxene characterized by diopside-Ca-Tschermak solid solution, 2) silica-undersaturated CaO-Al_2O_3-rich melt, and 3) C-O-H fluid phase. However, rather than the direct ingestion of solid carbonate wall rocks, Gaeta *et al.* (2009) propose that such magma contamination may produce magmatic skarns at the magma-carbonate interface that act as a source of CaO-Al_2O_3-rich contaminant melt (Heap *et al.*, 2013).

Figures 31a-e (ΔCaO vs. ΔMg#) demonstrate that both pre- and post-1971 samples contain crystals which exhibit increased CaO along their core to rim profiles, with post-1971 demonstrating more significant increases in weight percent CaO. Formation of these higher CaO parts of crystals is consistent with predictions of carbonate assimilation, and the inferred placement of the Etna magmatic plumbing system within the carbonate platform of the Hyblean Foreland suggests that such magma-carbonate interaction at Etna is plausible. The dominance of the higher CaO crystals in post-1971 clinopyroxene and select pre-1971 clinopyroxene suggests that the degree of assimilation is greater in post-1971 magmas and that this assimilation may be systematically increasing with time. Additionally, as described in Chapter IV, a distinct population of high-CaO clinopyroxene (>22.5 wt. %) is observed in select 1886, 1981, 2001.1 and 2004.1 phenocrysts and select 1974 microphenocrysts. Figure 31c examines the distribution of this population of crystals in terms of ΔCaO vs. ΔMg# relationships.

Samples plot in all four quadrants, suggesting limestone assimilation in both the presence and absence of recharge and/or dolomite assimilation. This evidence suggests that multiple open-system processes are indeed operative, although recharge and carbonate assimilation are dominant.

Figure 23b-c and Figures 24 and 25 also offer compelling evidence for mid- to upper-crustal assimilation of the limestone/dolomite sequence in which the Etnean magmatic plumbing system is emplaced. This systematic increase in CaO with decreasing pressure (Figure 23b and Figure 25), observed in selected crystals from 1886, as well as post-1971 phenocrysts and microphenocrysts, strongly suggests direct interaction between the sedimentary strata and the magmatic system. Such geochemical enrichment along with decreasing pressures is also observed in the Mg# vs. pressure plot (Figure 24) for post-1971 phenocrysts and microphenocrysts. Increases in Mg# with decreasing pressure may signal assimilation of a dolomite component of the Hyblean Foreland Units. (It is also noted that although 1974 microphenocrysts have lower Mg# than the majority of phenocrysts in the study, most do increase in Mg # systematically with decreasing pressure.) Additionally, systematic increases in CaO, and to a lesser extent Mg# and Al_2O_3, in the crystals, is well aligned with the placement of the carbonate platform at ~5 kbar, or 15 km depth.

On a petrographic scale, the presence of plagioclase and clinopyroxene monomineralic glomerocrysts, may be interpreted to represent the entrainment of cumulate and/or conduit-wall crystals (Marsh, 2006). As presented in Tables 3 and 4, such glomerocrysts are abundant in all samples with the exception of sample 1974/1. An

interesting observation regarding clinopyroxene glomerocrysts includes clinopyroxene 1886 L, which is part of a large monomineralic glomerocryst and possesses an anomalously high $^{87}Sr/^{86}Sr$ value (0.710150 ± 0.000119), a signature that could be related to the carbonate substratum beneath Mt. Etna. This may hold implications for magmatic skarn formation, in which magma/carbonate interaction results in associated contact metamorphism and metasomatism of the wall rock, thereby producing fluids and mineralization (Meinert, 1992). Such interactions, among with other anomalously high $^{87}Sr/^{86}Sr$ clinopyroxene (i.e. 1329 B and 2004.1 A), will be discussed in greater detail below.

It is also important to consider that there are two potential and distinct sources of Mg# increases displayed within the clinopyroxene: the dolomite wall rock, and more mafic recharge magma from a mantle source. Such a characterization cannot be made merely by the major element geochemistry, but may be derived by examining the $^{87}Sr/^{86}Sr$ data. Values ranging from ~0.70336 to ~0.70385 cannot be excluded from the contribution of a mantle recharge component, while higher levels of $^{87}Sr/^{86}Sr$ are inferred to represent the addition of a crustal component and potentially a carbonate assimilation signature. Therefore, these crystals residing at the more elevated Sr isotope levels and displaying a concomitant increase in Mg#, are interpreted to represent the incorporation of the dolomite component at that stage in their growth history.

Evidence for Dynamic RAFC Processes

Complexity among whole rock data (Figures 32a-d, 33a-e, 36a-d) suggests the occurrence of multiple processes of recharge, assimilation and fractional crystallization

processes operating within the Etnean magmatic regime. Similarly, Figure 31e illustrates the complex distribution of RAFC pathways among clinopyroxene in each sample; clinopyroxene crystal populations express much heterogeneity, lacking consistent core to rim trends in components such as Mg#, CaO (Figure 31a-d), pressures and $^{87}Sr/^{86}Sr$ values. This lack of strictly systematic relationships in clinopyroxene implies complex crystallization environments and RAFC processes that make variable contributions in space and time.

Clinopyroxene data presented here indeed bears evidence for polygenetic histories, in which each crystal records multiple events during its growth as it resides within the crystallization environment. Figures 34 and 35 reflect the wide range of melt compositions in which the clinopyroxene resided and evolved. Figures 31a-e (ΔCaO vs. ΔMg#) further demonstrate the contribution of multiple magma dynamics of recharge, assimilation and fractional crystallization process (RAFC), as well as the combined interactions of carbonate assimilation and recharge among crystal populations.

In order to provide examples of the dynamic processes inferred to coexist within the magmatic plumbing system, three crystals, which demonstrate particularly diverse and intriguing petrogenetic histories, will be explored in greater detail: a) 1669.1 B, b) 1981 D and c) 2004.1 A (Figures 37a-d, Tables 7 and 8). These crystals represent an array of RAFC processes that occur within the subvolcanic plumbing system over time and space. Textural features, geochemical components (Mg# and wt. % CaO and Na_2O), geobarometry and $^{87}Sr/^{86}Sr$ values are examined.

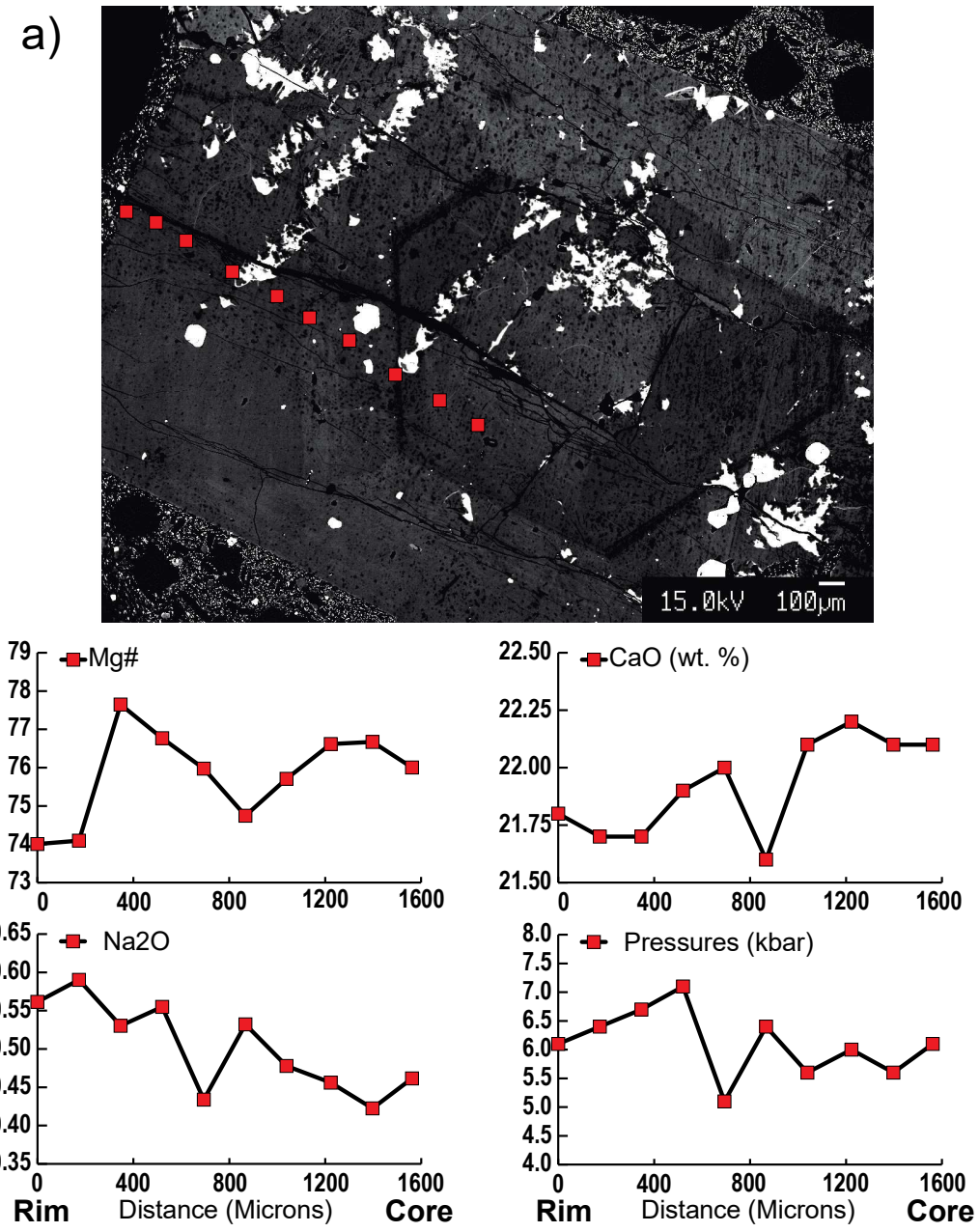

Figure 37a. Clinopyroxene profiles demonstrating petrogenetic history. Clinopyroxene 1669.1 B, displaying select textural, geochemical, and geobarometric information: core-to-rim transects of Mg#, CaO, Na_2O, and calculated pressures (kbar). Red squares are locations of electron microprobe analyses. All oxides are reported in weight percent. Pressure errors are ± 2 kbar.

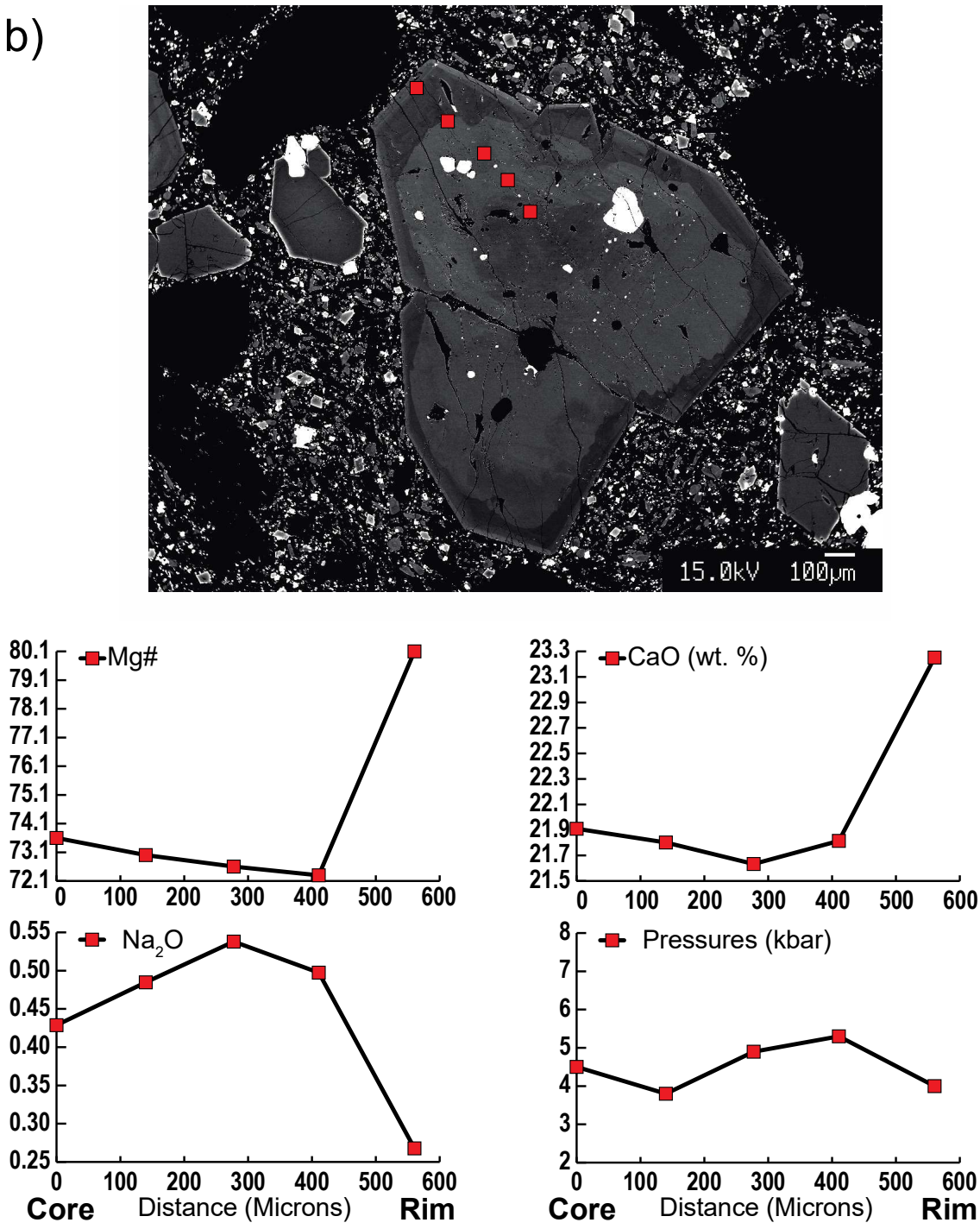

Figure 37b. Clinopyroxene profiles demonstrating petrogenetic history. Clinopyroxene 1981 D, displaying select textural, geochemical, and geobarometric information: core-to-rim transects of Mg#, CaO, Na_2O, and calculated pressures (kbar). Red squares are locations of electron microprobe analyses. All oxides are reported in weight percent. Pressure errors are ± 2 kbar.

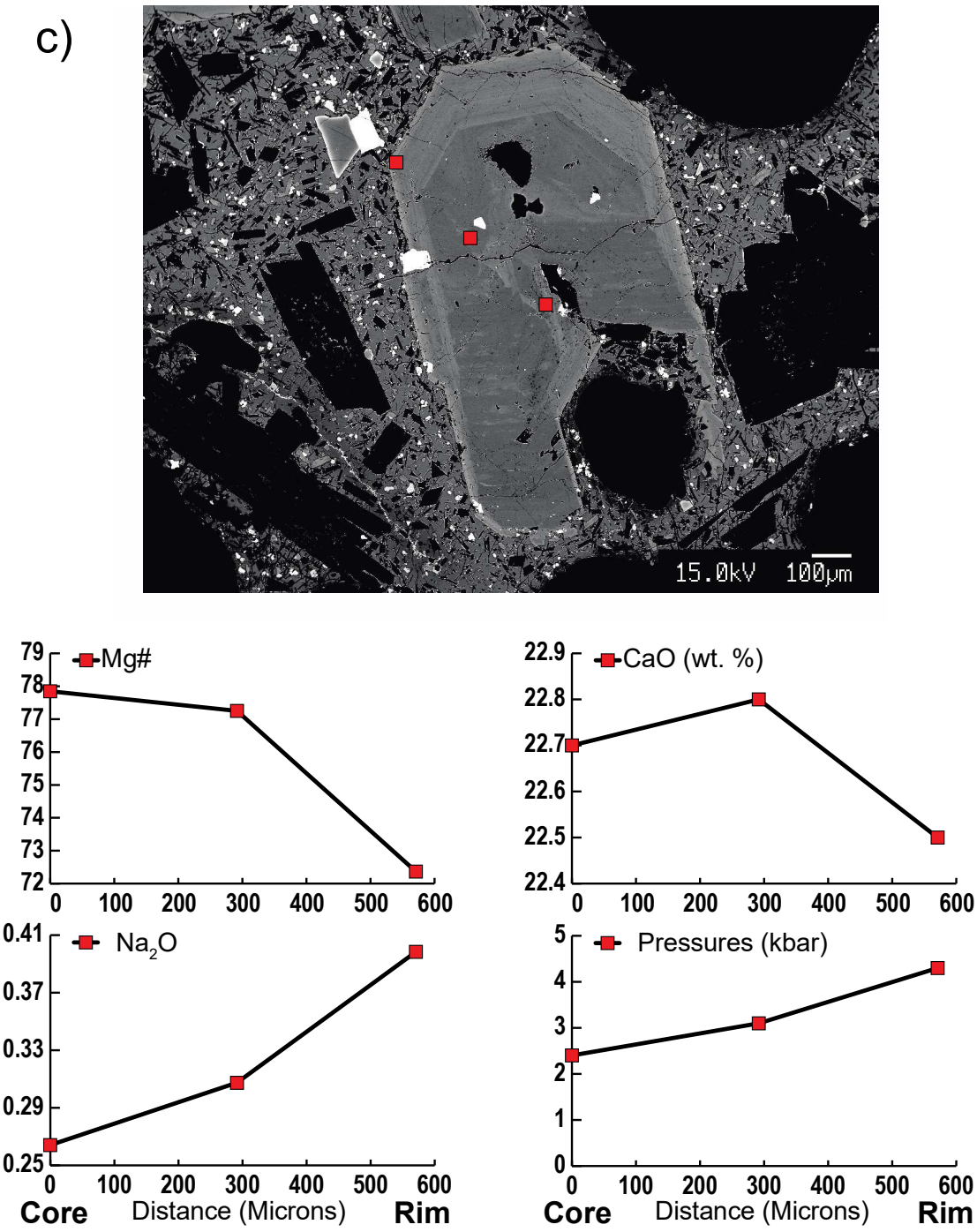

Figure 37c. Clinopyroxene profiles demonstrating petrogenetic history. Clinopyroxene 2004.1 A, displaying select textural, geochemical, and geobarometric information: core-to-rim transects of Mg#, CaO, Na_2O, and calculated pressures (kbar). Red squares are locations of electron microprobe analyses. All oxides are reported in weight percent. Pressure errors are ± 2 kbar.

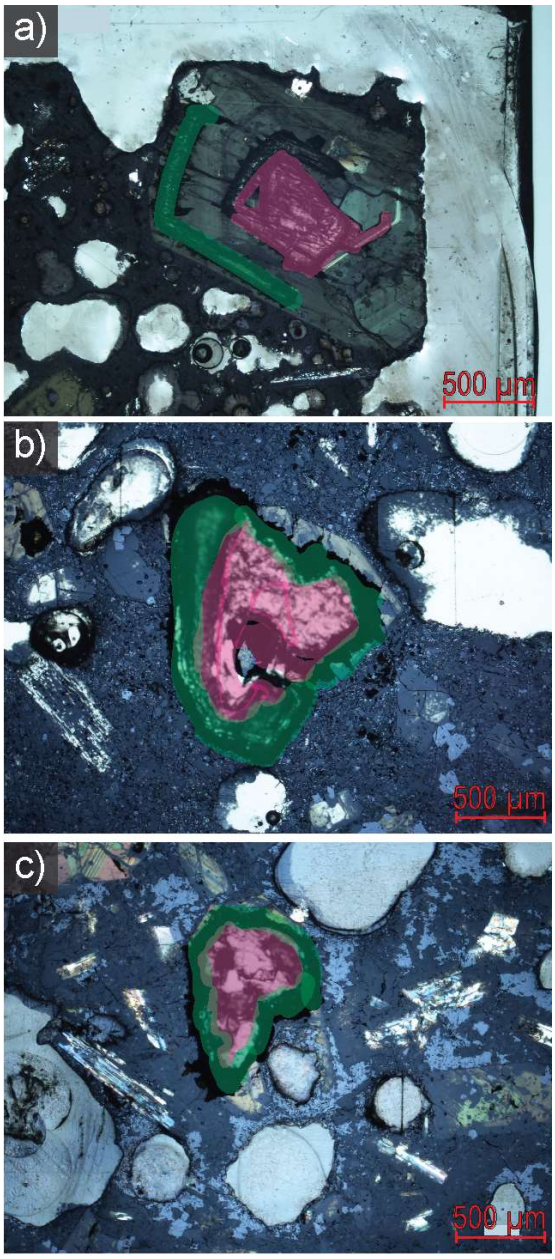

a) Clinopyroxene 1669.1 B:
$^{87}Sr/^{86}Sr$ values:
Core: 0.703383 ± 2.00E-05
Rim: 0.703465 ± 2.10E-05

b) Clinopyroxene 1981 D:
$^{87}Sr/^{86}Sr$ values:
Core: 0.703451 ± 2.00E-05
Rim: 0.704298 ± 1.80E-05

c) Clinopyroxene 2004.1 A:
$^{87}Sr/^{86}Sr$ values:
Core: 0.710207 ± 6.30E-05
Rim: 0.705389 ± 2.30E-05

Figure 37d. Clinopyroxene profiles demonstrating petrogenetic history. $^{87}Sr/^{86}Sr$ values for microsampled cores of rims of clinopyroxene samples: a) 1669.1 B, b) 1981 D, c) 2004.1 A. Green region of crystal drilled and defined as rim; pink region drilled and defined as core for Sr isotope analyses.

Corsaro *et al.* (1996) describes the 1669 eruption of Mt. Etna to be historically unique, due to the large volume of lava erupted (500-1000 x 10^6 m^3, Wadge, 1977) and a

high average effusion rate of 50-100 m^3/s. Based upon petrochemical data, they interpret this eruption to have been triggered by the injection of a hot, volatile-rich, mafic magma into a reservoir containing a more evolved and volatile-poor magma. They conclude that these contrasting conditions caused the former to buoyantly rise through the existing reservoir, thereby inducing eruption. This eruption continued for approximately two months, producing the longest lava field (~17 km) in recent times and causing widespread damage, including the partial destruction of the city of Catania. Additionally, this eruption is significant as it is proposed to have significantly altered the magmatic plumbing system (Hughes *et al.*, 1990; Wadge *et al.*, 1975), the implications of which will be discussed in the final section of this Chapter.

Clinopyroxene 1669.1 B (Figure 37a,d) is the largest crystal (longest dimension 2.5 millimeters) of those analyzed. Overall, strong oscillatory zoning is displayed throughout the entire crystal and all calculated pressures along its core to rim profile are within ± 2 kbar error (5-7 kbar). CaO is more enriched in the core than the rim, while expressing variation throughout the crystal transect. Mg# also expresses variation, with a core more enriched than the rim, as well as internal variations. Those internal variations which show increase in the Mg# may reflect the injection of the mafic recharge magma, as proposed by Corsaro *et al.* (1996). The more evolved rim may also reflect fractional crystallization, in which the last portion of the crystal grew within a more evolved melt. The $^{87}Sr/^{86}Sr$ values indicate enrichment in the rim relative to the core, therefore suggesting that the recharge magma delivered a higher $^{87}Sr/^{86}Sr$ signature into the system, as well.

Clinopyroxene 1981 D (Figure 37b,d) bears strong evidence for a complex petrogenetic history: implying the potential assimilation of limestone and dolomite components and fractional crystallization, along with possible recharge, at pressures of approximately 4-5 ± 2.0 kbar, 12-15 ± 6.0 km. Texturally, this crystal exhibits patchy and oscillatory zoning in its interior, as well as a distinct resorption texture toward its outer edge. Its rim demonstrates clear oscillatory zoning and the crystal has some euhedral edges and some embayment features, all attesting to an intricate petrochemical history. Both CaO and Mg# are high in the cores, and progressively decrease along the core to rim profile of the crystal, indicating fractional crystallization. The rim, however, shows dramatic enrichment in both CaO at 23.3 weight percent and Mg# at 80.1. This is mirrored by a dramatic increase in radiogenic Sr, with $^{87}Sr/^{86}Sr$ values from core values of 0.703451 ± 0.000020 to a 0.704298 ± 0.000018 in the rim. These geochemical and isotopic signatures likely reveal the late-stage assimilation of the carbonate (limestone and/or dolomite) wall rock. Elevated Mg# values, along with the resorption feature, is also a strong indicator for the additional influence of magma recharge into the system.

Clinopyroxene 2004.1 A (Figure 37c,d) is a particularly compelling sample, as it represents the most highly radiogenic microsampled crystal of the entire dataset, with a core at 0.710207 ± 0.000063 and a rim at 0.705389 ± 0.000023. Geobarometry results suggest the crystal grew isobarically, within error (2-4 kbar). Geochemically, the core and single intermediate point are fairly enriched in CaO and Mg#, while the rim shows a decrease in CaO and a fairly dramatic drop in Mg#, from 77.8 and 77.3, to 72.4. Such a highly radiogenic, CaO- and Mg#-rich core may indicate that this portion of the crystal is

xenocrystic. The abundant presence of high temperature, calcic skarn xenoliths, which include clinopyroxene, have been documented as evidence for carbonate assimilation/contamination at the Alban Hills Volcano of Central Italy (Federico *et al.*, 1994; Iacono Marziano *et al.*, 2007b; Peccerillo, 2005), while petrological and experimental studies (Di Rocco *et al.*, 2012; Gaeta *et al.*, 2009; Mollo *et al.*, 2010) describe the formation of clinopyroxene with high Ca-Tschermak activity. Thus clinopyroxene 2004.1 A may be evidence of magma-carbonate interaction and skarn formation.

Furthermore, at Mt. Etna, Michaud (1995) documents the presence of thermally altered crustal xenoliths, including carbonate xenoliths containing calcium-rich clinopyroxene. Clinopyroxene 2004.1 A's intriguing textural, geochemical, and isotopic features may indicate the following magmatic history: the clinopyroxene was first inherited by the magma from the related magmatic skarn; as the crystal was introduced to the magmatic environment, it began to re-equilibrate. Finally, as its rim grew, it began to reflect the more evolved, less radiogenic magma batch into which it had been introduced. Similar geochemical patterns are also observed in 1329 B and 1886 L, as well, and all three of these clinopyroxenes lie within error of the same pressures and location in the Etna magmatic plumbing system (Figure 27d).

Constraints for the Source and Timing of Alkali-Enrichment

As displayed in Figures 32d, 33e, 36a and 36b and described in Chapter II, enrichment in select alkali elements and $^{87}Sr/^{86}Sr$ ratios is displayed in Mt. Etna's erupted products from 1329 to 1971, followed by a dramatic increase in these components, post-1971. The primary debate regarding this alkali-enrichment is whether its source is related to changes in the mantle (Armienti *et al.*, 1989; Doglioni *et al.*, 2001; Gvirtzman and Nur, 1999; Métrich *et al.*, 2004; Schiano *et al.*, 2001; Tonarini *et al.*, 2001; Viccaro *et al.*, 2010), or to shallow crustal assimilation (Chiodini *et al.*, 2011; Clocchiatti *et al.*, 1988; Condomines *et al.*, 1995; Heap *et al.*, 2013; Michaud and Clocchiatti, 1994; Michaud, 1991, 1995; Michaud *et al.*, 1988; Pitcher, 2011; Villemant *et al.*, 1993).

In the previous sections, whole rock and clinopyroxene data from 1329 to 2004 AD characterize the petrogenetic history recorded in pre-1971 and post-1971 samples. These data demonstrate the dominance of fractional crystallization, crustal assimilation (with particular emphasis on carbonate/dolomite assimilation), recharge and mixing processes within a highly dynamic magmatic system. Here, I propose that the alkali-enrichment at Mt. Etna, Sicily is primarily related to late-stage, upper crustal assimilation due to interaction of basaltic magma and the carbonate substratum of the Hyblean Plateau. Furthermore, I propose that increased rates of mantle recharge may further enhance carbonate assimilation process, thereby influencing the alkali-enrichment process, as well.

As discussed in Chapter IV, many pre-1971, and all (excluding 2004.1 A) post-1971 samples rims are more enriched in $^{87}Sr/^{86}Sr$ than their corresponding cores. Cores are typically ~0.70336 to 0.70385 (Group 1, Figure 27a) and rims are in the range

~0.70386 to 0.70550 (Group 2, 27a), excluding Group 3 samples. This core to rim change indicates that radiogenic Sr was added as the crystals grew. This observation, together with the strong correlation between whole rock Sr isotope ratios and K/Nb suggests that the alkali-enrichment is late-stage. Additionally, the very radiogenic values, up to as high as 0.710207 ± 0.000063 (Group 3, Figure 27a), expressed in some crystals are unlikely to represent a mantle signature. These very radiogenic clinopyroxene, as described in previous sections, are interpreted as xenocrystic and inherited from the wall rock, with an origin from magmatic skarn. All anomalously high $^{87}Sr/^{86}Sr$ clinopyroxene of Group 3 are also represented by cores, paired with rims that are much less radiogenic, and all record pressures at 3-5 ± 2 kbar (Figure 27d), a location that is consistent with the carbonate volcanic substratum as well as the high-velocity anomaly as recorded by (Chiarabba *et al.*, 2000), a seismological signature which may potential indicate the presence of a magmatic skarn.

According to Mollo *et al.* (2009) and references therein, the primary effect of basaltic magma-carbonate interaction is the formation of a silica-undersaturated, alkali-rich residual melt. This resultant melt is associated with the dissolution of $CaCO_3$ in the melt by the consumption of SiO_2 and MgO to form diopside, in the following reaction from Marziano (2007 a and b):

$$CaCO_3 \text{ (solid)} + SiO_2 \text{ (melt)} + MgO \text{ (melt)} \rightarrow \text{Diopside (solid)} + CO_2 \text{ (fluid)}$$

Thus, this implies that MgO content, and therefore, magmatic recharge, potentially represents a control on the extent of carbonate assimilation. The assimilation of dolomite may also supply the MgO for this reaction, as well. From 1329 to 2004,

whole rock weight percent SiO_2 (Figure 38d) demonstrates a general decrease with many fluctuations, which is consistent with processes of desilication. Decreasing silica in pre- and post-1971 samples (Figures 38a-c) correlates with indicators of alkali-enrichment such as K/Nb and Rb/Nb, suggesting decreases in silica and addition of alkali elements are at least partly a consequence of crustal contamination. Figure 36d illustrates that whole rocks exhibit a concomitant increase in CaO (wt. %) and $^{87}Sr/^{86}Sr$ from pre- to post-1971; thus, the increase in CaO may be tied to the alkali-enrichment signature in the magmas.

Experimental and petrologic studies, such as Barnes *et al.* (2005) and Marziano *et al.* (2007a and b), demonstrate that in the presence of a hot, mafic and volatile-rich melt, carbonate assimilation may be most efficiently induced. It is therefore reasonable to infer that mantle recharge itself may trigger the contamination and incorporation of limestone and dolomite wall rock by delivering heat. According to experiments performed by Heap *et al.* (2009, 2013), the high temperatures induced by magmatism within the deep carbonate basement have the potential to critically weaken and alter the wall rock, producing a) increased deformation due to instability, and b) increased CO_2 degassing as a result of the carbonate-basaltic magma interaction (Chiodini *et al.*, 2011; Frezzotti *et al.*, 2009; Heap *et al.*, 2009, 2013); both features are demonstrably increased at Mt. Etna since 1971 (Kamenetsky *et al.*, 2007; Tanguy *et al.*, 1997; Viccaro *et al.*, 2010) and thus coincide with the dramatic alkali-enrichment signature. Additionally, Heap *et al.* (2013) propose that the establishment of peripheral reservoirs and eccentric dikes through the Hyblean Plateau may potentially introduce hot basaltic magma to fresh, unaltered

carbonate rock, promoting enhanced carbonate assimilation. Therefore, a carbonate assimilation signature may indeed overprint the contribution of a mantle recharge signature within the magma system; as demonstrated by the textural, geochemical and isotopic features of clinopyroxene 1981 D (Figure 37b,d) there is direct crystal evidence that such dynamics are indeed at work within the Etnean magmatic system.

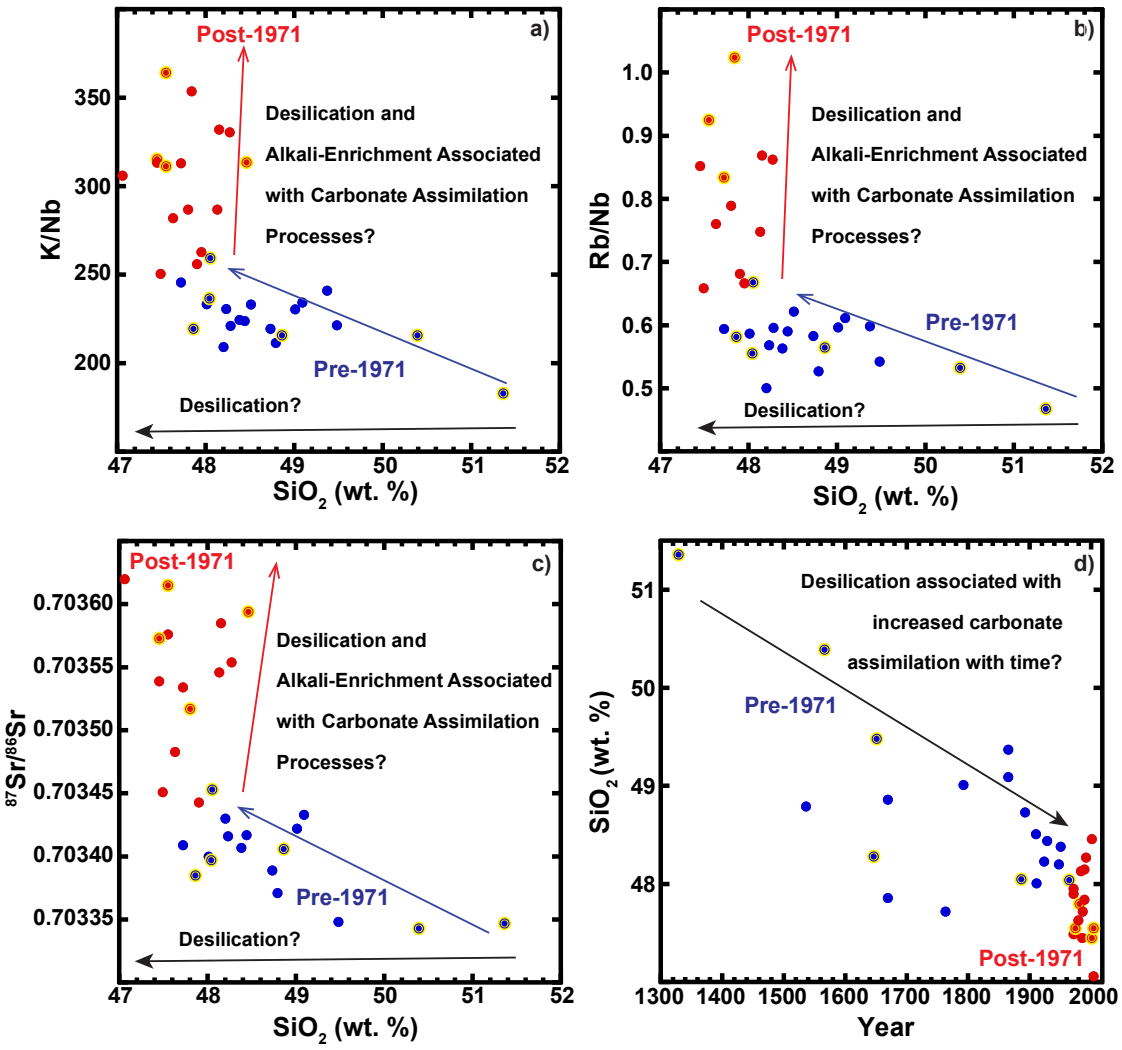

Figure 38a-d. Whole rock data plots for pre- and post-1971 samples, examining relationships with SiO_2 depletion with the alkali-enrichment signature, and from 1329-2004 AD: a) SiO_2 vs. K/Nb, b) SiO_2 vs. Rb/Nb, c) SiO_2 vs. $^{87}Sr/^{86}Sr$, d) Year vs. SiO_2. Samples used in this study are highlighted in yellow.

In summary, due to the potential influence of mantle recharge on carbonate assimilation processes, the mantle recharge component, as described by Armienti *et al.* (2012) and Gvirtzman and Nur (1999), may contribute to the observed enrichment in select alkalis and $^{87}Sr/^{86}Sr$. Thus, although carbonate assimilation may be the primary contributor of the alkali-enrichment signature, magmatic recharge may potentially have a secondary role in contributing distinct geochemical and isotopic compositions into the system. Computational modeling can further test these hypotheses regarding the roles of recharge and carbonate assimilation, allowing us to resolve better the source and timing of alkali-enrichment within the Etnean magmatic system.

There may also be evidence for late-stage upper crustal assimilation involving the upper portions of the volcanic substratum and the allochthonous flyschoid series overlying the carbonate sedimentary basement. The documentation of crustal siliceous and peraluminous xenoliths by Michaud (1995) and Clocchiatti *et al.* (1988) support the concept of magmatic interaction with these shallower sedimentary units, and clinopyroxene geobarometry suggests crystallization at depths (~4.5 km, 1.5 kbar, Catalano *et al.*, 2004; Heap *et al.*, 2013) where these units are located.

Magmatic Storage and Transport System

In previous sections, I have documented constraints on the locations of clinopyroxene crystallization, and discussed evidence for RAFC. Additionally, I have hypothesized that the observed alkali-enrichment in volcanic products over the last 700 years is related to carbonate assimilation/contamination, with the potential influence of magmatic recharge, as well. I will now apply this information to the broader context of

Mt. Etna's magmatic storage and transport system. I will first examine the evolution of thought within volcanology itself in the modeling of magmatic systems. I will then revisit several relationships among the *in situ* clinopyroxene data and their implications regarding the nature and evolution of Mt. Etna's magmatic storage and transport system. Finally, I will reconstruct the Etnean magmatic plumbing system from pre- to post-1971, integrating scientific literature as well as my observations and interpretations regarding the shifts in geochemical, isotopic and eruptive behavior throughout the last 700 years of volcanic history.

A major pursuit in volcanology is documenting the location, size and structure of the subvolcanic magma storage and transport zone. A textbook model of a typical volcanic plumbing system might include a single, simple magma chamber connected to the surface via a volcanic conduit. But magma bodies may be portrayed as complex structures consisting of an intricate system of dikes, sills and irregularly-shaped chambers or pockets that can extend through the crust (Cartwright and Møller Hansen, 2006; Dawson, 2004; Marsh, 2004; Paonita *et al.*, 2012; Paulatto *et al.*, 2010; Preston, 2001; Thomson, 2004; Zellmer and Annen, 2008). The structure and geometry of these bodies regulate the extent of magma migration as well as hydraulic connectivity and continuity throughout the system, resulting in conditions that promote the mixing and interaction of magma and magmatic fluids among different levels of the plumbing system prior to eruption (Edmonds *et al.*, 2010; Paonita *et al.*, 2012).

Several researchers characterize the recent plumbing system of Mt. Etna as a complex network of interconnected feeding-dikes and sills (Aloisi *et al.*, 2009; Chiarabba

et al., 2000; Cristofolini *et al.*, 1987; De Gori *et al.*, 2005; Guest and Duncan, 1981; Hirn *et al.*, 1997; Patanè *et al.*, 2011; Rollin *et al.*, 2000; Romano, 1983; Romano *et al.*, 1979). Within the 1329 to 2004 sample suite, each documented clinopyroxene crystal possesses a unique petrogenetic history. Indeed, complexity in petrographic, compositional, geobarometric and isotopic features is prevalent not only within a single sample, but within a single crystal, holding implications for crystallization within an expansive framework of magmatic dikes and sills as described by Corsaro and Pompilio (2000) and Corsaro *et al.* (2006).

As described in Chapter IV, clinopyroxenes are texturally complex in all samples, often with multiple textures represented in a single lava sample; this may be consistent with the mixing and interaction of magma among multiple levels of the plumbing system as described by Edmonds *et al.* (2010) and Paonita *et al.* (2012). Additionally, it is observed that phenocrysts and microphenocrysts of pre- and post-1971 samples display geochemical heterogeneity throughout the last 700 years of volcanic history coupled with both normal and reverse zoning in Mg#, CaO and other geochemical constituents. Sr isotope relationships also exhibit a very broad range of values, with the majority of clinopyroxene cores and rims demonstrating higher $^{87}Sr/^{86}Sr$ than their corresponding whole rock. Exchanges and mixing between distinct magma batches may be responsible for introducing such heterogeneity to the clinopyroxene populations, supporting a complex and dynamic crystallization and growth environment.

The Fe-Mg exchange between clinopyroxene and the whole rock (Figure 34), demonstrates $D(Fe\text{-}Mg)^{cpx/whole\ rock}$ values above, below and within equilibrium (0.27 ±

0.03), indicating that clinopyroxene grew within a wide range of melt compositions. The observed variation from sample to sample represents the presence mixed crystal populations, which have undergone complex RAFC processes. However, many samples also exhibit overlap in D(Fe-Mg) $^{\text{cpx/whole rock values}}$: 1329, 1566 and 2004.1, as well as 1669.1, 1669.2, 1886, 1964 and 1981 in particular. Similarly, although Figure 15 demonstrates a wide range of whole rock MgO values, all samples share a similar and constrained range of clinopyroxene Mg# values. Such commonality among crystal populations may indicate the operation of antecrystic 'sharing', or 'communication' among the magmas throughout their history, marked by interaction within an open-system, dynamic regime of crystal growth. Ultimately, the heterogeneous nature described above is displayed in all samples, and therefore may imply that complex RAFC processing within the magmatic system is maintained throughout Mt. Etna's history from 1329-2004 AD. In summary, the complex petrogenetic histories observed in each individual clinopyroxene crystal represent intricate geochemical pathways coexisting within a dynamic system, and are further evidence for crystallization within an expansive framework of magmatic dikes and sills.

Reconstructing the Etnean Magmatic Plumbing System from Pre-1971 to Post-1971

According to Guest and Duncan (1981) and Duncan and Guest (1982), due to factors such as fluctuations in the regional stress pattern, changes in the rate and volume of magma supply, and variations in local stress conditions within the magma source region, the size, geometry and connectivity of the magmatic system has fluctuated, both spatially and temporally throughout its history. 700 years of whole rock and *in situ*

clinopyroxene data illustrate these variations, particularly with respect to the geochemical and isotopic distinctions among pre- and post-1971 samples.

As discussed in Corsaro *et al.* (1996) and previously in this Chapter, the 1669 eruption of Mt. Etna was highly voluminous and destructive, and is proposed to have also introduced significant changes (size, geometry and connectivity) to the subvolcanic plumbing system (Hughes *et al.*, 1990; Wadge *et al.*, 1975). This interpretation is based upon a period of exceedingly low volcanic activity for 60 years, following the 1669 eruption. After this relatively quiescent period, a dramatic increase in the mean effusion rate was recorded, as well as an exponential increase in explosive activity at Mt Etna, both trends of which have continued to present day (Branca and Del Carlo, 2004, 2005; Clocchiatti *et al.*, 1988; Corsaro *et al.*, 1996; Mulargia *et al.*, 1987; Romano *et al.*, 1979). A mean effusive rate of 0.02 m^3/s initiated post-1669 and persisted until the mid-18^{th} century. From the mid-18^{th} century until 1971, the mean effusive rate increased to 0.2 m^3/s, followed by a further increase to 0.51 m^3/s, post-1971 (Branca and Del Carlo, 2004, 2005; Wadge and Guest, 1981).

This concept of a collapse and 'resetting' of the Etnean magmatic plumbing system as inferred by Wadge *et al.* (1975) and Hughes *et al.* (1990), as well as the increase in the mean effusion rates and exponential increase in explosivity post-1669, correlates well with the evidence and interpretation of an increasing influence of recharge-induced carbonate assimilation from pre- to post-1971. This interpretation may also help further explain the shifts in both geochemical and eruptive behavior observed at Mt. Etna over the last 700 years. Such a rearrangement of the system was a potential

mechanism to expose fresh, unaltered carbonate at the depths of the Hyblean Plateau.

Furthermore, an increased pulse of magmatic recharge, as inferred by the increased rate of effusion from pre- to post-1971, could further promote carbonate wall rock assimilation, as described by Heap *et al.* (2009, 2013). Pre-1971 samples indeed demonstrate evidence for carbonate assimilation ± recharge, as represented by Figures 31a and 31e, as well as the elevated Sr isotope values observed in the 1329, 1566 and 1886 clinopyroxene. Additionally, the high-CaO clinopyroxene (>wt. % 22.5) observed in sample 1886 further support the interpretation that changes in the structure of the magmatic plumbing system, post-1669, allowed for the increased influence of carbonate assimilation ± recharge. As effusion rates and eruption frequency further increased, post-1971, this expression of carbonate assimilation ± recharge potentially increased as well, as documented in this study.

Here, I present two schematic diagrams of Mt. Etna's subvolcanic plumbing system, summarizing the observations and interpretations of this study by providing a reconstruction of the Etnean magma storage and transport system from 1329-1971 AD (pre-1971, Figure 39) and 1971-2004 AD (post-1971, Figure 40). I also relate the evolution the magmatic system from pre- to post-1971 to the gradual and dramatic shifts in geochemical, isotopic and eruptive behavior that have been observed in the last 700 years at Mt. Etna. Recall that throughout this period, clinopyroxene crystallization is recorded from 0-7 ± 2 kbar (surface-21 km ± 6 km, Figure 21), consistent with previous studies (Armienti, 2004; Armienti *et al.*, 2007; Ghiorso, 2002; Moses, 2010; Trigila *et al.*, 1990). In addition a dominant crystallization zone is recorded at ~2.9-5.5 kbar (~8.7-16.5

km, Figure 22), consistent with measured depths of cumulate/magma storage zones, (3-18 km, Chiarabba *et al.*, 2000) as well as the carbonate substratum of the Hyblean Plateau beneath Mt. Etna (5-15 km, Heap *et al.*, 2013b). These estimated pressure ranges and magmatic storage zones are thus represented in Figures 39 and 40, as a plexus of dikes and sills.

The pre-1971 Etnean magma and transport system (Figure 39) is represented by well-established magmatic reservoirs, with geochemical pathways of magmatic recharge and fractional crystallization dominating the system. Evidence for minor carbonate assimilation is also demonstrated in elevated clinopyroxene Sr isotope values observed in samples 1329, 1566 and 1886 (Figure 27a). Additionally, the anomolously-high Sr isotope values of clinopyroxene 1329 B and 1886 L (Table 7) are interpreted as potential skarn xenocrysts. Sample 1886 also contains clinopyroxene among the high CaO (>weight % 22.5) population, which exhibit increasing CaO values with decreasing pressures (Figures 23b and 25). In addition, the 1669 eruption potentially resulted in changes of the subvolcanic plumbing system (Hughes *et al.*, 1990; Wadge *et al.*, 1975) that contribute to an increased influence of the carbonate assimilation signature, as expressed in sample 1886 and eventually, post-1971 samples. The post-1971 Etnean magma and transport system (Figure 40) is dominated by this carbonate assimilation signature, with strong evidence that this process is enhanced by recharge. Figure 41 summarizes the implications of these processes, as well as the final interpretations of this study in regard to Mt. Etna's dramatic shift in geochemical and eruptive behavior throughout 700 years of volcanic history.

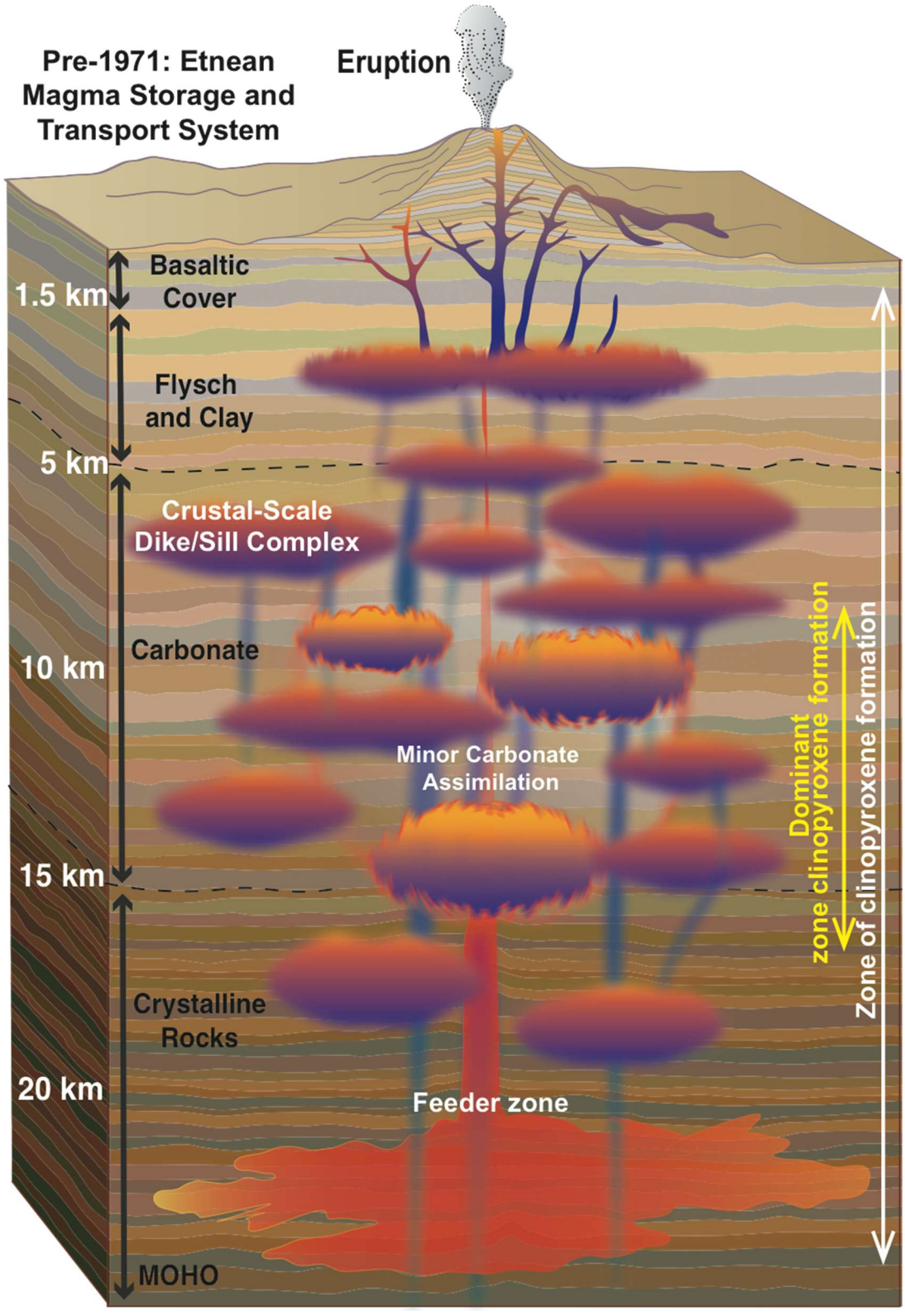

Figure 39. Schematic diagram of pre-1971 Etnean magma storage and transport system.

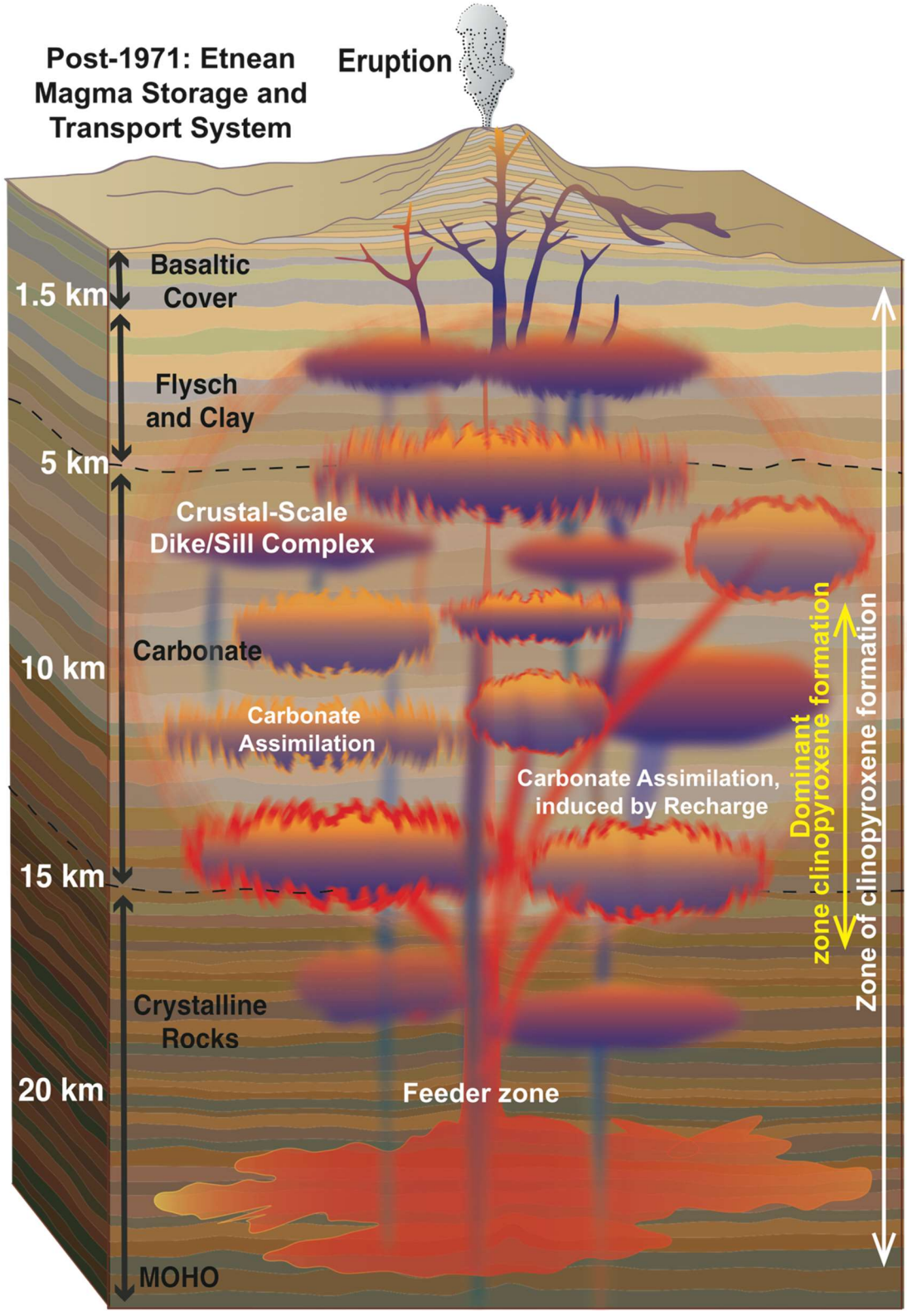

Figure 40. Schematic diagram of post-1971 Etnean magma storage and transport system.

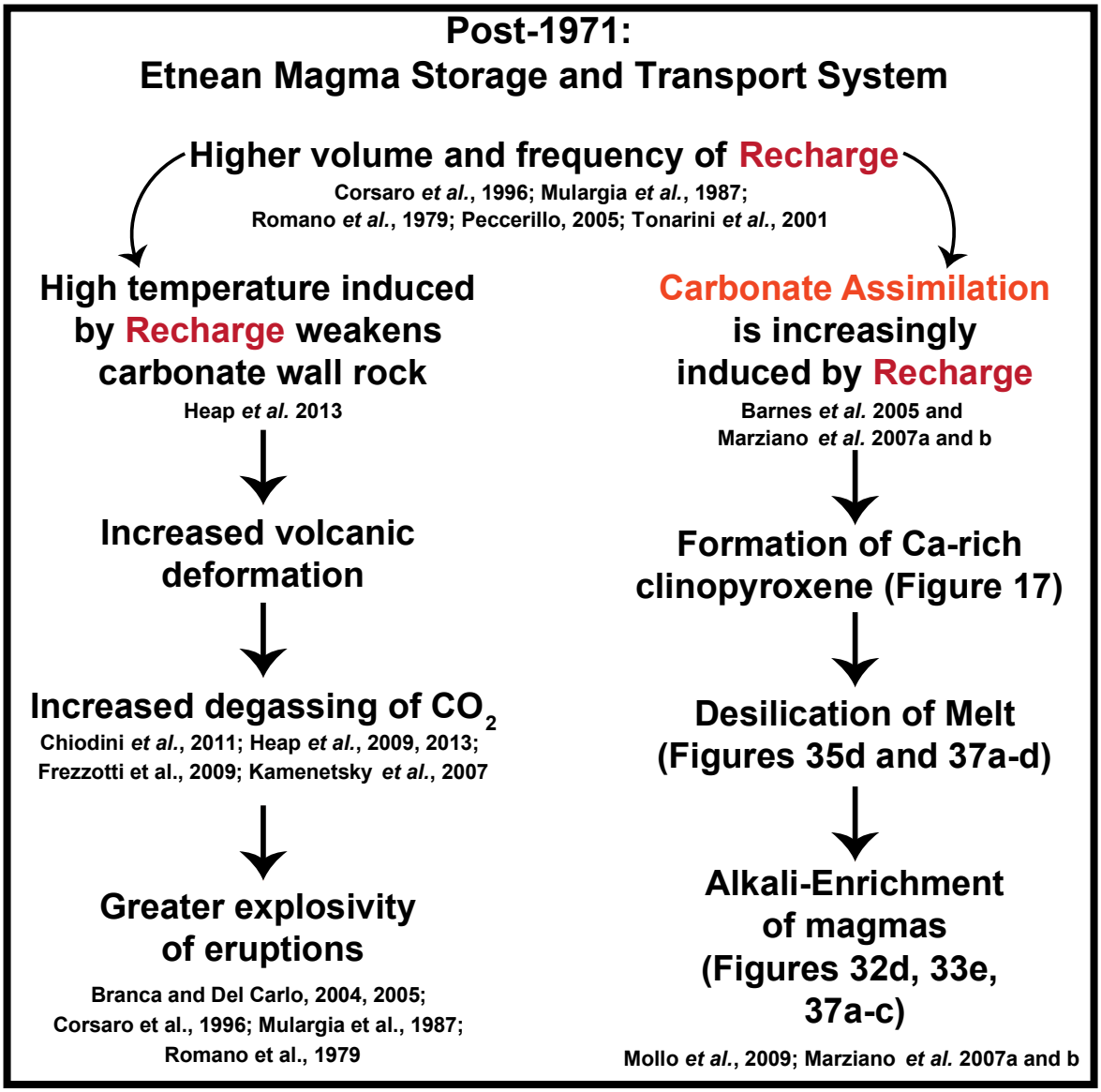

Figure 41. Flow chart of post-1971 Etnean magma storage and transport system dynamics and interpretations. Relevant scientific literature and relevant figures are cited for reference.

CHAPTER VI

SUMMARY AND FUTURE WORK

This research demonstrates the application of clinopyroxene *in situ* textural, geochemical and isotopic data in conjunction with geobarometry, in order to document the structural and evolutionary changes of the Mt. Etna's magma storage and transport system, as well as the dominant magmatic pathways at work. Recording this information from 1329 to 2004 AD provides a window into the spatial and temporal evolution of Mt. Etna's highly dynamic magmatic regime, in addition to the intriguing alkali-enrichment signature, which becomes dramatically pronounced in post-1971 samples.

This work has documented a clinopyroxene crystallization zone that extends from below the Moho (~27 km) to the upper crust (<6 km), with a primary crystallization zone at approximately 8.7-16.5 km (2.9-5.5 ± 2 kbar). Intricate crystallization histories, as demonstrated by heterogeneous textural, geochemical and isotopic features, provide evidence for complex magmatic pathways, including fractional crystallization, and open-system processes of crustal assimilation and recharge/dynamic mixing, which take place within a subvolcanic plexus of interconnected dikes and sills.

Furthermore, carbonate assimilation/contamination by the basaltic magmas is implicated by unique geochemical and pressure relationships, (e.g. CaO vs. pressure), isotopic disequilibrium between crystals and their whole rock, and evidence for clinopyroxene inherited from magmatic skarns. Influxes of magmatic recharge/mixing are also implied by these geochemical observations, and may play a part in initiating and promoting such assimilation processes by supplying hot, volatile-rich magmas from

depth. The destructive eruption of 1669 may have also initiated new pathways within Mt. Etna's subvolcanic plumbing system, allowing the mechanism of carbonate assimilation ± recharge to become increasingly influential over time within the system.

Several experimental and analytical studies (Di Rocco *et al.*, 2012; Heap *et al.*, 2013; Iacono Marziano *et al.*, 2007a; Marziano and Gaillard, 2006; Mollo *et al.*, 2010) also relate carbonate assimilation processes to an expression of alkali-enrichment in eruptive products. Within the Etnean magmatic system, this premise is substantiated by the abundance of clinopyroxene rims that are systematically enriched in $^{87}Sr/^{86}Sr$, implying that this enrichment is late-stage. This $^{87}Sr/^{86}Sr$ enrichment also occurs at levels that are consistent with the carbonate substratum of the Hyblean Plateau. Furthermore, the documentation of increased CO_2 emissions and seismicity in association with the alkali-enrichment signature, according to Heap *et al.* (2013), may also represent a connection between the source and timing of alkali-enrichment, and magma-carbonate interactions (Figure 39b).

In order quantitatively document the roles of fractional crystallization, recharge/mixing and crustal assimilation of a carbonate assimilant/contaminant, future work will include computational modeling, which can evaluate the influences these processes have within the magmatic system (Bohrson *et al.*, 2014). *In situ* clinopyroxene trace element analysis via laser ablation-inductively coupled plasma mass spectrometry (LA-ICPMS) may also document compositional trends and further characterize the contributions of crustal components and mantle recharge. In addition, melt inclusion studies can provide further insight into Mt. Etna's geochemical evolution, as well as

identify the presence CaO-rich, silica-undersaturated and Al_2O_3-rich melts, as documented by Marziano *et al.* (2007) and Mollo *et al.* (2010), which would hold strong implications for carbonate assimilation and alkali-enrichment processes. Finally, additional microsampling and $^{87}Sr/^{86}Sr$ analysis of clinopyroxene cores and rims will further build upon this reconstruction of the Mt. Etna magma and transport system from 1329 to 2004 AD.

REFERENCES

Acocella, V., Neri, M. and Norini, G. (2013). An overview of experimental models to understand a complex volcanic instability: Application to Mount Etna, Italy. *Journal of Volcanology and Geothermal Research* **251**, 98–111.

Ague, J. J. (2003). Fluid Infiltration and Transport of Major, Minor, and Trace Elements During Regional Metamorphism of Carbonate Rocks, Wepawaug Schist, Connecticut, USA. *American Journal of Science* **303**, 753–816.

Aiuppa, A., Federico, C., Paonita, A. and Pecoraino, G. (2002). S , Cl and F degassing as an indicator of volcanic dynamics : The 2001 eruption of Mount Etna. **29**, 1–4.

Allard, P. *et al.* (1991). Eruptive and diffuse emissions of CO2 from Mount Etna. *Nature* **351**, 387–391.

Allard, P., Jeanbaptiste, P., Dalessandro, W., Parello, F., Parisi, B. and Flehoc, C. (1997). Mantle-derived helium and carbon in groundwaters and gases of Mount Etna, Italy. *Earth and Planetary Science Letters* **148**, 501–516.

Aloisi, M., Bonaccorso, A., Cannavò, F., Gambino, S., Mattia, M., Puglisi, G. and Boschi, E. (2009). A new dyke intrusion style for the Mount Etna May 2008 eruption modelled through continuous tilt and GPS data. *Terra Nova* **21**, 316–321.

Anderson, H. and Jackson, J. (1987). The deep seismicity of the Tyrrhenian Sea. *Geophysical Journal International* **91**, 613–637.

Andronico, D. *et al.* (2004). A multi-disciplinary study of the 2002-03 Etna eruption: insights into a complex plumbing system. *Bulletin of Volcanology* **67**, 314–330.

Argnani, A. and Bonazzi, C. (2005). Malta Escarpment fault zone offshore eastern Sicily: Pliocene-Quaternary tectonic evolution based on new multichannel seismic data. *Tectonics* **24**, 1-12.

Armienti, P. (2004). Genesis and evolution of Mt. Etna alkaline lavas: petrological and Sr-Nd-B isotope constraints. *Periodico di Mineralogia* **73**, 29–52.

Armienti, P., Innocenti, F., Petrini, R., Pompilio, M. and Villari, L. (1989). Petrology and Sr-Nd isotope geochemistry of recent lavas from Mt. Etna: bearing on the volcano feeding system. *Journal of Volcanology and Geothermal Research* **39**, 315–327.

Armienti, P., Macedonio, G. and Pareschi, M. T. (1988). A numerical model for simulation of tephra transport and deposition: Applications to May 18, 1980, Mount St. Helens eruption. *Journal of Geophysical Research* **93**, 6463.

Armienti, P., Perinelli, C. and Putirka, K. D. (2012). A New Model to Estimate Deep-level Magma Ascent Rates, with Applications to Mt. Etna (Sicily, Italy). *Journal of Petrology* **54**, 795–813.

Armienti, P., Tonarini, S., D'Orazio, M. and Innocenti, F. (2004). Genesis and evolution of Mt. Etna alkaline lavas; petrological and Sr-Nd-B isotope constraints. *Periodico di Mineralogia* **73**, 29–52.

Armienti, P., Tonarini, S., Innocenti, F. and D'Orazio, M. (2007). Mount Etna pyroxene as a tracer of petrogenetic processes and dynamics of the feeding system. *Geological Society of America: Special Papers* **418**, 265-276.

Barberi, F., Civetta, L., Gasparini, P., Innocenti, F., Scandone, R. and Villari, L. (1974). Evolution of a section of the Africa-Europe plate boundary: Paleomagnetic and

volcanological evidence from Sicily. *Earth and Planetary Science Letters* **22**, 123–132.

Barnes, C. G., Prestvik, T., Sundvoll, B. and Surratt, D. (2005). Pervasive assimilation of carbonate and silicate rocks in the Hortavær igneous complex, north-central Norway. *Lithos* **80**, 179–199.

Behncke, B. and Neri, M. (2003). Cycles and trends in the recent eruptive behaviour of Mount Etna (Italy). *Canadian Journal of Earth Sciences* **40**, 1405–1411.

Ben-Avraham, Z. and Grasso, M. (1990). Collisional zone segmentation in Sicily and surrounding areas in the central Mediterranean. *Annales Tectonicae* **4**, 131–139.

Bianchini, G., Clocchiatti, R., Coltorti, M., Joron, J. L. and Vaccaro, C. (1998). Petrogenesis of mafic lavas from the northernmost sector of the Iblean district (Sicily). *European Journal of Mineralogy* **10**, 301–316.

Blatt, H., Tracy, R. and Owens, B. (2006). *Petrology: Igneous, Sedimentary, and Metamorphic*. New York: W. H. Freeman.

Bohrson, W. A. and Spera, F. J. (2001). Energy-constrained open-system magmatic processes II: Application of energy-constrained assimilation-fractional crystallization (EC-AFC) model to magmatic systems. *Journal of Petrology* **42**, 1019–1041.

Bohrson, W. A., Spera, F. J., Ghiorso, M. S., Brown, G. A., Creamer, J. B. and Mayfield, A. (2014). Thermodynamic Model for Energy-Constrained Open-System Evolution of Crustal Magma Bodies Undergoing Simultaneous Recharge, Assimilation and

Crystallization: the Magma Chamber Simulator. *Journal of Petrology* **55**, 1685–1717.

Bonaccorso, A., Currenti, G., Del Negro, C. and Boschi, E. (2010). Dike deflection modelling for inferring magma pressure and withdrawal, with application to Etna 2001 case. *Earth and Planetary Science Letters* **293**, 121–129.

Bonaccorso, A., Ferrucci, F., Patanè, D. and Villari, L. (1996). Fast deformation processes and eruptive activity at Mount Etna (Italy). *Journal of Geophysical Research* **101**, 17467.

Bonforte, A., Gambino, S. and Neri, M. (2009). Intrusion of eccentric dikes: The case of the 2001 eruption and its role in the dynamics of Mt. Etna volcano. *Tectonophysics* **471**, 78–86.

Bonforte, A. and Sturiale, G. (2008). Strain on Africa-Europa boundary in the northern Hyblean plateau margin (SE-Sicily) from GPS and geological data. *EGU General Assembly, Geophysical Research Abstracts* **10**, 1-3.

Boroughs, S., (2013), personal communication.

Bousquet, J. and Lanzafame, G. (2004). The tectonics and geodynamics of Mt. Etna: synthesis and interpretation of geological and geophysical data. *Geophysical Monograph Series* **143**, 29–49.

Branca, S. (2003). Intrusive mechanism of the 2002 NE-Rift eruption at Mt. Etna (Italy) inferred through continuous microgravity data and volcanological evidences. *Geophysical Research Letters* **30**, 2077.

Branca, S., Coltelli, M., De Beni, E. and Wijbrans, J. (2008). Geological evolution of Mount Etna volcano (Italy) from earliest products until the first central volcanism (between 500 and 100 ka ago) inferred from geochronological and stratigraphic data. *International Journal of Earth Sciences* **97**, 135–152.

Branca, S., De Beni, E. and Proietti, C. (2013). The large and destructive 1669 AD eruption at Etna volcano: reconstruction of the lava flow field evolution and effusion rate trend. *Bulletin of Volcanology* **75**, 694.

Branca, S. and Del Carlo, P. (2004). Eruptions of Mt . Etna during the past 3,200 years: a revised compilation integrating the historical and stratigraphic records, in Mt. Etna: volcano laboratory. *American Geophysical Union Geophysical Monograph* **143**, 1-29.

Branca, S. and Del Carlo, P. (2005). Types of eruptions of Etna volcano AD 1670–2003: implications for short-term eruptive behaviour. *Bulletin of Volcanology* **67**, 732–742.

Caracausi, A., Favara, R., Giammanco, S., Italiano, F., Paonita, A. and Pecoraino, G. (2003). Mount Etna: Geochemical signals of magma ascent and unusually extensive plumbing system. *Geophysical Research Letters* **30**, 1057.

Carbone, D., D'Amico, S., Musumeci, C. and Greco, F. (2009). Comparison between the 1994–2006 seismic and gravity data from Mt. Etna: New insight into the long-term behavior of a complex volcano. *Earth and Planetary Science Letters* **279**, 282–292.

Carbone, S., Lentini, F. and Grasso, M. (1982). Considerazioni sul- F evoluzione geodinamica della Sicilia sud-orientale dal Cretaceo al Quaternario. Mem. Soc. Geol It, 24, 367-386, 1982. *Mem. Soc. Geol. It* **24**, 367–386.

Carminati, E., Doglioni, C. and Cuffaro, M. (2006). What moves slabs? *Bollettino di Geofisica Teorica e Applicata* **47**, 227–247.

Cartwright, J. and Møller Hansen, D. (2006). Magma transport through the crust via interconnected sill complexes. *Geology* **34**, 929.

Carveni, P., Grasso, M. and Romano, R. (1991). Vulcanismo del margine settentrionale ibleo. *Mem. Soc. Geol. It.* **47**, 417–429.

Catalano, S., Torrisi, S. and Ferlito, C. (2004). The relationship between Late Quaternary deformation and volcanism of Mt. Etna (eastern Sicily): new evidence from the sedimentary substratum in the Catania region. *Journal of Volcanology and Geothermal Research* **132**, 311–334.

Chadwick, J. P., Troll, V. R., Ginibre, C., Morgan, D., Gertisser, R., Waight, T. E. and Davidson, J. P. (2007). Carbonate Assimilation at Merapi Volcano, Java, Indonesia: Insights from Crystal Isotope Stratigraphy. *Journal of Petrology* **48**, 1793–1812.

Chatterjee, N. (2012). *Electron Microprobe Analysis, 12.141*. *MIT OpenCourseWare: Massachusetts Institute of Technology*, 2–43.

Chiarabba, C., Amato, A., Boschi, E. and Barberi, F. (2000). Recent seismicity and tomographic modeling of the Mount Etna plumbing system. *Journal of Geophysical Research* **105**, 10923.

Chiodini, G., Caliro, S., Cardellini, C., Frondini, F., Inguaggiato, S. and Matteucci, F. (2011). Geochemical evidence for and characterization of CO2 rich gas sources in the epicentral area of the Abruzzo 2009 earthquakes. *Earth and Planetary Science Letters* **304**, 389–398.

Clocchiatti, R., Joron, J.-L. and Treuil, M. (1988). The role of selective alkali contamination in the evolution of recent historic lavas of Mt. Etna. *Journal of Volcanology and Geothermal Research* **34**, 241–249.

Clocchiatti, R., Schiano, P., Ottolini, L. and Bottazzi, P. (1998). Earlier alkaline and transitional magmatic pulsation of Mt Etna volcano. *Earth and Planetary Science Letters* **163**, 399–407.

Coltelli, M., Del Carlo, P. and Vezzoli, L. (2000). Stratigraphic constraints for explosive activity in the past 100 ka at Etna Volcano, Italy. *International Journal of Earth Sciences* **89**, 665–677.

Condomines, M., Tanguy, J. ., Kieffer, G. and Allègre, C. . (1982). Magmatic evolution of a volcano studied by 230Th-238U disequilibrium and trace elements systematics: The Etna case. *Geochimica et Cosmochimica Acta* **46**, 1397–1416.

Condomines, M., Tanguy, J.-C. and Valerie, M. (1995). Magma dynamics at Mt Etna : Constraints from U-Th-Ra-Pb radioactive disequilibria and Sr isotopes in historical lavas. *Earth and Planetary Science Letters* **132**, 25–41.

Continisio, R., Ferrucci, F., Gaudiosi, G., Lo Bascio, D. and Ventura, G. (1997). Malta escarpment and Mt. Etna; early stages of an asymmetric rifting process? Evidences from geophysical and geological data. *Acta Vulcanologica* **9**, 45–53.

Correale, A., Paonita, A., Martelli, M., Rizzo, A., Rotolo, S. G., Corsaro, R. A. and Di Renzo, V. (2014). A two-component mantle source feeding Mt. Etna magmatism: Insights from the geochemistry of primitive magmas. *Lithos* **184-187**, 243–258.

Corsaro, R. A., Cristofolini, R., Patanè, L. and Patanand#x000E8;, L. (1996). The 1669 eruption at Mount Etna: chronology, petrology and geochemistry, with inferences on the magma sources and ascent mechanisms. *Bulletin of Volcanology* **58**, 348–358.

Corsaro, R. a., Métrich, N., Allard, P., Andronico, D., Miraglia, L. and Fourmentraux, C. (2009). The 1974 flank eruption of Mount Etna: An archetype for deep dike-fed eruptions at basaltic volcanoes and a milestone in Etna's recent history. *Journal of Geophysical Research* **114**, 1-20.

Corsaro, R. A., Miraglia, L. and Pompilio, M. (2006). Petrologic evidence of a complex plumbing system feeding the July–August 2001 eruption of Mt. Etna, Sicily, Italy. *Bulletin of Volcanology* **69**, 401–421.

Corsaro, R. A. and Pompilio, M. (2000). Dynamics of magmas at Mount Etna, in Mt. Etna: volcano laboratory. *Geophysical Monograph Series* **143**, 91-110.

Corsaro, R. A. and Pompilio, M. (2004). Magma dynamics in the shallow plumbing system of Mt. Etna as recorded by compositional variations in volcanics of recent summit activity (1995–1999). *Journal of Volcanology and Geothermal Research* **137**, 55–71.

Coulson, I. M., Westphal, M., Anderson, R. G. and Kyser, T. K. (2007). Concomitant skarn and syenitic magma evolution at the margins of the Zippa Mountain pluton. *Mineralogy and Petrology* **90**, 199–221.

Cristofolini, R., Ghisetti, F., Scarpa, R. and Vezzani, L. (1985). Character of the stress field in the Calabrian Arc and Southern Apennines (Italy) as deduced by geological, seismological and volcanological information. *Tectonophysics* **117**, 39–58.

Cristofolini, R., Lentini, F., Patanè, G. and Rasa, R. (1979). Intergrazione di dati geologici, geofisici e petrologici per la stesura di un profilo crostale in corrispondenza dell'Etna. *Bollettino della Societa Geologica Italiana*. The Electrochemical Society **98**, 239–247.

Cristofolini, R., Menzies, M. A., Beccaluva, L. and Tindle, A. (1987). Petrological notes on the 1983 lavas at Mount Etna, Sicily, with reference to their REE and Sr-Nd isotope composition. *Bulletin of Volcanology* **49**, 599–607.

Davidson, J. P., Morgan, D. J., Charlier, B. L. a., Harlou, R. and Hora, J. M. (2007). Microsampling and Isotopic Analysis of Igneous Rocks: Implications for the Study of Magmatic Systems. *Annual Review of Earth and Planetary Sciences* **35**, 273–311.

Dawson, P. (2004). Application of near real-time radial semblance to locate the shallow magmatic conduit at Kilauea Volcano, Hawaii. *Geophysical Research Letters* **31**, L21606.

De Gori, P., Chiarabba, C. and Patanè, D. (2005). Qp structure of Mount Etna: Constraints for the physics of the plumbing system. *Journal of Geophysical Research B: Solid Earth* **110**, 1–16.

Deer, W. A., Howie, R. A. and Zussman, J. (1982). *Rock-forming minerals: Orthosilicates, Volume 1, Part 1*. Longman.

Del Negro, C., Currenti, G. and Scandura, D. (2009). Temperature-dependent viscoelastic modeling of ground deformation: Application to Etna volcano during the 1993–1997 inflation period. *Physics of the Earth and Planetary Interiors* **172**, 299–309.

Di Rocco, T., Freda, C., Gaeta, M., Mollo, S. and Dallai, L. (2012). Magma Chambers Emplaced in Carbonate Substrate: Petrogenesis of Skarn and Cumulate Rocks and Implications for CO2 Degassing in Volcanic Areas. *Journal of Petrology* **53**, 2307–2332.

Di Stefano, A. and Branca, S. (2002). Long-term uplift rate of the Etna volcano basement (southern Italy) based on biochronological data from Pleistocene sediments. *Terra Nova* **14**, 61–68.

Doglioni C., F., I. and G., M. (1998). On the geodynamic origin of Mt. Etna. *Atti 17° Convegno Gruppo Nazionale Geofisica Terra Solida, Roma*

Doglioni, C., Innocenti, F. and Mariotti, G. (2001). Why Mt Etna? *Terra Nova* **13**, 25–31.

Dvorkin, J., Nur, A., Mavko, G. and Ben-Avraham, Z. (1993). Narrow subducting slabs and the origin of backarc basins. *Tectonophysics* **227**, 63–79.

Edmonds, M., Aiuppa, A., Humphreys, M., Moretti, R., Giudice, G., Martin, R. S., Herd, R. A. and Christopher, T. (2010). Excess volatiles supplied by mingling of mafic magma at an andesite arc volcano. *Geochemistry, Geophysics, Geosystems* **11**, 1–16.

Federico, M., Peccerillo, A., Barbieri, M. and Wu, T. W. (1994). Mineralogical and geochemical study of granular xenoliths from the Alban Hills volcano, Central Italy: bearing on evolutionary processes in potassic magma chambers. *Contributions to Mineralogy and Petrology* **115**, 384–401.

Ferlito, C., Coltorti, M., Cristofolini, R. and Giacomoni, P. P. (2009). The contemporaneous emission of low-K and high-K trachybasalts and the role of the NE Rift during the 2002 eruptive event, Mt. Etna, Italy. *Bulletin of Volcanology* **71**, 575–587.

Ferlito, C. and Lanzafame, G. (2010). The role of supercritical fluids in the potassium enrichment of magmas at Mount Etna volcano (Italy). *Lithos* **119**, 642–650.

Ferlito, C., Viccaro, M. and Cristofolini, R. (2008). Volatile-induced magma differentiation in the plumbing system of Mt. Etna volcano (Italy): Evidence from glass in tephra of the 2001 eruption. *Bulletin of Volcanology* **70**, 455–473.

Finetti, I., Lentini, F., Carbone, S., Catalano, S. and Del Ben, A. (1996). Il sistema Appennino Meridionale-Arco Calabro-Sicilia nel Mediterraneo Centrale; studio geologico-geofisico. *Bollettino della Societa Geologica Italiana* **115**, 529–559.

Freda, C., Gaeta, M., Misiti, V., Mollo, S., Dolfi, D. and Scarlato, P. (2008). Magma–carbonate interaction: An experimental study on ultrapotassic rocks from Alban Hills (Central Italy). *Lithos* **101**, 397–415.

Frezzotti, M. L., Peccerillo, A. and Panza, G. (2009). Carbonate metasomatism and CO2 lithosphere–asthenosphere degassing beneath the Western Mediterranean: An integrated model arising from petrological and geophysical data. *Chemical Geology* **262**, 108–120.

Gaeta, M., Di Rocco, T. and Freda, C. (2009). Carbonate Assimilation in Open Magmatic Systems: the Role of Melt-bearing Skarns and Cumulate-forming Processes. *Journal of Petrology* **50**, 361–385.

Ghiorso, M. S. (2002). The pMELTS: A revision of MELTS for improved calculation of phase relations and major element partitioning related to partial melting of the mantle to 3 GPa. *Geochemistry Geophysics Geosystems* **3**, 1-35.

Goodge, J. (University of M.-D. (2012). *Geochemical Instrumentation and Analysis: Electron probe micro-analyzer (EPMA)*. *Science Education Research Center, Carleton College*.

Grasso, M. and Ben-Avraham, Z. (1992). Magnetic study of the northern margin of the Hyblean Plateau, south-eastern Sicily. *Terra Abstracts* **3**, 270.

Grasso, M. and Lentini, F. (1982). Sedimentary and tectonic evolution of the eastern Hyblean Plateau (southeastern Sicily) during late Cretaceous to Quaternary time. *Palaeogeography, Palaeoclimatology, Palaeoecology* **39**, 261–280.

Grasso, M., Lentini, F., Nairn, A. E. M. and Vigliotti, L. (1983). A geological and paleomagnetic study of the Hyblean volcanic rocks, Sicily. *Tectonophysics* **98**, 271–295.

Guest, J. E. and Duncan, A. M. (1981). Internal plumbing of Mount Etna. *Nature* **290**, 584–586.

Gvirtzman, Z. and Nur, A. (1999). The formation of Mount Etna as the consequence of slab rollback. *Nature* **401**, 782–785.

Gvirtzman, Z. and Nur, A. (2001). Residual topography, lithospheric structure and sunken slabs in the central Mediterranean. *Earth and Planetary Science Letters* **187**, 117–130.

Heap, M. J. J., Mollo, S., Vinciguerra, S., Lavallée, Y., Hess, K.-U. U., Dingwell, D. B. B., Baud, P. and Iezzi, G. (2013). Thermal weakening of the carbonate basement under Mt. Etna volcano (Italy): Implications for volcano instability. *Journal of Volcanology and Geothermal Research* **250**, 42–60.

Heap, M. J., Mollo, S., Lavallée, Y., Vinciguerra, S., von Aulock, F. W., Dingwell, D. B. and Baud, P. (2009). How Does Temperature Influence the Physical and Chemical Properties of the Deep Carbonate Basement and Shallow Lava Flows at Mt. Etna Volcano? *American Geophysical Union, Fall Meeting 2009, abstract #V23D-2144*.

Hess, P. C. and Head, J. W. (1990). Derivation of primary magmas and melting of crustal materials on Venus: Some preliminary petrogenetic considerations. *Earth, Moon and Planets* **50-51**, 57–80.

Hirn, A., Nicolich, R., Gallart, J., Laigle, M., Cernobori, L. and ETNASEIS Scientific Group (1997). Roots of Etna volcano in faults of great earthquakes. *Earth and Planetary Science Letters* **148**, 171–191.

Hughes, J. W., Guest, J. E. and Duncan, A. M. (1990). *Changing styles of effusive eruption on Mount Etna since AD 1600*. New York: John Wiley and Sons. 385-406.

Iacano Marziano, G. I. and Gaillard, F. (2006). Limestone Assimilation: a Dominant non-Magmatic Source of Volcanic CO2. *American Geophysical Union, Fall Meeting 2007, abstract #V34A-04*.

Iacono Marziano, G., Gaillard, F. and Pichavant, M. (2007a). Limestone assimilation by basaltic magmas: an experimental re-assessment and application to Italian volcanoes. *Contributions to Mineralogy and Petrology* **155**, 719–738.

Iacono Marziano, G., Gaillard, F. and Pichavant, M. (2007b). Limestone assimilation and the origin of CO2 emissions at the Alban Hills (Central Italy): Constraints from experimental petrology. *Journal of Volcanology and Geothermal Research* **166**, 91–105.

Jerram, D. and Martin, V. (2008). Understanding crystal populations and their significance through the magma plumbing system. *Geological Society, London, Special Publications* **304**, 133-148.

Kahl, M., Chakraborty, S., Costa, F., Pompilio, M., Liuzzo, M. and Viccaro, M. (2013). Compositionally zoned crystals and real-time degassing data reveal changes in magma transfer dynamics during the 2006 summit eruptive episodes of Mt. Etna. *Bulletin of Volcanology* **75**, 692.

Kamenetsky, V. S., Pompilio, M., Métrich, N., Sobolev, A. V., Kuzmin, D. V. and Thomas, R. (2007). Arrival of extremely volatile-rich high-Mg magmas changes explosivity of Mount Etna. *Geology* **35**, 255.

Laigle, M. and Hirn, A. (1999). Explosion-seismic tomography of a magmatic body beneath Etna: Volatile discharge and tectonic control of volcanism. *Geophysical Research Letters* **26**, 2665–2668.

Lanzafame, G. and Bousquet, J. C. (1997). The Maltese escarpment and its extension from Mt. Etna to the Aeolian Islands (Sicily): Importance and evolution of a lithosphere discontinuity. *Acta Vulcanologica* **9**, 113–120.

Lentini, F. (1982). The geology of the Mt. Etna basement. *Mem. Soc, Geol. It* **23**, 7–25.

Lentini, F., Carbone, S. and Catalano, S. (1994). Main structural domains of the Central Mediterranean region and their Neogene tectonic evolution. *Bollettino di Geofisica Teorica ed Applicata* **36**, 103–125.

Longaretti, G., Rocchi, S. and Ferrari, L. (1991). Il magmatismo dell'avampaese Ibleo (Sicilia orientale) tra il Trias e il Quaternario; dati di sottosuolo della piana di Catania dal Pleistocene al Miocene medio. *Memorie della Societa Geologica Italiana* **47**, 537–555.

Marsh, B. (2004). A magmatic mush column rosetta stone: the McMurdo dry valleys of Antarctica. *Eos, Transactions American Geophysical Union* **85**, 497.

Marsh, B. D. (2006). Dynamics of Magmatic Systems. *Elements* **2**, 287–292.

Martelli, M., Caracausi, A., Paonita, A. and Rizzo, A. (2008). Geochemical variations of air-free crater fumaroles at Mt Etna: new inferences for forecasting shallow volcanic activity. *Geophysical Research Letters* **35**, L21302.

Martin, V. M., Davidson, J., Morgan, D. and Jerram, D. A. (2010). Using the Sr isotope compositions of feldspars and glass to distinguish magma system components and dynamics. *Geology* **38**, 539–542.

Meinert, L. D. (1992). Skarns and skarn deposits. *Geoscience Canada* **19**, 145–162.

Mercatanti, L. (2013). Etna and the perception of volcanic risk. *Geographical Review* **103**, 486–497.

Métrich, N., Allard, P., Spilliaert, N., Andronico, D. and Burton, M. (2004). 2001 flank eruption of the alkali- and volatile-rich primitive basalt responsible for Mount Etna's evolution in the last three decades. *Earth and Planetary Science Letters* **228**, 1–17.

Michaud, V. (1991). L'enrichissement sélectif en K, Rb et Cs des laves récentes de l'Etna: rôle des fluides du système phréatique dans l'interaction magma - encaissant sédimentaire et implications sur les dynamismes éruptifs = Selective enrichment in K, Rb and Cs of Etna pre. University Paris, XI. Thesis.

Michaud, V. (1995). Crustal xenoliths in recent hawaiites from Mount Etna, Italy: evidence for alkali exchanges during magma-wall rock interaction. *Chemical Geology* **122**, 21–42.

Michaud, V., Clocchiatti, R. and Joron, J. L. (1988). Approche des phénomènes d'interaction magma/encaissant par l'étude des enclaves énallogènes. L'éruption paroxysmale du 24 septembre 1986 de l'Etna (Sicile). *Comptes rendus de l'Académie des sciences. Série 2, Mécanique, Physique, Chimie, Sciences de l'univers, Sciences de la Terre* **307**, 1527–1533.

Michaud, V. M. and Clocchiatti, R. (1994). Pyroxene features in crustal xenoliths from Etna; primary nature and elemental exchanges with magma. *Acta Vulcanologica* **5**, 105–115.

Mollo, S., Gaeta, M., Freda, C., Di Rocco, T., Misiti, V. and Scarlato, P. (2010). Carbonate assimilation in magmas: A reappraisal based on experimental petrology. *Lithos* **114**, 503–514.

Monaco, C. and Tortorici, L. (2000). Active faulting in the Calabrian arc and eastern Sicily. *Journal of Geodynamics* **29**, 407–424.

Morgan, W. J. (1971). Convection Plumes in the Lower Mantle. *Nature* **230**, 42–43.

Morgan, W. J. (1972). Studies in Earth and Space Sciences. *Geological Society of America Memoirs* **132**, 7-22.

Moses, M. N. (2010). Use of MELTS Modeling and Detailed Textural and Chemical Crystal Population Studies to Document Magma Chamber Processes at Mount Etna, Sicily. Thesis.

Mueller, P. (2012). *Geochemical Instrumentation and Analysis: Thermal Ionization Mass Spectrometry (TIMS)*. *Science Education Research Center, Carleton College*, 1.

Mulargia, F., Gasperini, P. and Tinti, S. (1987). Identifying different regimes in eruptive activity: An application to Etna volcano. *Journal of Volcanology and Geothermal Research* **34**, 89–106.

Murru, M. (2005). Mapping of the b value anomalies beneath Mt. Etna, Italy, during July–August 2001 lateral eruption. *Geophysical Research Letters* **32**, L05309.

Murru, M., Console, R., Falcone, G., Montuori, C. and Sgroi, T. (2007). Spatial mapping of the b value at Mount Etna, Italy, using earthquake data recorded from 1999 to 2005. *Journal of Geophysical Research*. **112**, B12303.

Murru, M., Montuori, C., Wyss, M. and Privitera, E. (1999). The locations of magma chambers at Mt. Etna, Italy, mapped by b-values. *Geophysical Research Letters* **26**, 2553–2556.

Musumeci, C., Scarfì, L., Palano, M. and Patanè, D. (2014). Foreland segmentation along an active convergent margin: New constraints in southeastern Sicily (Italy) from seismic and geodetic observations. *Tectonophysics* **630**, 137–149.

Neri, M., Acocella, V. and Behncke, B. (2004). The role of the Pernicana Fault System in the spreading of Mt. Etna (Italy) during the 2002-2003 eruption. *Bulletin of Volcanology* **66**, 417–430.

Nur, A., Dvorkin, J., Makvo, G. and Ben-Avraham, Z. (1991). Speculations on the origin and fate of backarc basins. *Annali di Geofisica* **36**, 155–163.

Paonita, A., Caracausi, A., Iacono-Marziano, G., Martelli, M. and Rizzo, A. (2012). Geochemical evidence for mixing between fluids exsolved at different depths in the magmatic system of Mt Etna (Italy). *Geochimica et Cosmochimica Acta* **84**, 380–394.

Paris, G. De, Monaco, C., Tapponnier, P., Tortorici, L. and Gillot, P. Y. (1997). Late Quaternary slip rates on the Acireale-Piedimonte normal faults and tectonic origin of Mt. Etna (Sicily). *Earth and Planetary Science Letters* **147**, 125–139.

Patanè, D., Aliotta, M., Cannata, A., Cassisi, C., Coltelli, M., Di Grazia, G., Montalto, P. and Zuccarello, L. (2011). Interplay between tectonics and Mount Etna's volcanism: insights into the geometry of the plumbing system. *New Frontiers in Tectonic Research - At the Midst of Plate Convergence*. InTech. 73-77.

Patanè, G., La Delfa, S. and Tanguy, J.-C. (2006). Volcanism and mantle–crust evolution: The Etna case. *Earth and Planetary Science Letters* **241**, 831–843.

Paulatto, M., Minshull, T. A. and Henstock, T. J. (2010). Constraints on an intrusive system beneath the Soufriére Hills Volcano, Montserrat, from finite difference modeling of a controlled source seismic experiment. *Geophysical Research Letters* **37**.

Peccerillo, A. (2005). *Plio-Quaternary Volcanism in Italy: Petrology, Geochemistry, Geodynamics*. Springer Science and Business Media. 1-4.

Pedley, M. H. and Grasso, M. (1992). Miocene syntectonic sedimentation along the western margins of the Hyblean-Malta platform: A guide to plate margin processes in the central Mediterranean. *Journal of Geodynamics* **15**, 19–37.

Pitcher, B. (2011). Crustal Assimilation and Magma Recharge in the Recent Mt. Etna Magma Plumbing System: Evidence from In Situ Plagioclase Textural and Compositional Data. Thesis.

Preston, R. J. (2001). Composite minor intrusions as windows into subvolcanic magma reservoir processes: mineralogical and geochemical evidence for complex magmatic plumbing systems in the British Tertiary Igneous Province. *Journal of the Geological Society* **158**, 47–58.

Putirka, K. D. (2008). Thermometers and Barometers for Volcanic Systems. *Reviews in Mineralogy and Geochemistry* **69**, 61–120.

Putirka, K. D., Mikaelian, H., Ryerson, F. and Shaw, H. (2003). New clinopyroxene-liquid thermobarometers for mafic, evolved, and volatile-bearing lava compositions, with applications to lavas from Tibet and the Snake River Plain, Idaho. *American Mineralogist*. Mineralogical Society of America **88**, 1542–1554.

Ramos, F. C., Wolff, J. A. and Tollstrup, D. L. (2005). Sr isotope disequilibrium in Columbia River flood basalts: Evidence for rapid shallow-level open-system processes. *Geology* **33**, 457.

Richet, P., Leclerc, F. and Benoist, L. (1993). Melting of forsterite and spinel, with implications for the glass transition of Mg 2 SiO 4 liquid. *Geophysical Research Letters* **20**, 1675–1678.

Rittmann, A. and Sato, M. (1973). Structure and evolution of Mount Etna [and discussion]. *Philosophical Transactions of the Royal Society A: Mathematical, Physical and Engineering Sciences* **274**, 5–16.

Rollin, P. J., Cassidy, J., Locke, C. A. and Rymer, H. (2000). Evolution of the magmatic plumbing system at Mt Etna: New evidence from gravity and magnetic data. *Terra Nova* **12**, 193–198.

Romano, R. (1982). Succession of volcanic activity in the etnean area. *Memorie della Società Geologica Italiana* **23**, 27–48.

Romano, R. (1983). Mount Etna volcano: a review of recent earth sciences studies. *Memorie Della Società Geologica Italiana* **23**, 75-97.

Romano, R., Sturiale, C. and Lentini, F. (1979). Carta geologica del Monte Etna, Geological map of Mt. Etna. Firenze. *Memorie della Società Geologica Italiana* **23**.

Schellart, W. P. (2010a). Slab-rollback induced upper mantle upwelling near lateral slab edges: A new mechanism for generating intra-plate magmatism in the central Mediterranean. *American Geophysical Union, Fall Meeting 2010, abstract #T13G-08*.

Schellart, W. P. (2010b). Mount Etna-Iblean volcanism caused by rollback-induced upper mantle upwelling around the Ionian slab edge: An alternative to the plume model. *Geology* **38**, 691–694.

Schiano, P., Clocchiatti, R., Ottolini, L. and Busà, T. (2001). Transition of Mount Etna lavas from a mantle-plume to an island-arc magmatic source. *Nature* **412**, 900–904.

Schmincke, H. U., Behncke, B., Grasso, M. and Raffi, S. (1997). Evolution of the northwestern Iblean Mountains, Sicily: uplift, Plicocene/Pleistocene sea-level changes, paleoenvironment, and volcanism. *Geologische Rundschau* **86**, 637–669.

Scribano, V., Viccaro, M., Cristofolini, R. and Ottolini, L. (2008). Metasomatic events recorded in ultramafic xenoliths from the Hyblean area (Southeastern Sicily, Italy). *Mineralogy and Petrology* **95**, 235–250.

Şengör, A. M. C. (2009). Tectonic evolution of the Mediterranean : a dame with four husbands. *Trabajos de Geología, Universidad de Oviedo* **50**, 45–50.

Sharp, A. D. L., Davis, P. M. and Gray, F. (1980). A low velocity zone beneath Mount Etna and magma storage. *Nature* **287**, 587–591.

Tanguy, J. C. (1978). Tholeiitic basalt magmatism of Mount Etna and its relations with the alkaline series. *Contributions to Mineralogy and Petrology* **67**, 51–67.

Tanguy, J. C. (1981). Les Éruptions Historiques de L'Etna: Chronologie et Localisation. *Bulletin Volcanologique* **44**, 585–640.

Tanguy, J. C., Condomines, M. and Kieffer, G. (1997). Evolution of the Mount Etna magma: Constraints on the present feeding system and eruptive mechanism. *Journal of Volcanology and Geothermal Research* **75**, 221–250.

Tanguy, J. C., Kieffer, G. and Patanè, G. (1996). Dynamics, lava volume and effusion rate during the 1991–1993 eruption of Mount Etna. *Journal of Volcanology and Geothermal Research* **71**, 259–265.

Tepley, F. J. I., Davidson, J. P., Tilling, R. I. and Arth, J. G. (2000). Magma mixing, recharge and eruption histories recorded in plagioclase phenocrysts from El Chichon Volcano, Mexico. *Journal of Petrology* **41**, 1397–1411.

Thomson, K. (2004). Sill complex geometry and internal architecture: a 3D seismic perspective. *Geological Society, London, Special Publications* **234**, 229–232.

Tonarini, S., Armienti, P., D'Orazio, M. and Innocenti, F. (2001). Subduction-like fluids in the genesis of Mt. Etna magmas: evidence from boron isotopes and fluid mobile elements. *Earth and Planetary Science Letters* **192**, 471–483.

Trigila, R., Spera, F. J. and Aurisicchio, C. (1990). The 1983 Mount Etna eruption: thermochemical and dynamical inferences. *Contributions to Mineralogy and Petrology* **104**, 594–608.

Viccaro, M. and Cristofolini, R. (2008). Nature of mantle heterogeneity and its role in the short-term geochemical and volcanological evolution of Mt. Etna (Italy). *Lithos* **105**, 272–288.

Viccaro, M., Ferlito, C., Cortesogno, L., Cristofolini, R. and Gaggero, L. (2006). Magma mixing during the 2001 event at Mount Etna (Italy): Effects on the eruptive dynamics. *Journal of Volcanology and Geothermal Research* **149**, 139–159.

Viccaro, M., Ferlito, C. and Cristofolini, R. (2008). Complex evolution processes in the upper feeding system of Mt. Etna (Italy) as revealed by the geochemistry of recent lavas. *Periodico di Mineralogia* **77**, 21–42.

Viccaro, M., Giacomoni, P. P., Ferlito, C. and Cristofolini, R. (2010). Dynamics of magma supply at Mt. Etna volcano (Southern Italy) as revealed by textural and compositional features of plagioclase phenocrysts. *Lithos* **116**, 77–91.

Villaseñor, A., Benz, H. M., Filippi, L., De Luca, G., Scarpa, R., Patanè, G. and Vinciguerra, S. (1998). Three-dimensional P -wave velocity structure of Mt. Etna, Italy. *Geophysical Research Letters* **25**, 1975–1978.

Villemant, B., Michaud, V. and Métrich, N. (1993). Wall rock-magma interactions in Etna, Italy, studied by U-Th disequilibrium and rare earth element systematics. *Geochimica et Cosmochimica Acta* **57**, 1169–1180.

Wadge, G. (1977). The storage and release of magma on Mount Etna. *Journal of Volcanology and Geothermal Research* **2**, 361–384.

Wadge, G. and Guest, J. E. (1981). Steady-state magma discharge at Etna 1971–81. *Nature* **294**, 548–550.

Wadge, G., Walker, G. P. L. and Guest, J. E. (1975). The output of the Etna volcano. *Nature* **255**, 385–387.

Washington State University. (2015). *Peter Hooper GeoAnalytical Lab Electron Microprobe*. 1.

Wenzel, T., Baumgartner, L. P., Brügmann, G. E., Konnikov, E. G. and Kislov, E. V. (2002). Partial melting and assimilation of dolomitic xenoliths by mafic magma: the Ioko-Dovyren intrusion (North Baikal region, Russia). *Journal of Petrology* **43**, 2049–2074.

Yellin-Dror, A., Grasso, M., Ben-Avraham, Z. and Tibor, G. (1997). The subsidence history of the northern Hyblean plateau margin, southeastern Sicily. *Tectonophysics* **282**, 277–289.

Zellmer, G. F. and Annen, C. (2008). An introduction to magma dynamics. *Geological Society, London, Special Publications* **304**, 1–13.